

UNIVERSITY OF TWENTE.



SURGICAL ROBOTICS
LABORATORY

Self-assembled Magnetic Carpets for Cargo-Transport of Millimetric Planar Objects

Dionne Ariëns
M.Sc. Thesis
May 2023

Board of Examinators:

Prof.dr. Sarthak Misra
MSc. Juan Julian Jesus Huaroto Sevilla
dr.ir. Ronald Aarts

Document number:

BE-923

Surgical Robotics Laboratory
Department of Biomechanical Engineering
Faculty of Engineering Technology
University of Twente
P.O. Box 217
7500 AE Enschede
The Netherlands



Acknowledgements

I am extremely grateful to Prof.dr. Sarthak Misra and MSc. Juan J.J. Huaroto Sevilla for their guidance and feedback during my thesis assignment. In addition, this endeavor would not have been possible without my external supervisor dr.ir Ronald Aarts. Lastly, I could not have undertaken this journey without access to the Surgical Robotics Lab located at the University of Twente.

I am also thankful to Rob Struik for his help with the hardware of the BatMag system. In addition I am grateful to other members and master students from the SRL lab that have helped me by answering questions and inspired me during the thesis assignment.

Lastly, I would like to mention my family, boyfriend, and friends for motivation and support during this process.

Summary

Nature provides many examples of collective behavior ranging from social insects to bird flocks. Collective behavior has motivated scientists to develop multi-robotic systems to overcome the limitations of single robotic units. At the microscale, the collective behavior of artificial cilia has demonstrated applications in cargo transportation, drug delivery, and self-cleaning technologies. Magnetic-actuated artificial cilia (i.e., magnetic carpets) consist of numerous pillar-like structures fabricated using two main fabrication techniques: molding and self-assembly. Molding techniques are suitable for fabricating homogeneous pillar-like structures yet involve complex and expensive mold creation methods. Magnetic self-assembly is the spontaneous organization of magnetic components and can be used to create pillar-like structures from microparticles. However, there are still challenges in understanding pillar-like structure formation and reconfiguring the magnetic carpet under magnetic fields and gradients.

In this master's thesis, we propose a fabrication-free approach to create a magnetic carpet by self-assembly using reduced iron microparticles. The fabrication-free approach permits generating and reconfiguring the magnetic carpet within the workspace. Throughout the report, we analyze the pillar-like structure formation from magnetic self-assembly. Furthermore, we examine the behaviour of the magnetic carpet by different actuation mechanisms using an electromagnetic system composed of nine coils. Lastly, we experimentally validate which actuation mechanism is most efficient for cargo transport of planar objects of different shapes, sizes and weights.

In the results of this thesis we find that the height and density of the created magnetic carpet increases when using more microparticles or currents on the electromagnetic coils to create the carpet. The actuation mechanisms examined for the carpet behaviour include rotational magnetic fields, oscillating magnetic fields and sweeping magnetic fields. The pillars behave differently at each point in the workspace which influences the cargo transport. We experimentally observe that the sweeping magnetic field is the most efficient actuation mechanism to displace planar objects into two dimensions.

Contents

Acknowledgements	iii
Summary	v
List of acronyms	ix
1 Introduction	1
2 Background	3
2.1 Magnetic carpets	3
2.1.1 Molding techniques	3
2.1.2 Self-assembly techniques	5
2.1.3 Other fabrication techniques	5
2.1.4 Actuation of the magnetic carpets	5
2.2 Cargo transport using magnetic carpets	6
2.2.1 Gelatin Robot	6
2.2.2 Asymmetric-structured Intelligent Magnetic Pillar Actuator	7
2.2.3 Soft Magnetic Carpet	7
2.2.4 Magnetically Flexible Arrays	8
2.2.5 Magnetic Artificial Cilia Carpets	9
2.2.6 Reconfigurable carpets	9
2.3 Contribution to state-of-the-art	10
3 Materials and Methods	11
3.1 BatMag System	11
3.1.1 Hardware	11
3.1.2 Software	12
3.2 Used materials	12
4 Results and discussion	15
4.1 Carpet characterisation	15
4.1.1 Static characterisation	15
4.1.2 Dynamic performance	16
4.2 Transport of non-magnetic planar objects	28

4.2.1	Lifting planar objects with different weights	29
4.2.2	Displacement of the planar objects	29
4.3	Proof-of-concepts using the carpet	33
4.3.1	Rotation of a planar object	33
4.3.2	Moving the planar objects into two dimensions	34
4.3.3	Reconfiguration and relocation of the carpet	38
5	Conclusions and future work	41
	References	43
	Appendices	
A	Background	47
A.1	Magnetism	47
A.1.1	Maxwell's Equations	49
A.1.2	Electromagnetic field and magnetic materials	51
A.2	Swarm robotics	52
A.2.1	High-Level and Low-Level tasks in swarm robotics	53
B	BatMag system	55
B.1	Hardware designs	56
B.2	Software design	57
C	Description of performed experiments	61
C.1	Characterisation of carpet formation	61
C.2	Characterisation of the behavior of the carpet under different magnetic fields	62
C.2.1	Experiment 1: carpet under magnetic fields	62
C.2.2	Experiment 2: Adding iron microparticles under rotational magnetic field	63
C.3	Carpet strength	64
C.4	Cargo transport using different magnetic fields	64
C.4.1	Experiment 1: cargo transport using rotating, oscillating and sweeping magnetic fields	64
C.4.2	Experiment 2: Cargo transport using rotational magnetic field	66
C.5	Final experiments	67
C.5.1	Experiment 1: Cargo transport with circular and triangle planar objects under rotating magnetic field	67
C.5.2	Experiment 2: Cargo transport into two dimensions	68
C.5.3	Experiment 3: Replacing carpet and planar object	69
D	Simulations of magnetic fields	73
E	Full data of planar object displacement	79

List of acronyms

IEEE	Institute of Electrical and Electronics Engineers
SRL	Surgical Robotics Lab
3D	Three-dimensional
2D	Two-dimensional
DI	Deionization
AI-MPA	Asymmetric-structured Intelligent Magnetic Pillar Actuator
SMC	Soft Magnetic Carpet
PS	Polystyrene
PDMS	Polydimethylsiloxane
MACC	Magnetic Artificial Cilia Carpet
PCB	Printed Circuit Board
LED	Light-emitting diode
CAN	Controller Area Network
GUI	Graphical User Interface
ROS	Robotic Operating System
PET	Polyethylene terephthalate
ROI	Region of interest
NdFeB	Neodymium-iron-boron

Introduction

In nature we see collective behaviour in animal groups like fish schools, swarms of insects, bird flocks, herds of mammals or groups of ants [15]. Such groups can execute tasks that individuals are unable to perform by themselves. For example, a group of ants that try to cross a gap by forming a bridge. These collective behaviours have inspired to optimize multi-robot systems [10]. These multi-robot systems exists on macro-, micro- or nanoscales and are used for multiple applications in different fields such as chemical, industrial and medical as identified in Cheraghi *et al.* [10]. On microscale, collectives of magnetic microparticles are able to perform for example targeted drug delivery [6], minimally invasive surgery [26] and cargo transport [37].

Cargo transport can be used for transporting solid objects like glass beads [37] or fluids like a glycerol droplet [13]. A common strategy used for cargo transport is creating a magnetic carpet consisting of pillars inspired by cilia which shows an effective way of transporting objects or fluids in nature [23]. Magnetic carpets are used in for example, drug delivery systems [23], self-cleaning technologies [18] [12] and mixing liquids [13] [31]. These carpets are commonly created using a mixture of magnetic microparticles and polymer and controlled using magnetic fields. In the literature, there are two main fabrication techniques to fabricate the carpet structures: the molding

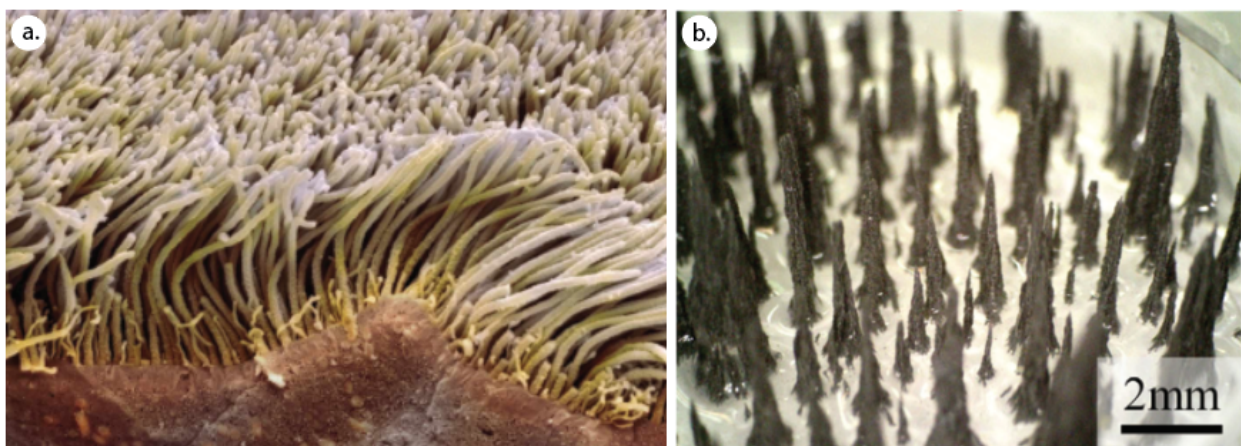


Figure 1.1: (a) Cilia in microbiological systems (image obtained from ThoughtCo [1]). (b) Magnetic carpets inspired on biological cilia (image obtained from Miao *et al.* [22]).

and the self-assembly technique (according to Ni *et al.* [23]). For the molding technique, a mixture of polymer and magnetic microparticles is added to a mold and the substance is cured. It is also possible to use a magnetic during the molding technique where the magnet is used to create the pillars inside the mold. For the self-assembly technique a magnetic field is used to generate the pillars spontaneously. This is therefore a simpler fabrication process compared to the molding technique. It is also possible to configure the pillars from magnetic self-assembly. The pillars are then generated using a magnetic field and returns to separate microparticles when the magnetic field is deactivated [37]. Since most carpets consists of a mixture of magnetic microparticles and polymer, they cannot reconfigure from pillar-like structures to for example vortex, chain or ribbon structures [36] to perform different tasks. In addition, the carpet cannot easily relocate inside the workspace.

The aim of this thesis is to generate a fabrication-free carpet from reduced iron microparticles using a nine electromagnetic coil setup called BatMag. Magnetic fields can be generated without changing the distance between the magnet and the workspace which is an advantage compared to the other researches in the state-of-the-art.

First we characterize the carpet in static and dynamic case to observe the behaviour of the microparticles when the magnetic carpet is generated and actuated. In the static case, the height and density of the pillars of the carpet are analyzed. For the dynamic characterisation, different actuation mechanisms are used to observe the behaviour of the carpet during actuation. The actuation mechanisms include rotational magnetic fields, oscillating magnetic fields and sweeping magnetic fields. Multiple planar objects are created from polyethylene terephthalate (PET) with different weights and sizes. These are placed on the carpet inside the workspace. The effectiveness of cargo transport for each actuation mechanism is observed. The most efficient actuation mechanisms are used to perform cargo transport in two dimensions using planar objects with different shapes, sizes and weights.

The report is structured in (2) the background which goes further into magnetic carpets. This is followed by the (3) materials and methods chapter which discusses the BatMag system, the performed experiments and the materials used during materials. The (4) results of the experiments are divided into three subsections: the characterisation of the carpet, the transport of non-magnetic planar object using different actuation mechanisms. Lastly, the (5) conclusions and future work of this research are discussed.

Background

In nature, there are multiple examples of animal species that work together as a group to accomplish day-to-day tasks like ants building a bridge over a gap, bird flocks gathered over the roost at nightfall, herds of mammals and a school of fish swimming under water [15]. This is called collective behaviour. In literature, this concept is used at the microscales and has applied in swarms of microrobots [38] (see Appendix A for more information swarm robotics). Magnetic microparticles can form pillar-like structures, inspired by cilia, to perform tasks in a wide range of applications [23]. Multiple magnetically-responsive pillar-structures form magnetic carpets.

In the next sections we go further into detail and discuss the essential concepts: (2.1) magnetic carpets and (2.2) cargo transport. In addition, we discuss a few related applications and we close with (2.3) the contribution to the state-of-the-art.

2.1 Magnetic carpets

Cilia is present in nature on various surfaces of micro-organisms, exists of micro-pillars (between 1 and 30 μm) and behaves like sensors and actuators [33]. There are various types of cilia that differ in shapes and sizes and are able to perform multiple tasks like transportation and sensing (e.g., transport oocytes through the fallopian tube or get information about blood flow) [33]. Micropillared-structures (also called artificial cilia) have multiple applications like for example, targeted drug delivery [23], microfluidic propulsion [13], object manipulations [37] and self-cleaning technologies [18] [12].

Multiple of these pillar-like structures form magnetic carpets. There are two main fabrication techniques for the fabrication of the magnetic carpets: molding techniques and self-assembly techniques [28].

2.1.1 Molding techniques

According to Ni *et al.* [23], the molding technique is a fabrication technique where the magnetic carpet is fabricated using a mold pattern where a mixture of magnetic microparticles and poly-

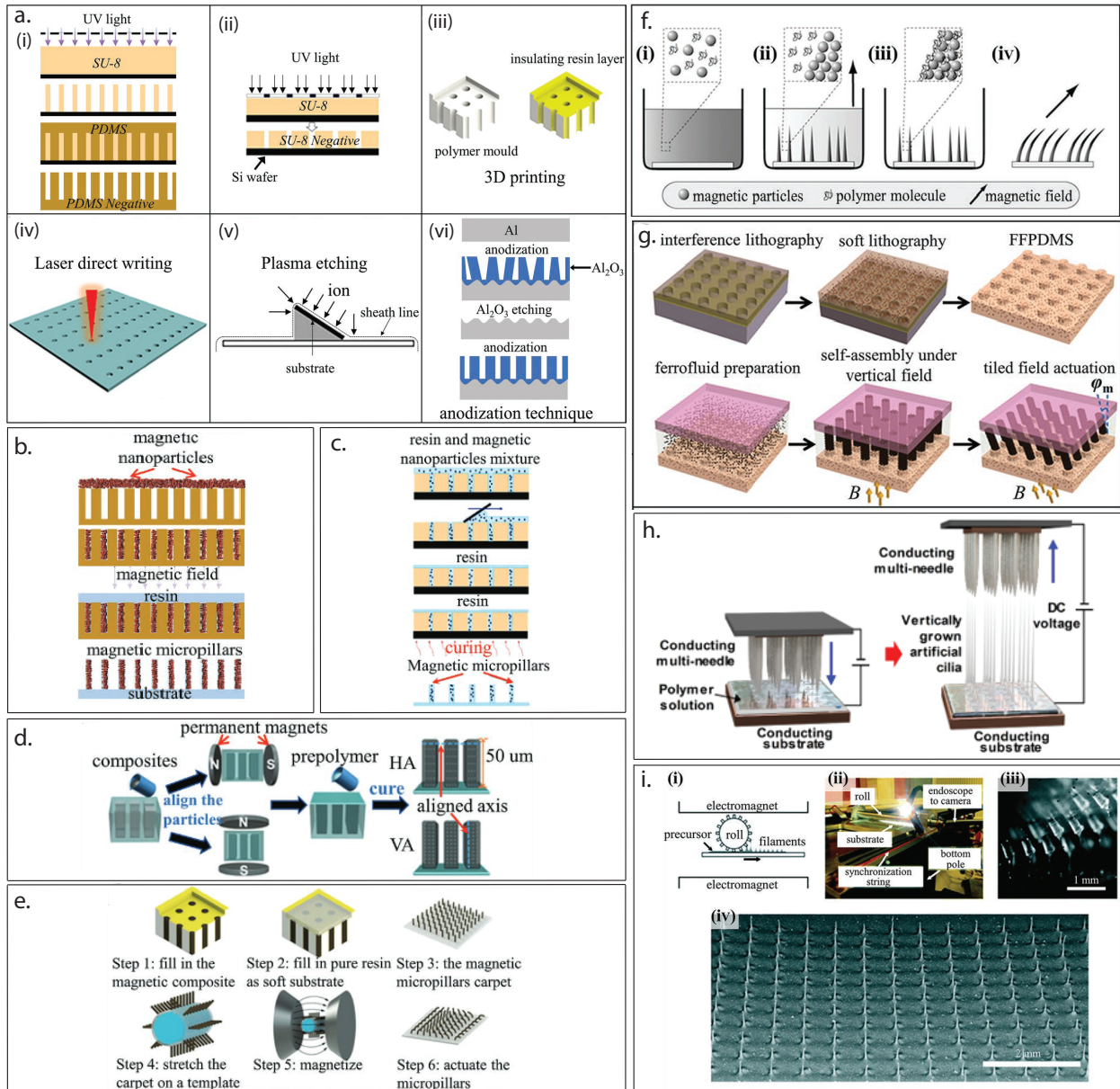


Figure 2.1: Illustration of the different fabrication techniques. a) Illustrates the fabrication methods of molds (used in the molding fabrication techniques) that include (i) indirect and (ii) direct photolithography, (iii) 3D printing, (iv) laser writing, (v) plasma etching and (vi) anodization. b-e) Illustrates examples of the molding technique including the (b) dry-nanoparticle embedding technique, (c) solvent casting technique, (d) micropillar fabrication with aligned nanoparticle chains and (e) carpet fabrication with magnetization of the magnetic particles. f-g) Illustrates examples of the self-assembly technique including (f) the facile bottom-up approach and (g) an approach using soft lithography. h-i) Illustrates examples of other existing techniques to fabricate a magnetic carpet: (h) the roll-pulling approach and (i) the field-effect spinning approach. (Images are adopted by Ni et al. [23] and Sahadevan et al. [28].)

mer material is poured into the pattern (illustrated in Figure 2.1b). This approach can also be performed using a magnet underneath the mold to form the pillars inside the mold (illustrated in Figure 2.1c). Figure 2.1d-e show two other examples of the molding technique in which the magnetic particles are aligned in chain-like patterns before curing the substance (Figure 2.1d) and a molding technique in which the magnetic particles are magnetized [23]. The mold patterns used

in the molding technique are typically fabricated using photolithography (direct and indirect), 3D printing, laser writing, plasma etching and anodization (illustrated in Figure 2.1a) [23].

2.1.2 Self-assembly techniques

The self-assembly technique is a fabrication technique which does not use molds to fabricate the magnetic carpet but the pillar-like structures are automatically assembled from the magnetic particles using a magnetic field [23]. Then the assembled pillars are surrounded with a polymer coating. An example of the self-assembly technique is the facile bottom-up approach in which a mixture of magnetic microparticles, elastomeric poly and toluene is ultrasonicated to fabricate the magnetic carpet (illustrated in Figure 2.1f) [28]. Another example of the self-assembly approach is where a magnetic carpet is fabricated by using soft lithography (illustrated in Figure 2.1c) [23].

2.1.3 Other fabrication techniques

According to Ni *et al.* [23] and Sahadevan *et al.* [28], there exist other fabrication techniques besides the molding and self-assembly techniques. Examples of such techniques are the roll-pulling approach (where a magnetic carpet is fabricated by soft lithography using an aluminum roll as illustrated in Figure 2.1d) [23] and the field-effect spinning approach where the length and diameter of the pillars of the carpet can be controlled during the fabrication process (illustrated in Figure 2.1e) [28].

2.1.4 Actuation of the magnetic carpets

The carpet can be steered inside magnetic fields since the fabricated carpets include magnetic microparticles. In literature there are two types of magnetic actuation, magnetic force-based and magnetic torque-based actuation [38], to actuate the pillars of the magnetic carpet. The magnetic torque-based actuation is expressed in Equation 2.1 where $\tau \in \mathbb{R}^3$ is the magnetic torque and $m \in \mathbb{R}^3$ is the magnetic moment.

$$\tau = \mathbf{m} \times \mathbf{B} \quad (2.1)$$

The most commonly used coils to generate an uniform magnetic field are Helmholtz coils [38]. Torques can be generated in a system that consists of Helmholtz coils in a 3D configuration. The torque-based actuation is used to generate the swinging motion of the pillars [37]. The magnetic particles align with the magnetic flux lines of the magnetic field after the magnetic particles are magnetized. The pillars are then able to make a swinging motion when the magnetic field changes over time. Two forces will appear when the pillars move: the dynamic fluidic forces and the inter-microrobot magnetic forces which are the main forces that influence the resulting behaviour of the pillars [38]. The forces between the microparticles and the fluidic forces exist when the pillar

moves and flow patterns are created. The magnetic force-based actuation (also called magnetic gradient-based actuation) is expressed in Equation 2.2.

$$\mathbf{F} = \nabla(\mathbf{m} \cdot \mathbf{B}) \quad (2.2)$$

For this actuation type the microparticles will be propelled to the magnetic potential energy minima by a converging magnetic field via the force described in Equation 2.2 [38]. In other words, using the force-based actuation, the pillar-like structures are created and maintained [37].

2.2 Cargo transport using magnetic carpets

Cargo transport is defined as the movement of a material from a certain location to another location. In the microrobotics concept, the material can be solids like body cells or glass beads but it can also be fluids like a glycerol droplet [13] [37]. In the next subsections a few researches are discussed that developed and used magnetic carpets for cargo transport.

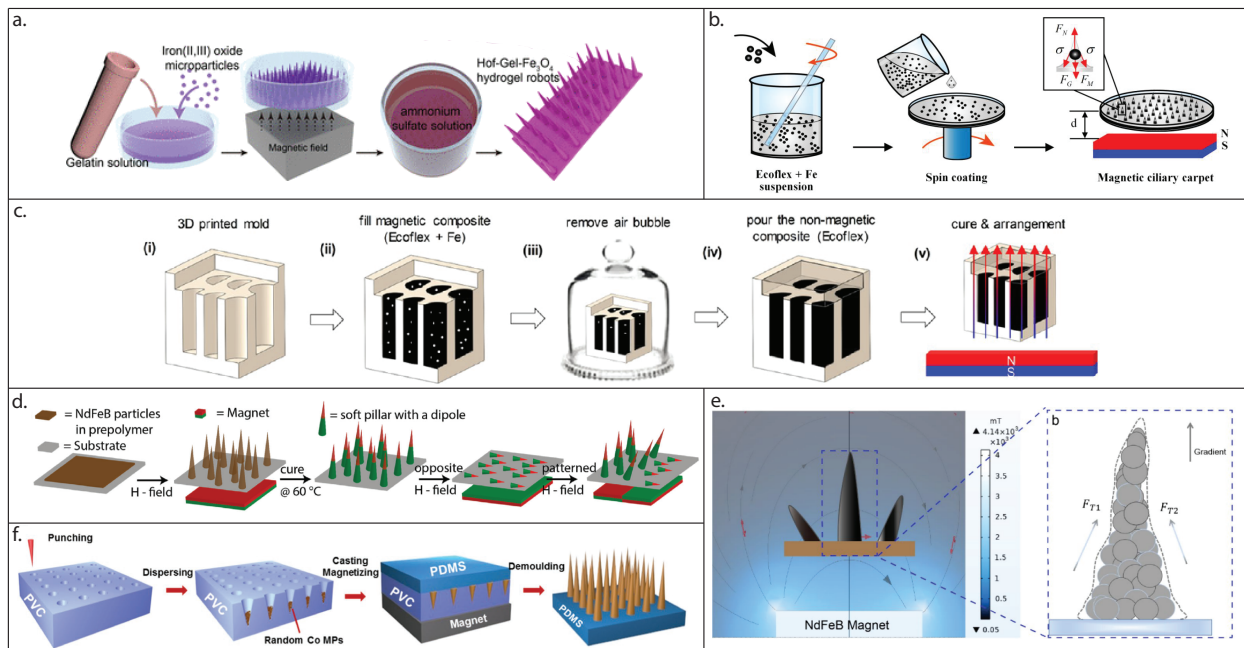


Figure 2.2: Fabrication processes of (a) the gelatin robot by Yang *et al.* [19], (b) the MACC by Miao *et al.* [22], (c) the AI-MPA by Miao *et al.* [21], (d) the soft magnetic carpet by Demirörs *et al.* [13], (e) the reconfigurable carpet by Xu *et al.* [37] and (f) Magnetically flexible arrays by [7].

2.2.1 Gelatin Robot

The research of Yang *et al.* [19] developed a magnetic carpet consisting of magnetic hydrogel which is a mixture of iron(II, III) oxide microparticles and a gelatin solution (referred to as the gelatin robot). In the self-assembly fabrication process a permanent magnet is used to create the pillars which are referred to as legs (Figure 2.2a). The amount of legs created onto the carpet

depends on the distance between the substance and the permanent magnet. The created soft robot has the function of grasping and cargo transport. An external magnetic field (generated by a permanent magnet) is used to magnetize the legs and bend the legs towards each other. Then the gelatin robot is able to grip objects (in the paper a 3D-printed cylinder is used). The cylinder will be released when the permanent magnet is removed from the robot. Yang *et al.* [19] developed a method to perform cargo transport using the gelatin robot (Figure 2.3a). The robot will wrap itself around the cargo by rotating the permanent magnet around the z-axis. The robot rolls through the workspace when the permanent magnet is rotated around the x-axis and z-axis. Lastly, the robot will open again to release the cargo by rotating the permanent magnet around the y-axis. An advantage that was demonstrated in the research of Yang *et al.* [19] is that the gelatin robot can be easily degrade using deionized (DI) water.

2.2.2 Asymmetric-structured Intelligent Magnetic Pillar Actuator

The research of Miao *et al.* [21] creates a magnetic carpet, inspired on biological cilia and pine needles, called asymmetric-structured intelligent magnetic pillar actuator (AI-MPA). The AI-MPA is fabricated using the molding process using a mixture of iron microparticles and Ecoflex 00-30 (Figure 2.2c). The AI-MPA has two main functionalities for small-scale liquid operations: the cargo transport of liquids and the ability to crawl around the workspace. The pillars on the AI-MPA will bend due to an external magnetic field which is created by a moving permanent magnet. The AI-MPA is able to perform two types of transport: active and passive cargo transport (Figure 2.3b). For active transport, the tips of the AI-MPA can transport liquids into a certain direction by changing the translation direction of the permanent magnet and results in a metachronal wave of the pillars. The liquid moves into the opposite direction of this wave. For passive cargo transport, a droplet of liquid is transported at the bottom of the AI-MPA in static state which means that the external magnetic field has a static gradient. The direction of the transport depends on this static gradient of the external magnetic field. The second functionality is the robotic crawling of the AI-MPA. The AI-MPA is now turned upside down and the pillars work as legs. Using translation of the permanent magnet around the axes the AI-MPA is able to move into different directions and is able to rotate around itself. According to Miao *et al.* [21] the functionality to rotate around its own axis is a big advantage on other crawling robots.

2.2.3 Soft Magnetic Carpet

The work of Demirörs *et al.* [13] shows a development method of a soft magnetic carpet (SMC). The carpet is fabricated using the self-assembly process and consists of a mixture of neodymium iron boron particles with Ecoflex 00-20 (Figure 2.2d). The size and density of the fabricated pillars depend on the strength of the permanent magnet used in the fabrication process. SMC is developed for cargo transport and mixing purposes. The SMC can transport droplets of liquid and solid objects inside wet and dry workspaces. In addition, the SMC can separate or sort objects by using the cargo transport methods. The SMC is suitable for transporting fragile objects for e.g. industrial production applications and biomedical applications. Demirörs *et al.* [13] used cylindrical magnets

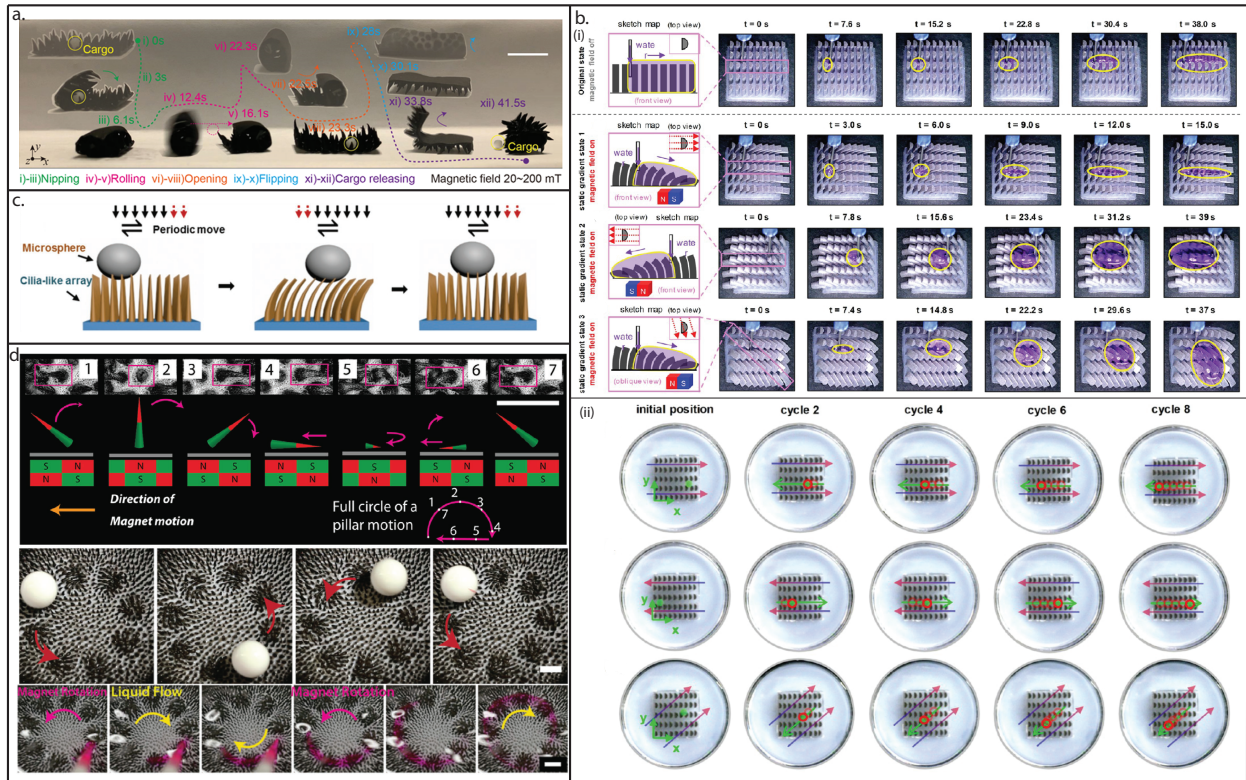


Figure 2.3: (a) Cargo transport of solids by the gelatin robot [19]. The gelatin robot is also able to relocate itself by using the pillars as legs. (b) Active and passive transport of liquids using the AI-MPA [21]. (c) Illustration of cargo transport of solids on the magnetically flexible arrays [7]. (d) An illustration of the movement of the pillars of the soft magnetic carpet [13]. Cargo transport of solids and liquids on top of the soft magnetic carpets.

in a circular shape (called a magnetic track) underneath the workspace to generate the external magnetic field by alternating the orientation of these magnets. The magnetic track is attached to a motor to rotate the track and generate the alternating magnetic field. The rotation of the magnetic track results in a ring-shaped pattern of depressions on the surface of the SMC also called wells. A solid spherical object on the SMC stays in such well and therefore makes a rotating motion on the surface of the SMC (illustrated in Figure 2.3d). This method of cargo transportation is efficient for any object with any shape as long the contact between the solid object and the SMC stays inside a well. In addition, the SMC can transport objects onto tilted surfaces. Lasly, Demirörs *et al.* [13] shows that the SMC can transport liquids (illustrated in Figure 2.3d).

2.2.4 Magnetically Flexible Arrays

Ben *et al.* [7] proposes a carpet of magnetically flexible arrays for cargo transport of polystyrene (PS) microspheres. The carpet is fabricated using the mechanical punching and template dissolving technology (illustrated in Figure 2.2f) consisting of PDMS prepolymer and cobalt magnetic particles. To actuate the flexible arrays, a permanent magnet is attached to a manipulator that moves above the carpet sample. Without an external field, the pillars will stay vertically and the pillars will bend when an external field is activated. A cyclically magnetic field is generated when

the manipulator is moved. The bending of the pillars makes the PS microsphere move over the flexible arrays (illustrated in Figure 2.3c). The experiments are performed using two different carpets: magnetically flexible conical arrays (consists of pillars with a pointy top) and magnetically flexible columnar arrays (consists of pillars with a flat top). Ben *et al.* [7] found that the speed of transporting a PS microsphere is higher for the flexible conical arrays than for the flexible columnar arrays. In addition they found that the distance between the pillars influences the distance of transporting the PS microspheres.

2.2.5 Magnetic Artificial Cilia Carpets

A magnetic artificial cilia carpet (MACC) is developed by the work of Miao *et al.* [22]. The carpet is fabricated by a template-free self-assembly process using a mixture of Ecoflex 00-30 and iron microparticles (illustrated in Figure 2.2b). Under an external magnetic field generated by a permanent magnet the pillars bend and create a movement inspired on the biological cilia. Miao *et al.* [22] performed two different control methods that result in a nodal-cilia-like motion and a metachronal motion of the MACC to transport solids and liquids. For the cargo transport of a planar object (plane-shaped and ellipsoid-shaped objects) they used a metachronal motion which is created by translating the permanent magnet. One cycle of the movement of the pillars causes a forward and backward stage as shown in Figure 2.4a. In addition, the MACC can mix solids and liquids where the metachronal motion of the MACC is best for directional mixing of solids and the nodal-cilia-like motion of the MACC is best for directional diffusion of liquids.

2.2.6 Reconfigurable carpets

Lastly we discuss the work of Xu *et al.* [37]. In this research the magnetic carpet is fabricated using self-assembly with iron(III) oxide microparticles with a size less than 5 μm (illustrated in Figure 2.2e). The carpet is actuated inside an electromagnetic setup of 4 electromagnets and a permanent magnet below the workspace. The permanent magnet is needed to maintain the pillars of the carpet and the electromagnetic coils are used to generate an oscillating or rotating magnetic field. The four electromagnetic coils are actuated separately by a sinusoidal signal of currents to create an oscillating or rotating external magnetic field. The work of Xu *et al.* [37] shows that using a rotating magnetic field onto the magnetic carpet, glass beads can be pushed through the workspace (shown in Figure 2.4b). In addition, the carpet can reconfigure its pattern for different applications. Using an oscillating magnetic field, the pillars can be reconfigured in a ribbon-like configuration. Using the rotating magnetic field they are able to relocate the magnetic carpet. Also they are able to perform liquid diffusion and move a micro bead through a microchannel using the reconfigurable carpet (Figure 2.4b). Lastly they develop a method to remove an attachment in a microchannel containing pure water (Figure 2.4b).

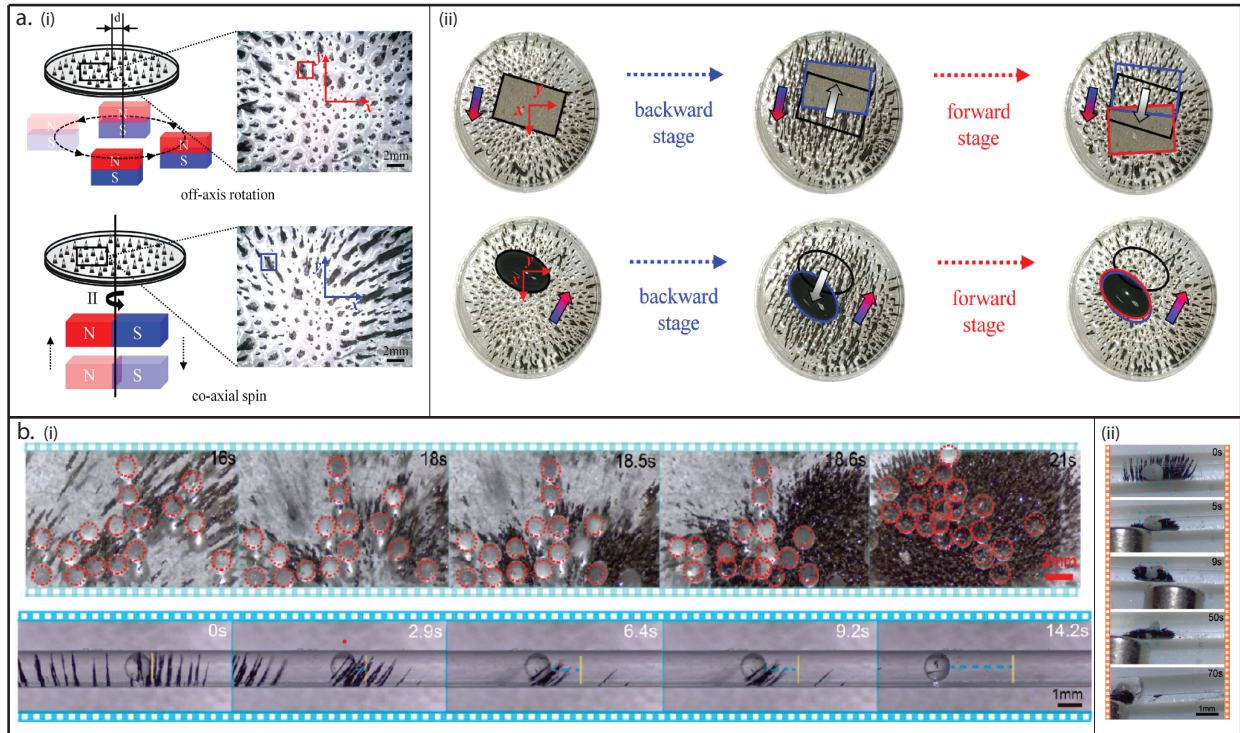


Figure 2.4: (a) Illustration of the two control methods: off-axis rotation and co-axial spin [22]. In addition, results of the cargo transport of planar objects showing backward and forward stages. (b) Results of the reconfigurable carpet [37]. Cargo transport of multiple glass beads and pushing the micro bead through the microchannel. In addition, removal of an attachment in a tube.

2.3 Contribution to state-of-the-art

In our research we aim to create a fabrication-free magnetic carpet from reduced iron microparticles. This makes it possible to create the carpet quickly and easily relocated within the workspace. This thesis provides insights on the height and density of the magnetic carpet, assembled using different parameters, to understand the collective behaviour of the microparticles during generation of the magnetic carpet and actuating such carpet. We take advantage of a nine coil electromagnetic system to test different actuation mechanisms. Non-uniform magnetic fields can be generated without changing the relative distance of the electromagnetic coils with respect to the workspace. Using such fabrication-free magnetic carpet, it is possible to perform cargo transport.

Materials and Methods

In this chapter we discuss (3.1) the BatMag system and (3.2) the used materials in the experiments.

3.1 BatMag System

The experimental setup, called BatMag, is designed and assembled by Ongaro *et al.* [25]. In the next sections we discuss the hardware and software of the BatMag system.

3.1.1 Hardware

The system consists of nine electromagnetic coils [25]. The coils are vested onto a frame as shown in Figure 3.1. The system has four upper coils: coils number 1, 2, 3 and 4 (numbered in red), four lower coils: coils number 5, 6, 7 and 8 (numbered in green) and a bottom coil: coil number 9 (numbered in yellow). The distance of each coil with respect to the middle of the setup can be adjusted. The maximal configuration that can be obtained results in a sphere with a diameter of 160mm. The smallest sphere that can be obtained has a diameter of 50 mm. The coils can be linearly adjusted closer to the middle of the setup with steps of 5mm. The coils are also designed and fabricated by Ongaro *et al.*, therefore, further information about the specifications of the coils can be found in the paper of Ongaro *et al.* [25]. The setup includes two cameras (grasshopper 3, Teledyne FLIR, United States) with zoom modules (Optem Fusion 7:1, Qioptiq, United Kingdom) at the top and right side of the system. The camera's are connected by USB with the desktop, have a framerate of 163 frames per second and have a resolution of 1920 × 1200 pixels. A visual representation of this setup can be seen in Figure 3.1.

A CAN-bus protocol is used to communicate information between the setup and the software using a Graphical User Interface (GUI). The experiments are performed inside a workspace of 22x22x25 mm created from 3 mm thick acrylic panels which is placed on top of a designed platform that levels the workspace at the middle of the setup (see section B.1). More information about the software and hardware of the BatMag system can be found in Appendix B and in the work of Ongaro *et al.* [25].

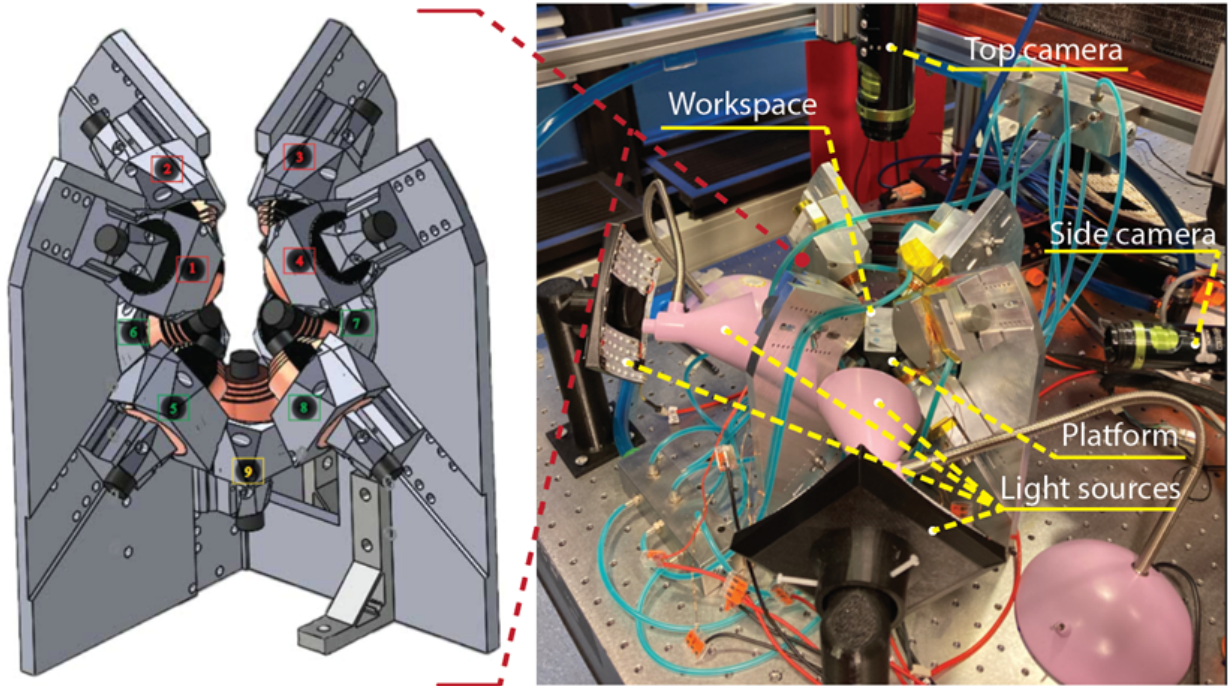


Figure 3.1: Configuration of the nine coils of the BatMag system by Ongaro et al. [25] showing the upper coils: coils number 1, 2, 3 and 4 (red numbered), lower coils: coils number 5, 6, 7 and 8 (green numbered) and bottom coil: coil number 9 (yellow numbered). The BatMag system includes the top and side camera's and the platform holding the workspace in the center of the BatMag system.

3.1.2 Software

An GUI is developed to activate different actuation mechanisms to perform cargo transport. Parameters, such as amplitude, frequency and phase shift, can be defined for each magnetic field inside the GUI. The Coil number 9 is actuated by a static current over time which can be set in the GUI as well (Figure 3.2).

3.2 Used materials

A few materials are used to make the experiments reproducible. The designed workspace is tested waterproof and used in all experiments to contain the reduced iron microparticles and 8 ml of tap water as an aqueous medium. The amount of iron microparticles is measured in mg using a scale. The 8 ml tap water is obtained using a micro liter pipette of 500 - 5000 μl . To obtain 8 ml inside the workspace. the micro liter pipette is set on 4000 μl and then the pipette is used twice to put tap water inside the workspace. Lastly, a spatula is used to stir the solution of iron microparticles and water inside the box to manually distribute the iron particle over the workspace. Specifications of each used material is given in Table 3.1.

In the experiments, planar objects are used as cargo for the cargo transport (shown in Table 3.2). Detailed descriptions of the performed experiments can be found in Appendix C.

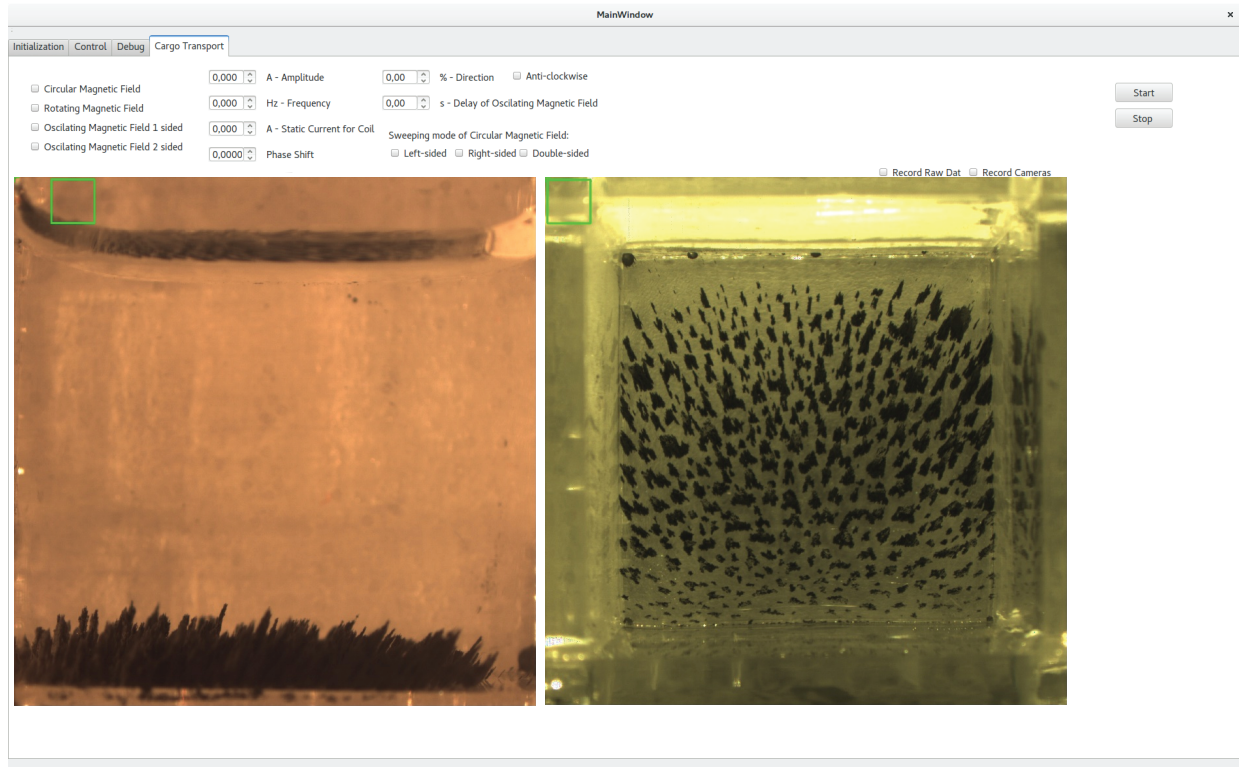


Figure 3.2: Cargo transport tab developed as addition onto the existing GUI developed by Ongaro et al. for cargo transport purposes using different magnetic fields.

Material	Specification	Brand	Origin
Iron microparticles	Reduced iron microparticles, $\geq 99\%$	Sigma-Aldrich	Germany
Microliter Pipette	proMLP, 500-5000 μl	LLG labware	France
Scale	SECURA225D - 1S	Sartorius Lab Instruments GmbH & Co.	Germany
Spatula	"macro spoon - P.P.", 150 mm	ISOLAB Laborgeräte GmbH	Germany

Table 3.1: Used materials during experiments. (The planar object which are also used during experiments are shown in a separate table.)

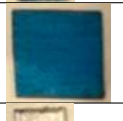
Object	Shape	Dimension	Material	Weight
	Square	3x3 mm	1 layer of PET	0.58 mg
	Square	5x5 mm	1 layer of PET	1.89 mg
	Square	3x3 mm	2 layers of PET	1.38 mg
	Square	5x5 mm	2 layers of PET	4.13 mg
	Square	3x3 mm	4 layers of PET	2.82 mg
	Square	5x5 mm	4 layers of PET	7.79
	Square	3x3 mm	Transparent PET	3.61 mg
	Square	5x5 mm	Transparent PET	9.55 mg
	Triangle	3.5 mm (side length)	2 layer of PET	0.68 mg
	Triangle	3.5 mm (side length)	4 layer of PET	1.90 mg
	Circle	3 mm (diameter)	2 layer of PET	1.68 mg
	Circle	3 mm (diameter)	4 layer of PET	3.83 mg

Table 3.2: Planar objects used in the experiments for cargo transport.

Results and discussion

In this chapter we discuss the (4.1) generation of the magnetic carpet using different currents and amounts of microparticles, also called the static characterisation, and we discuss the dynamic performance of the magnetic carpet using different actuation mechanisms. Thereon, we look into the (4.2) capabilities of the magnetic carpet and the (4.3) cargo transport using the different actuation mechanisms methods.

4.1 Carpet characterisation

The characterisation of the carpet consists of a static characterisation and the dynamic performance. In both cases the carpet is generated by powering a magnetic field with reduced iron microparticles inside the magnetic field.

4.1.1 Static characterisation

The static characterisation is performed to observe the behaviour of the carpet generation using different currents and different amount of reduced iron particles. To observe this behaviour, only coil number 9 is powered with a static current. Results are obtained by taking images of the side view and top view of the carpet. The images obtained from both camera's are processed to calculate the average height and density of the magnetic carpet. The side images are processed in three steps using *MatLab* (version R2020a): (1) the images are converted to grayscale, (2) the image is then binarized and (3) the outline of the pillars is determined in pixels for each column of the image by counting the white pixels (Figure 4.1b). The average height of the pillars is calculated by taking an average of the outline and converting this to micrometers ($1 \text{ pixel} \approx 38 \mu\text{m}$). The results show that the height of the pillars increase when the mass of microparticles increases (Figure 4.1). In addition, the height of the pillars increase according to the currents of coil number 9. Increasing currents on coil number 9 produces an increasing strenght of the resulting magnetic field which results in an increasing pillar height. The longer the pillars, the further the pillars are able to bend and the more they can push which is wanted for the cargo transport.

The images obtained by the top camera are used to characterize the area of pillars for different

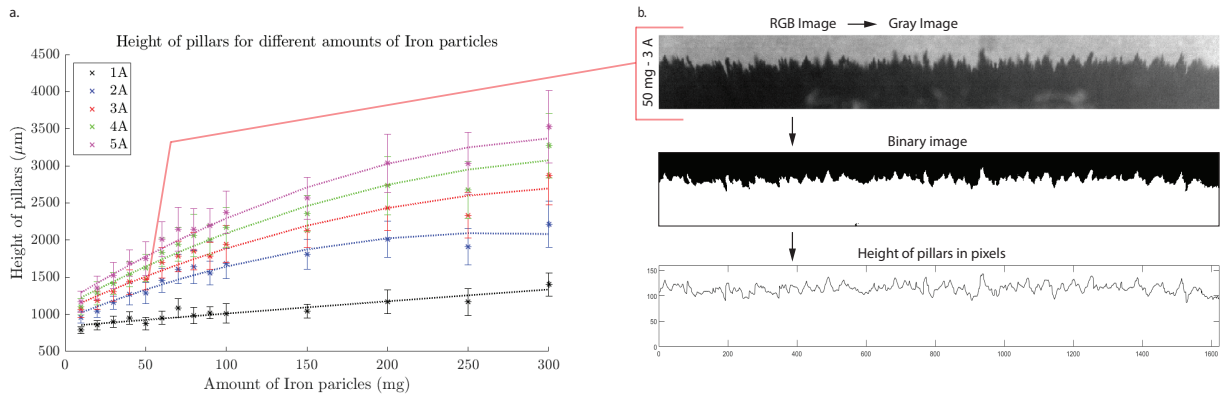


Figure 4.1: (a) Average height of the pillars for different masses of reduced iron microparticles and currents for coil number 9. The height of the pillars increase according to the mass of microparticles and currents on coil number 9. (b) To explain the image processing steps, the image for 50 mg of microparticles and 3 A (for coil number 9) is taken and processed in three steps: converting to gray-scale, binarizing and counting the white pixels for each pixel column in the image.

amounts of iron microparticles and different currents on coil number 9. These images are also processed using *MatLab* (version R2020a) following the next steps: (1) the image is converted to grayscale, (2) the pillars are extracted from the image using morphological top-hat filtering, (3) adjustment of the contrast of the image and (4) the resulting image is binarized. The ratio of the area of the pillars is obtained by dividing the amount of white pixels (pillars) by the total pixels of the image. In each image, three regions of interest (ROI) are used to obtain the density: 2 mm, 5 mm and 10 mm. The regions of interest are centered around the middle of the workspace. It can be observed that for 10 mg to 80 mg of microparticles a linear growth can be found. In these cases, the individual pillars can be clearly seen as shown in Figure 4.2a. However, for amounts of microparticles higher than 80 mg, broader pillars are formed and not all microparticles are used to form the pillars but still cover the bottom of the workspace. For cargo transport we do not want the excess of microparticles when forming the pillars. Therefore, we should use amounts of microparticles upto 80 mg for generating the pillars. For the linear growth between 10 mg to 80 mg, the slopes of these linear functions are calculated (Figure 4.2c). For each ROI the slope is similar over 2 A to 5 A for coil number 9. The slopes for 1 A are quite higher than for the other currents. This can be explained since using 1 A for coil number 9 results in a weaker magnetic field and therefore weaker gradient fields compared to the higher currents for coil number 9. This causes that not all microparticles are used to form the pillars. From the experimental results we decide to limit the mass of microparticles to 80 mg since for cargo transport we want to avoid unitizing of the pillars and the excess of microparticles.

4.1.2 Dynamic performance

The dynamic performance is performed to visualize how the pillars behave collectively using different actuation mechanisms. For this characterisation, the currents for the coils number 1 through

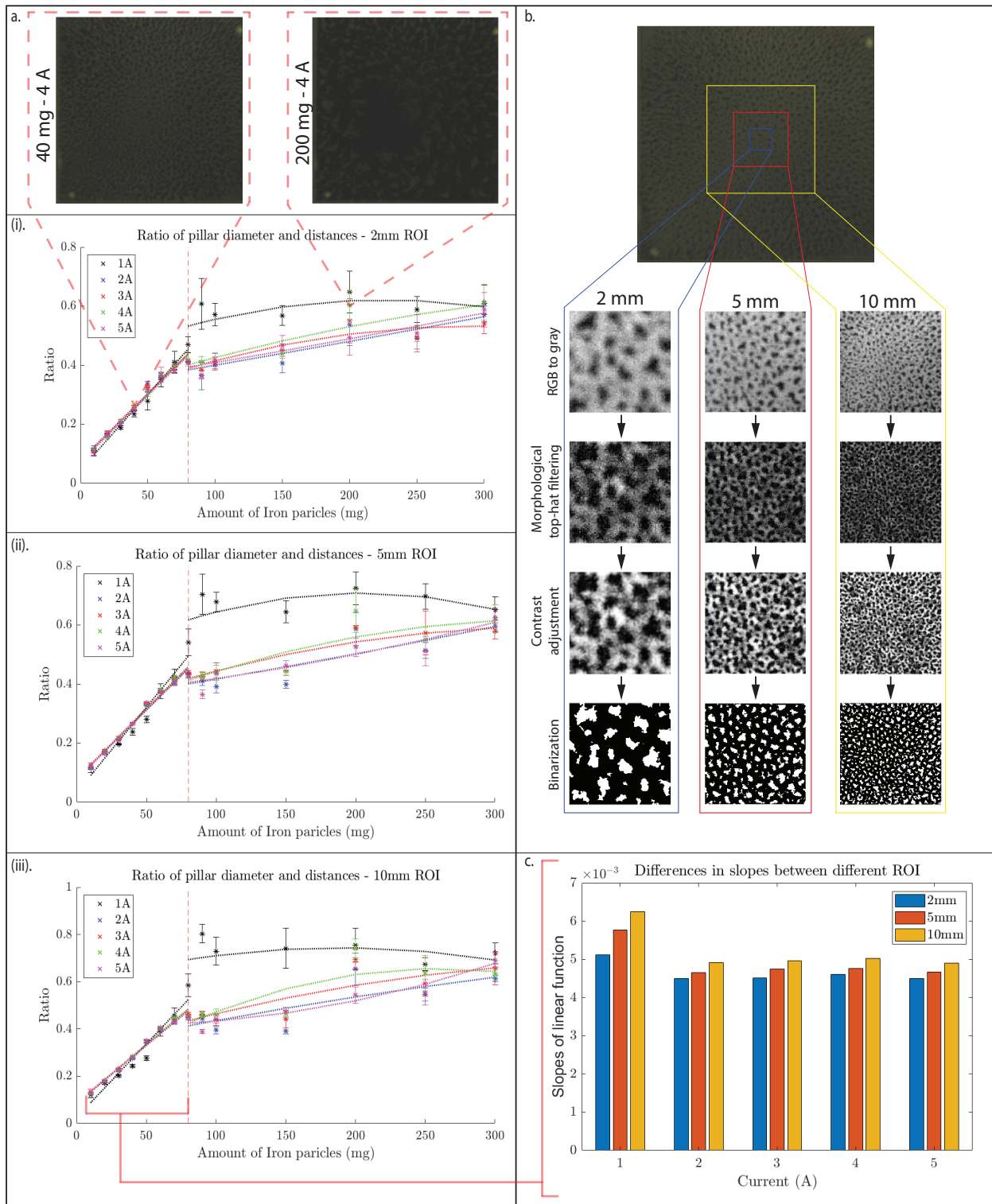


Figure 4.2: (a) Ratio between the area of the pillars in pixels and the total pixels of the image for different ROIs: (i) 2 mm, (ii) 5 mm and (iii) 10 mm. A linear relationship can be found between the ratio and the amount of microparticles for 10 mg to 80 mg. Between these amounts of microparticles, single pillars are observed in the top image. For higher amounts of microparticles, the pillars are unitizing and some microparticles are still covering the bottom of the workspace. (b) The image processing process of these images consists of four steps: (1) converting to gray-scale, (2) morphological top-hat filtering, (3) increasing contrast and (4) binarizing. The ratio is then calculated by dividing the white area in pixels by the total pixels of the image. (c) Slopes are calculated between 10 mg and 80 mg of microparticles. For each current, the slopes of the ROIs are close to each other except for 1 A.

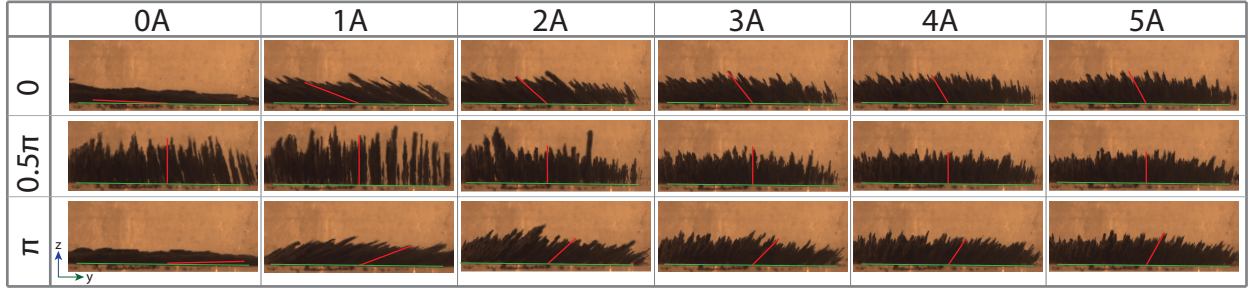


Figure 4.3: The amplitude of the generated oscillating magnetic field is 0.5 A and coil number 9 varies from 0 to 5 A. It can easily be seen that the angle with respect to the y-axis increases and therefore the angle that the carpet moves from left to right is decreased.

8 are calculated using sinusoidal signals while coil number 9 is powered using a constant current. Five actuation mechanisms are designed: horizontal rotating magnetic field (Figure 4.5), vertical rotating magnetic field (Figure 4.6), one-sided oscillating magnetic field (Figure 4.8), two-sided oscillating magnetic field (Figure 4.7) and sweeping magnetic field (Figure 4.11, Figure 4.10 and Figure 4.9). Figure 4.4 shows the angles between the coils and gives each coil a color code. The green plane v indicates the orientation of the magnetic field.

We set the frequency, phase shift and rotating direction of the magnetic field using the GUI. The maximal current for each coil is 5 A and the orientation is given in degrees (0 to 360 degrees), used to calculate the amplitude of each sinusoidal signal to obtain the wanted orientation of the magnetic field. Equation 4.1 and Equation 4.2 calculate the amplitudes of the sinusoidal signals of each coil ($A_c \in \mathbb{R}$) using the orientation ($v \in \mathbb{R}$) and desired resulting amplitude $A_{res} \in \mathbb{R}$.

$$A_{c_i}(v) = \begin{cases} A_{res} \cos(v) & 0^\circ \leq v < 90^\circ \\ -A_{res} \sin(v - 90) & 90^\circ \leq v < 180^\circ \\ -A_{res} \cos(v - 180) & 180^\circ \leq v < 270^\circ \\ A_{res} \sin(v - 270) & 270^\circ \leq v < 360^\circ \end{cases} \quad \text{with } i \in \{1, 3, 5, 7\} \quad (4.1)$$

$$A_{c_j}(v) = \begin{cases} A_{res} \sin(v) & 0^\circ \leq v < 90^\circ \\ A_{res} \cos(v - 90) & 90^\circ \leq v < 180^\circ \\ -A_{res} \sin(v - 180) & 180^\circ \leq v < 270^\circ \\ -A_{res} \cos(v - 270) & 270^\circ \leq v < 360^\circ \end{cases} \quad \text{with } j \in \{2, 4, 6, 8\} \quad (4.2)$$

In the next paragraphs we discuss each actuation mechanism and how the magnetic carpet behaves using these actuation mechanisms. To be able to hold the pillars attached to the bottom of the workspace, coil number 9 has to be powered with at least 4 times the amplitude of the generated magnetic field (typically we use an amplitude of 0.5 A for the generated magnetic field and 2 A for coil number 9 which gives a ratio of $\frac{A_{res}}{A_{c_9}} = \frac{0.5}{2} = \frac{1}{4}$). We see that the angle of the pillars, with respect to the y-axis, increases when the ratio between amplitude and current of coil

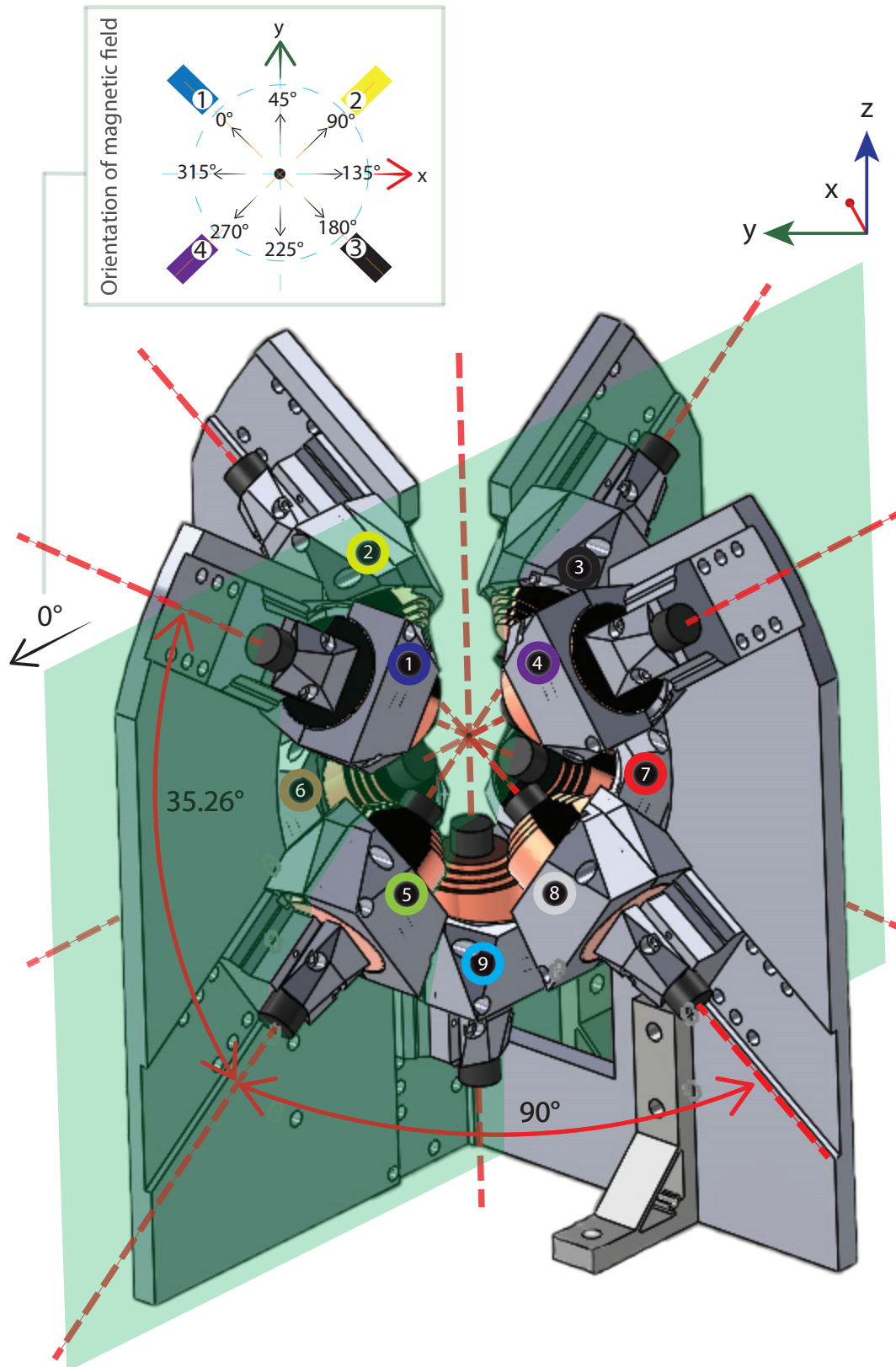


Figure 4.4: Illustration of the BatMag setup with the angles between the coils, the orientation of the BatMag setup and the green 2D plane (intersecting with coils number 1, 3, 5 and 7) which illustrates the orientation of the generated magnetic field. Coil number 9 is powered with a constant current which can be controlled independently from each actuation mechanism.

number 9 decreases (Figure 4.3). There is a trade-off, since we want the carpet to be attached to the bottom of the workspace during the swinging motion of the pillars, achieved by a high ratio. On the other hand, we want the pillars to make a greater motion to reach further for the cargo transport, achieved by a low ratio.

Rotational magnetic fields

Two different rotational magnetic fields are proposed: the horizontal rotating magnetic field and the vertical rotating magnetic field according to the coordinates defined in Figure 4.4. Both rotating magnetic fields are illustrated in Figure 4.6 and Figure 4.5 with a graph of the signals on each coil of one period. In addition, Equation 4.3 and Equation 4.4 are used to generate horizontal and vertical rotating magnetic fields, respectively, with amplitude A , frequency $f \in \mathbb{R}^+$ and phase shift $\phi_{tot} \in \mathbb{R}^{1 \times 4}$ at a certain time $t \in \mathbb{R}^+$. The total phases (ϕ_{tot}) is the sum of the phases (ϕ_{phase}), which is calculated using the unit circle, and the reference phase (ϕ_{ref}) multiplied by the matrix $D \in \mathbb{R}^{4 \times 4}$. In order to control the rotating orientation of the magnetic field, we define the matrix D , where $D = I$ for a clockwise orientation and $D = -I$ for a anti-clockwise orientation and I is the unitary matrix.

$$coil_i = A \cos(2\pi f t + \phi_{tot_i}) \quad \text{with } i \in \{1, 2, 3, 4, 5, 6, 7, 8\} \quad (4.3)$$

$$coil_i = A_i \cos(2\pi f t + \phi_{tot_i}) \quad \text{with } i \in \{1, 3, 5, 7\} \quad (\text{orientation} = 0^\circ) \quad (4.4)$$

$$\phi_{tot_i} = D(\phi_{phase_i} + \phi_{ref}) \quad (4.5)$$

The behaviour of the carpet is shown in Figure 4.6 and Figure 4.5. For the horizontal rotating magnetic field, the pillars are rotating in the horizontal plane. For the vertical rotating magnetic field, the pillars move between 0 and π in the plane of the orientation of the magnetic field. Using MatLab simulations of both rotational magnetic fields are made and described in Appendix D. The simulation of the rotational magnetic fields correspond with the illustrations of the movements of the magnetic carpet in Figure 4.6 and Figure 4.5. In experiments, the pillars bend more outward at the corners of the workspace compared to the middle of the workspace. This behaviour can be explained by the simulations since in the side views of the simulations we see that the magnetic field vectors are also bending more outwards. Since the microparticles align with the flux lines of the magnetic fields, the pillars will align with the simulated magnetic field vectors. The gradient field is pointing downwards (towards coil number 9) for both actuation mechanisms, which results in maintaining the pillar structure.

Oscillating magnetic fields

Two different oscillating magnetic fields are proposed: the one-sided oscillating magnetic field and the two-sided oscillating magnetic field. The two-sided oscillating magnetic field, spans an angle from 0 to $-\pi$. Thereon, the phases of the sinusoidal signals change and the magnetic field is rotating back to the starting point from $-\pi$ to 0 (illustrated in Figure 4.7). The one-sided oscillating magnetic field, spans an angle from 0 to $-\pi$. Then the magnetic field is deactivated until the next

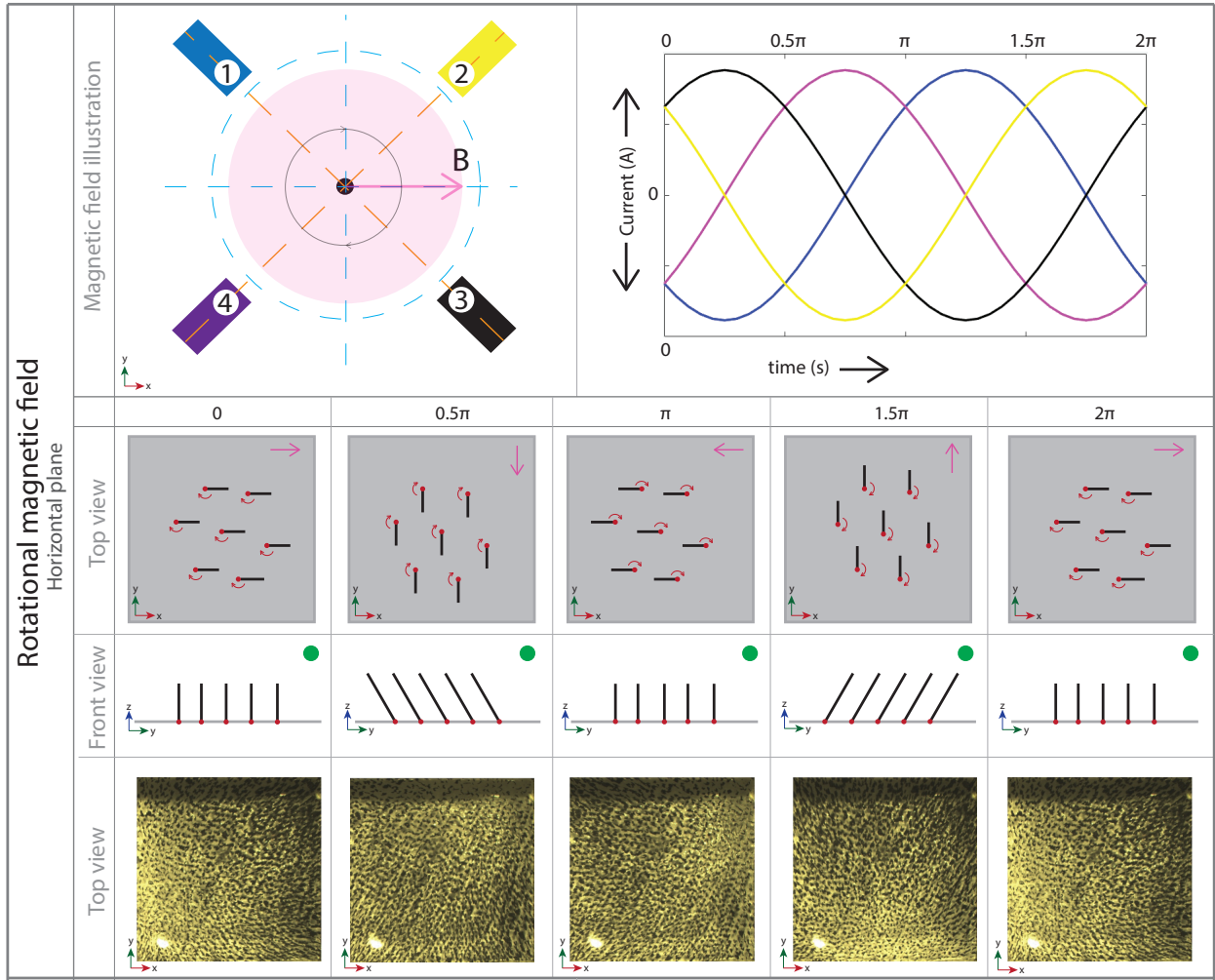


Figure 4.5: Illustration of the horizontal rotating magnetic field inside the setup of BatMag and the signals for the coil pairs number 1-5, number 2-6, number 3-7 and number 4-8. An illustration and camera dumb (where the red dot indicates the point that the pillar is touching the bottom of the workspace) shows the behaviour of the carpet inside this magnetic field. We can observe that the pillars are rotating in the horizontal plane as well. The direction of the magnetic field (pink arrow) is influenced when coil number 9 is powered on (green circles). The current of coil number 9 influences the angle between the y-axis and pillar which is static during the horizontal rotation. If the ratio between amplitude and current of coil number 9 increases, the angle (with respect to the y-axis) will decrease.

period of the sinusoidal signal starts and the magnetic field spans an angle from 0 to $-\pi$ again (illustrated in Figure 4.8). The two-sided oscillating magnetic field can be defined by Equation 4.6 and the sign of the phases changes at 0 and π of its period.

$$coil_i = A_i \cos(2\pi f t + \phi_{tot_i}) \quad \text{with } i \in \{1, 3, 5, 7\} \quad (\text{orientation} = 0^\circ) \quad (4.6)$$

$$\phi_{tot_i} = D(t)(\phi_{phase_i} + \phi_{ref}) \quad (4.7)$$

$$D(t) = \begin{cases} I & 0 < t < \pi \\ -I & \pi < t < 2\pi \end{cases} \quad \text{with } I \in \mathbb{R}^{3 \times 3} \quad (4.8)$$

The one-sided oscillating magnetic field can be defined by Equation 4.9. The one-sided oscil-

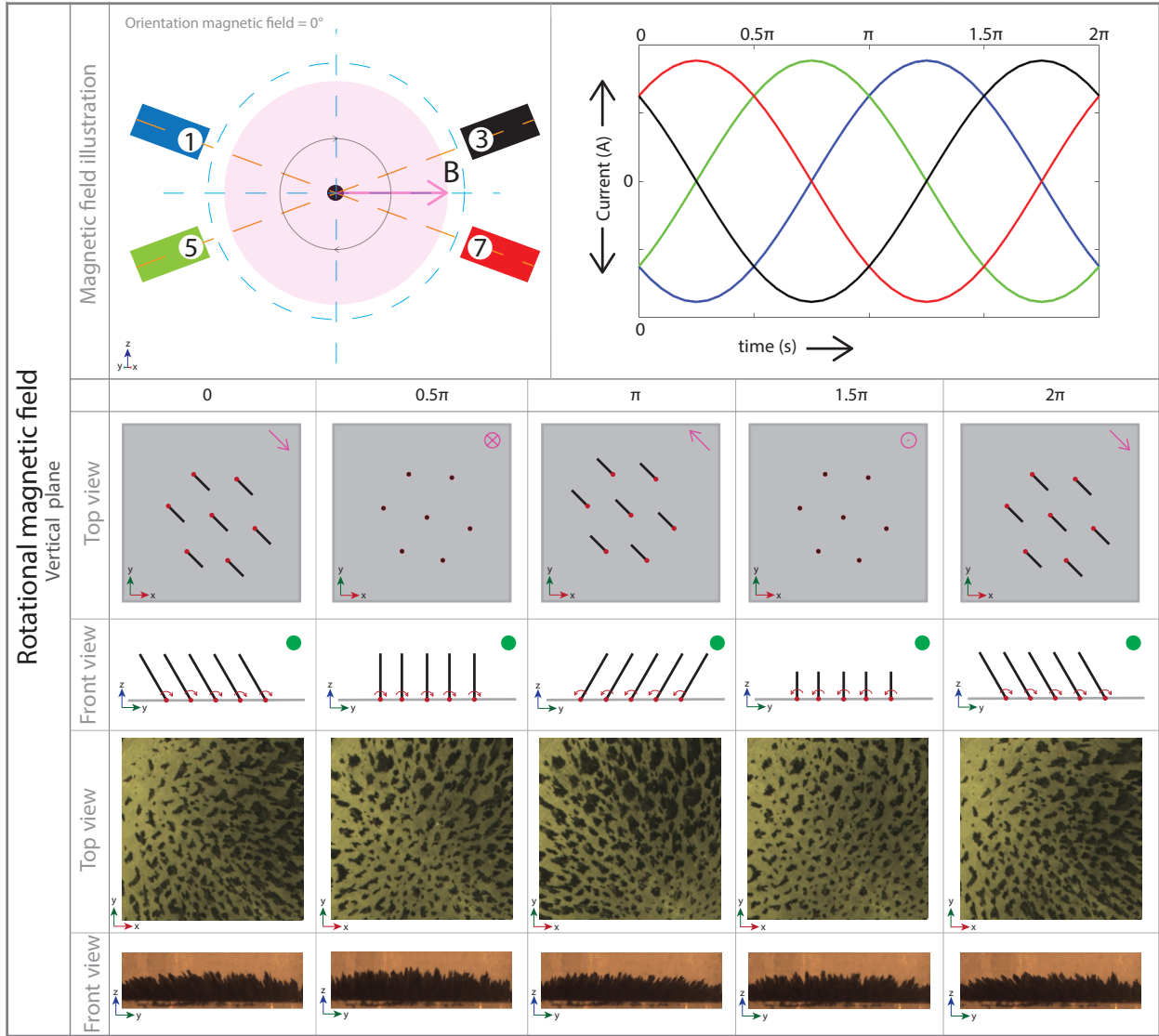


Figure 4.6: Illustration of the vertical rotating magnetic field inside the setup of BatMag with orientation of 0° and the signals for the coils number 1, 3, 5 and 7. An illustration and camera dumb shows the behaviour of the carpet inside this magnetic field. We can observe that the pillars are moving from 0 to π and back to 0 in one period. The direction of the magnetic field (pink arrow) is influenced when coil number 9 is powered on (green circles). The height of the pillars will decrease when the rotating magnetic field becomes positive because the length of the vector of the resulting magnetic field decreases (since the vector of the rotating magnetic field has the opposite sign of the vector of the magnetic field generated by coil number 9).

lating magnetic field only activates the coils from 0 to π of the period and deactivates the coil for the second part of the period.

$$coil_i = \begin{cases} A_i \cos(2\pi f t + \phi_{tot_i}) & 0 < t < \pi \\ 0 & \pi < t < 2\pi \end{cases} \quad \text{with } i \in \{1, 3, 5, 7\} \quad (\text{orientation} = 0^\circ) \quad (4.9)$$

$$\phi_{tot_i} = D(\phi_{phase_i} + \phi_{ref}) \quad (4.10)$$

The difference between this actuation mechanism and the vertical rotating magnetic field is

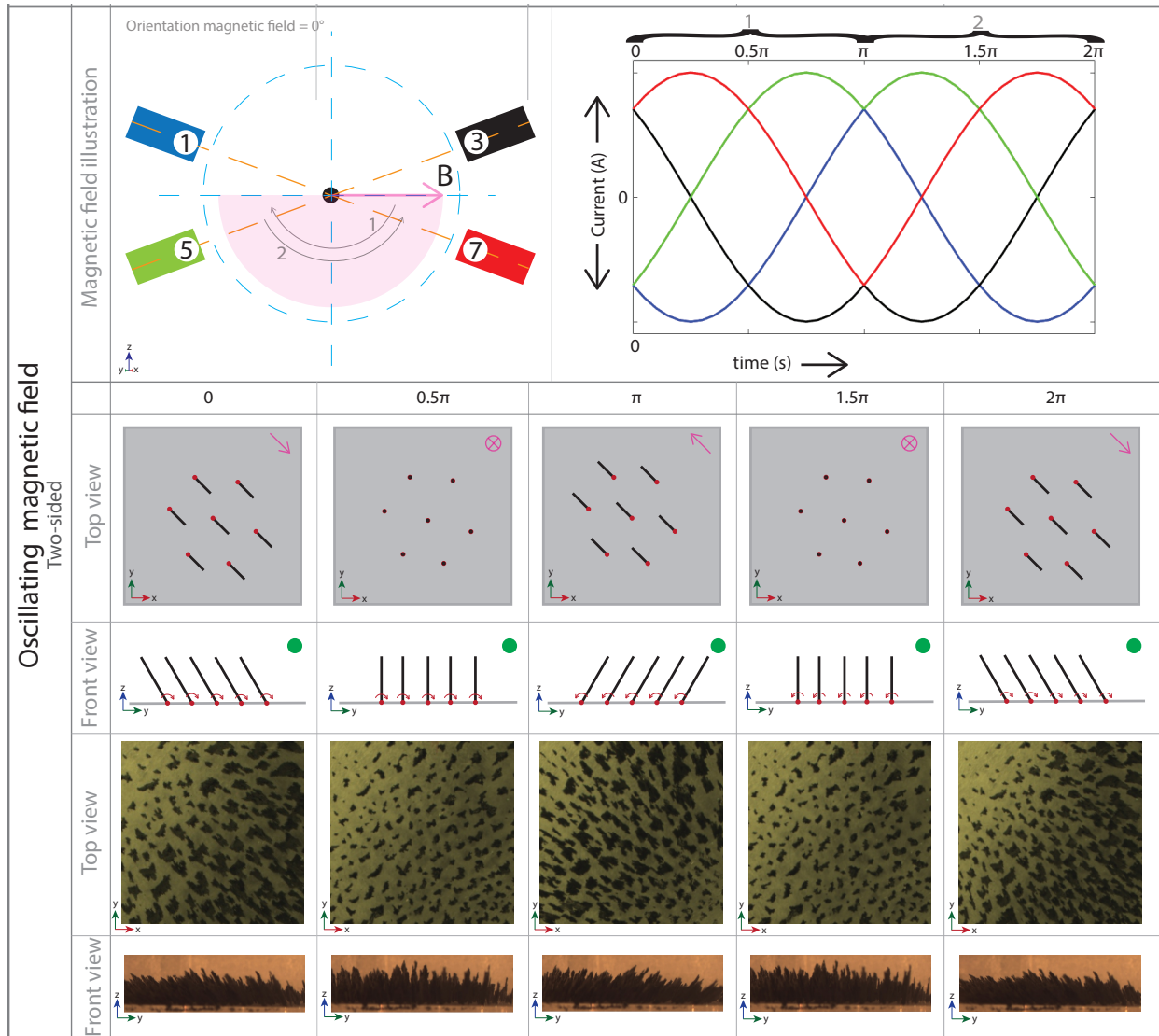


Figure 4.7: Illustration of the two-sided oscillating magnetic field inside the BatMag setup with an orientation of 0° and the signals for coils number 1, 3, 5 and 7. An illustration and camera dumb shows the behaviour of the carpet inside this magnetic field. We can observe that the pillars span an angle between 0 and π back and forth in one period. On the contrary to the rotating magnetic field, the vector of the two-sided oscillating magnetic field will always have a negative sign and, therefore, the magnitude of the vector of the resulting magnetic field will not change between the first and second half of the period which results in a static pillar length during the period. The current of coil number 9 influences the angle between the y -axis and pillar. If the ratio between amplitude and current of coil number 9 increases, the angle (with respect to the y -axis) will decrease.

that the direction of the two-sided oscillating magnetic field is always negative (between 0 and $-\pi$). In addition, when coil number 9 is deactivated the pillars will still be attached to the bottom of the workspace (but the pillars move outwards) and the pillars will span an angle of 180° . For the vertical rotating magnetic field, the pillars are not attached to the bottom of the workspace and span an angle of 360° when coil number 9 is deactivated.

Simulations of the oscillating magnetic fields are performed using MatLab and described in

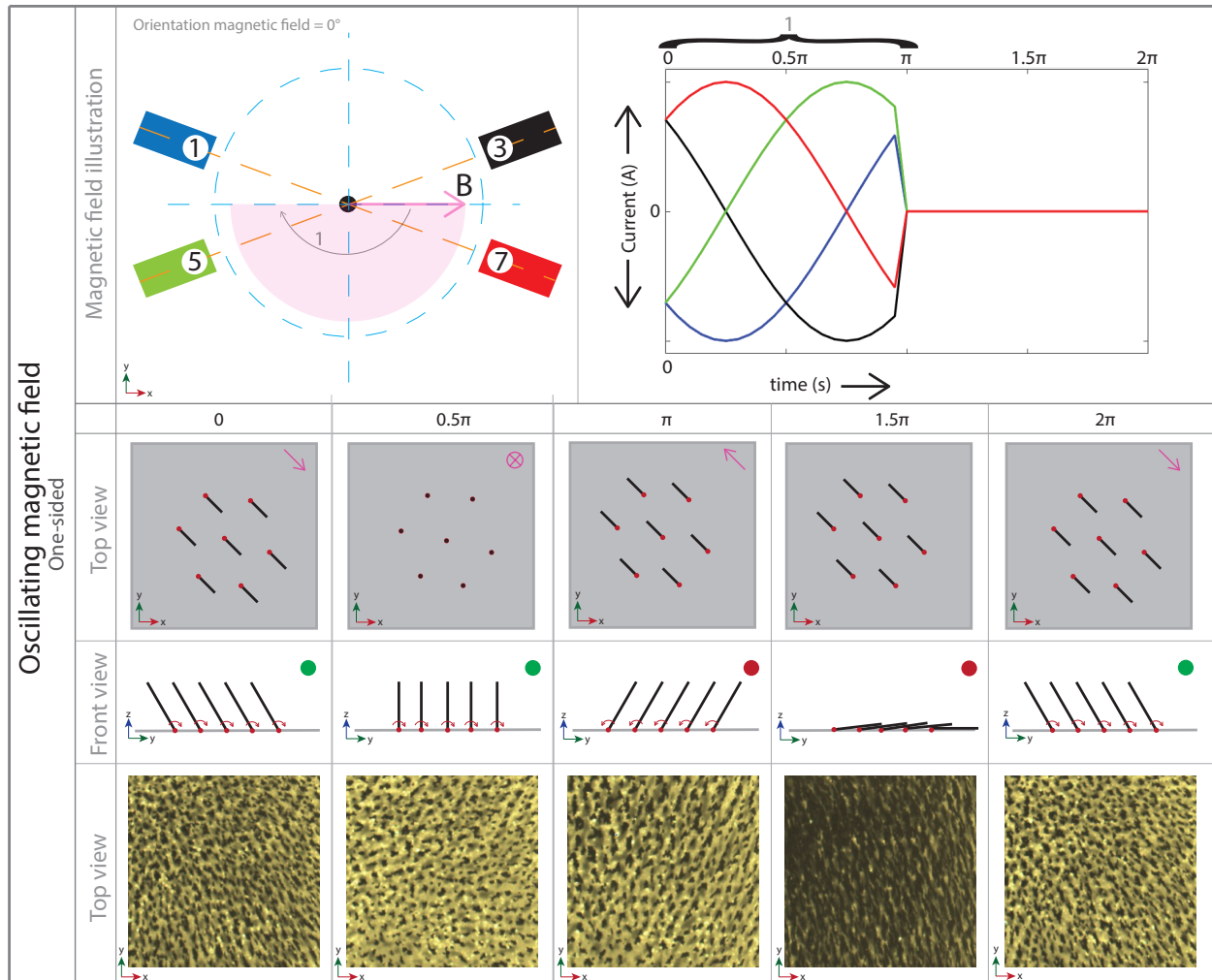


Figure 4.8: Illustration of the one-sided oscillating magnetic field inside the BatMag setup (with an orientation of 0°) and the signals for coils number 1, 3, 5 and 7. An illustration and camera dumb shows the behaviour of the carpet inside this magnetic field. We can observe that the pillars are moving between 0 and π and the magnetic field is deactivated the second half of period (red circles). The direction of the magnetic field (pink arrow) is influenced when coil number 9 is powered on (green circles). The current of coil number 9 influences the angle between the y -axis and pillar. If the ratio between amplitude and current of coil number 9 increases, the angle (with respect to the y -axis) will decrease.

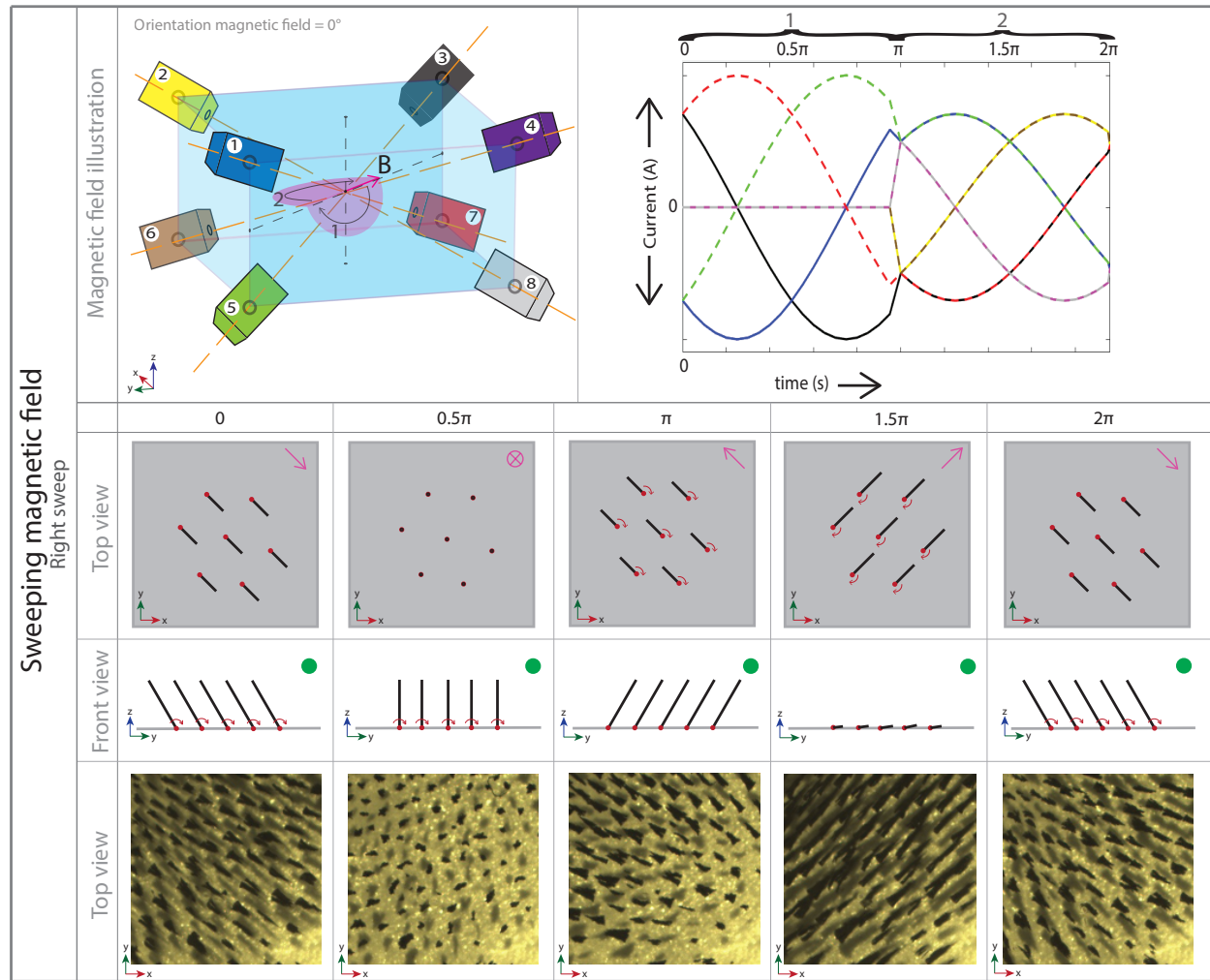


Figure 4.9: Illustration of the right-sided sweeping magnetic field inside the BatMag setup with an orientation of 0° and the signals for each coil. An illustration and camera dumb shows the behaviour of the carpet inside this magnetic field. We can observe that the pillars are moving between 0 and π in the vertical plane. Then in the second half of the period, the pillars are moving back to the initial point by rotating on the right side of the pillars in the horizontal plane. The current of coil number 9 influences the angle between the y -axis and pillar in the first half of the period. If the ratio between amplitude and current of coil number 9 increases, the angle (with respect to the y -axis) will decrease. In the second half of the period, the ratio is 1 to obtain a sweep over the bottom of the workspace.

Appendix D. Again, the pillars are aligning with the magnetic flux lines and the pillars bend more outward at the corners of the workspace compared to the middle of the workspace, due to the magnetic field vectors as shown in the simulations. Also, the gradient field is pointing downwards (towards coil number 9) for both actuation mechanisms, which results in maintaining the pillar structure.

Sweeping magnetic fields

Inspired by the work of Demirörs *et al.* [13], we propose three different sweeping actuation mechanisms: the right-sweeping (Figure 4.9), the left-sweeping (Figure 4.10) and the two-sided sweeping (Figure 4.11). Each option of the sweeping magnetic field consists of two parts. The first part (first

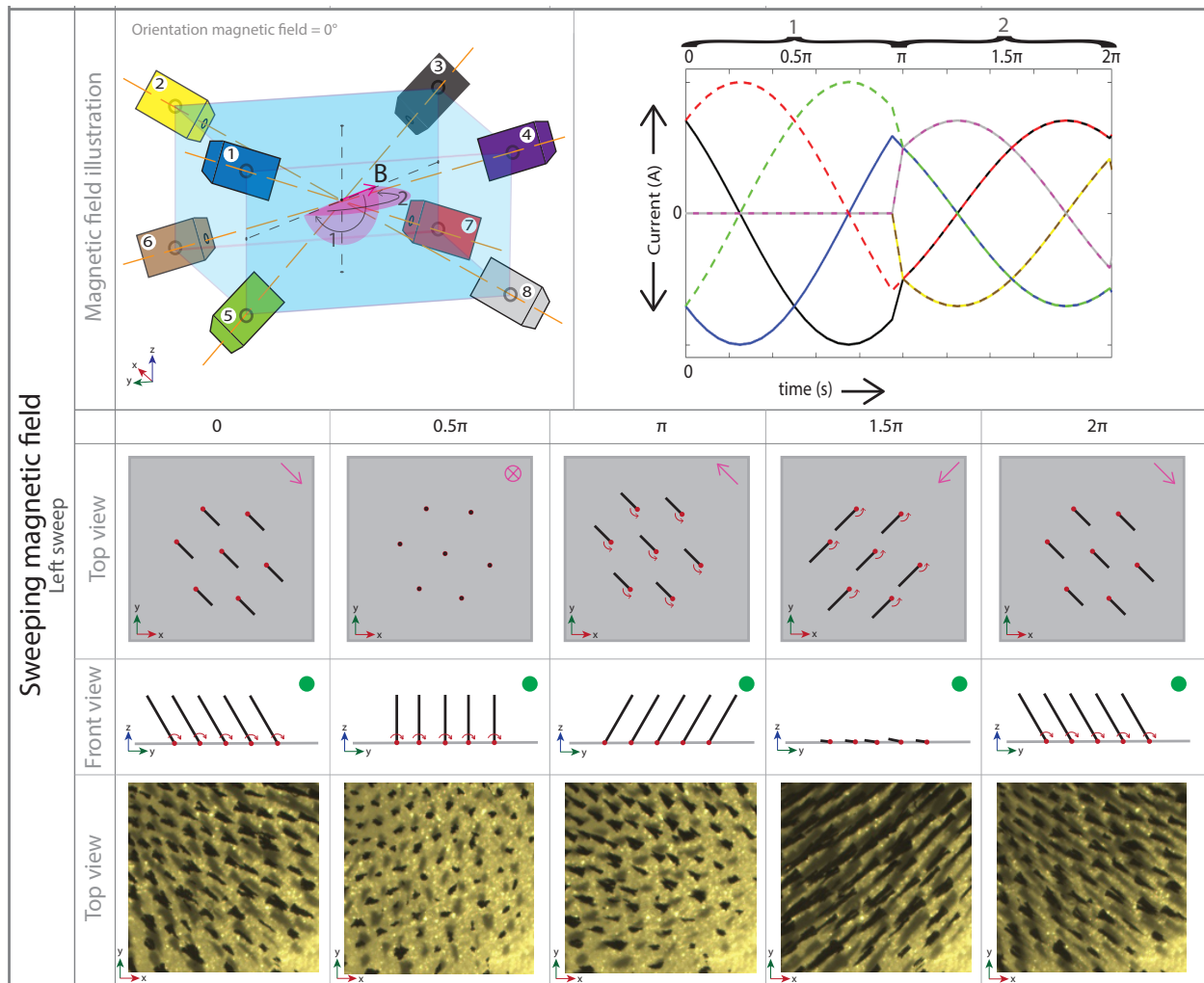


Figure 4.10: Illustration of the left-sided sweeping magnetic field inside the BatMag setup with an orientation of 0° and the signals for each coil. An illustration and camera dumb shows the behaviour of the carpet inside this magnetic field. We can observe that the pillars are moving between 0 and π in the vertical plane. Then in the second half of the period, the pillars are moving back to the starting point by rotating on the left side of the pillars in the horizontal plane. The current of coil number 9 influences the angle between the y -axis and pillar in the first half of the period. If the ratio between amplitude and current of coil number 9 increases, the angle (with respect to the y -axis) will decrease. In the second half of the period, the ratio is 1 to obtain a sweep over the bottom of the workspace.

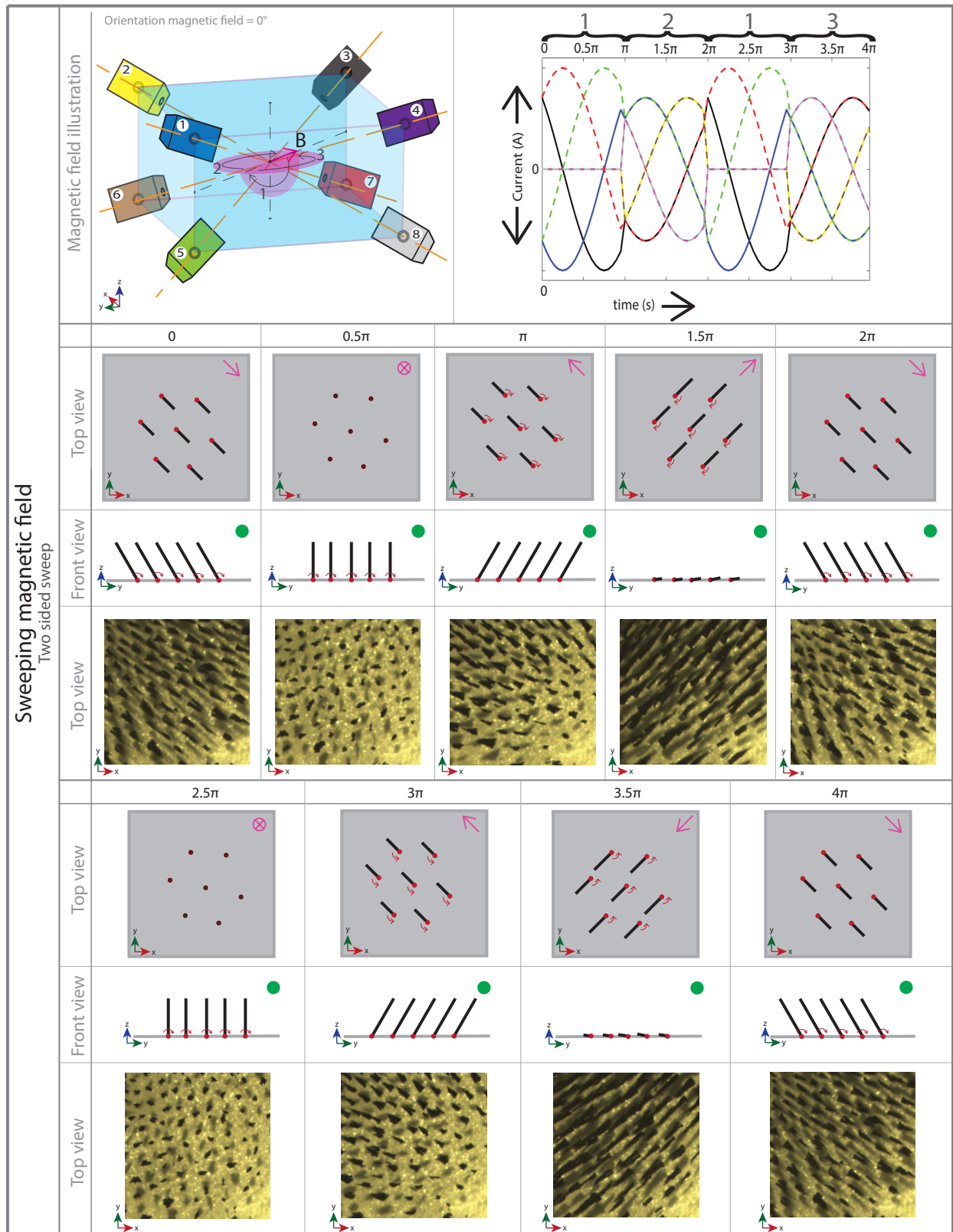


Figure 4.11: Illustration of the two-sided sweeping magnetic field inside the BatMag setup with an orientation of 0° and the signals for each coil. An illustration and camera dumb shows the behaviour of the carpet inside this magnetic field. We can observe that the pillars are moving between 0 and π in the vertical plane. Then in the second half of the period, the pillars are moving back to the starting point by rotating on the right and left side of the pillars alternately in the horizontal plane. The current of coil number 9 influences the angle between the y-axis and pillar in the first half of the period. If the ratio between amplitude and current of coil number 9 increases, the angle (with respect to the y-axis) will decrease. In the second half of the period, the ratio is 1 to obtain a sweep over the bottom of the workspace.

half of the period) the magnetic field rotates from 0 to $-\pi$ in the vertical plane. In the second part (second half of the period) the magnetic field rotates back to the initial point in the horizontal plane. The right- and left-sweeping options decide whether the pillars sweep back to the initial point on the left or right side of the pillars. The two-sided sweep option results in pillars that sweep back to the starting point on the left and right side alternately. The sweeping magnetic field can be defined by Equation 4.11. The sweeping option is selected by modifying the sign of $S \in \mathbb{R}$. For the two-sided sweeping option, the sign of S toggles each period.

$$coil_i = \begin{cases} A_i \cos(2\pi f t + \phi_{tot_i}) & 0 < t < \pi, \quad i \in \{1, 3, 5, 7\} \\ A \cos(2\pi f t + \phi_{tot_i}) & \pi < t < 2\pi, \quad i \in \{1, 2, 3, 4, 5, 6, 7, 8\} \end{cases} \quad (\text{orientation} = 0^\circ) \quad (4.11)$$

$$\phi_{tot_i} = \begin{cases} D(\phi_{phase_i} + \phi_{ref}) & 0 < t < \pi \\ S D(\phi_{phase_i} + \phi_{ref}) & \pi < t < 2\pi \end{cases} \quad (4.12)$$

$$S = \begin{cases} 1 & \text{Right sweep option} \\ -1 & \text{Left sweep option} \\ 0 - s(t) & \text{Two-sided sweep option, } s(0) = 1, \quad s(t) \in \{-1, 1\} \end{cases} \quad (4.13)$$

The behaviour of the carpet in each sweeping magnetic field option is shown in Figure 4.9, Figure 4.10 and Figure 4.11. For the first part of the period, coil number 9 is activated to hold the pillars attached to the bottom of the workspace. For the second part of the period, coil number 9 is powered with a lower current (typically 0.5 A or 1 A) to decrease the angle of the pillars with respect to y-axis as much as possible while the pillars are still attached to the bottom of the workspace.

Simulations of the sweeping magnetic fields are performed using MatLab and described in Appendix D. Again, the pillars are aligning with the magnetic flux lines and the pillars bend more outward at the corners of the workspace compared to the middle of the workspace, due to the magnetic field vectors as shown in the simulations. Also, the gradient field is pointing downwards (towards coil number 9) for the three actuation mechanisms, which results in maintaining the pillar structure.

4.2 Transport of non-magnetic planar objects

The previously presented actuation mechanisms are tested with the aim to perform cargo transport of the planar objects, introduced in the materials and methods (chapter 3). In this section we evaluate the performance of the cargo transport for each planar object using the different actuation mechanisms.

4.2.1 Lifting planar objects with different weights

We start with testing whether the magnetic carpet is able to carry the planar objects. In experiments, we state that all planar objects are carried by the carpet. Therefore, the maximum load that the carpet can carry is not experimentally observed. We observe that for the transparent planar objects (with weights of 3.61 mg for the 3x3 dimension and 9.55 mg for the 5x5 dimension) loose pillars underneath the planar object, that were initially under the object, over time. At a certain point in time, no pillars remain underneath the planar object. The magnetic carpet cannot move the planar object on top of its pillars but tends to push the planar object instead.

4.2.2 Displacement of the planar objects

We previously demonstrated that the magnetic carpet can carry all the planar objects of Table 3.2. In order to investigate which actuation mechanism is suitable for cargo transporting applications, we evaluate parameters as the displacement and velocity of the planar objects within a period of time. The position of the planar object is tracked for each actuation mechanism over time. For the one-sided oscillating magnetic field and sweeping magnetic fields, the objects are tracked until a wall of the workspace is reached. For the rotational magnetic field and two-sided oscillating magnetic field, the objects are tracked for 25 seconds. The displacements of each object for each actuation mechanism are shown in Appendix E. The displacement of the objects is influenced by the initial position of the object inside the workspace since the pillars behave differently at each location inside the workspace. When the pillars bend due to the magnetic field, the planar object is pushed by the tips of the pillars and the contact of new pillars is increased which makes the planar object displace. However, when the tips of the pillars are pushing the planar object into opposite direction with similar forces, the planar object is not leaving its initial position which is the case for the two-sided oscillating magnetic field. For each actuation mechanism (except the one-sided oscillating magnetic field) the carpet moves back and forth. This behaviour can clearly be observed in the graphs of the displacements of the planar objects into the x- and y-direction (Appendix E). Table 4.1 and Table 4.2 show for each planar object the average velocity in x- and y-direction and the calculated frequency of the planar object moving back and forth (due to the swinging movements of the pillars) for each actuation mechanism.

Table 4.1 and Table 4.2 show that the rotational magnetic field in the vertical plane and the two-sided oscillating magnetic field are the least effective for cargo transport compared to the other actuation mechanisms. On the contrary, the one-sided oscillating magnetic field is an effective actuation mechanism. This is also the only actuation mechanism in which the object is not moving back and forth. When the field is deactivated in the second half of the period, the object falls down to the bottom of the workspace and is lifted by the carpet when the field is activated again. However, this type of actuation has a disadvantage. The carpet moves through the workspace because of the second half of the period where the field is deactivated. In this part of the period, microparticles can easily pile up on the planar object. Over time, all pillars are moved over the object and less pillars are left underneath the planar object. This makes it difficult to exhibit motion of the planar object. However, when there are no pillars underneath the planar object, the pillars

Rotational magnetic field				
Object	Velocity in x-direction ($\mu\text{m/s}$)	Frequency (Hz)	Velocity in y-direction ($\mu\text{m/s}$)	Frequency (Hz)
1 layer PET - 3x3	25.96	0.71	15.48	0.71
2 layer PET - 3x3	27.20	0.71	11.32	0.71
4 layer PET - 3x3	14.96	0.71	12.26	0.71
Transparent PET - 3x3	19.53	0.72	24.97	0.72
1 layer PET - 5x5	49.59	0.73	1.46	0.73
2 layer PET - 5x5	37.61	0.71	4.80	0.71
4 layer PET - 5x5	27.53	0.73	30.43	0.73
Transparent PET - 5x5	52.71	0.77	5.00	0.77
Two-sided oscillating magnetic field				
Object	Velocity in x-direction ($\mu\text{m/s}$)	Frequency (Hz)	Velocity in y-direction ($\mu\text{m/s}$)	Frequency (Hz)
1 layer PET - 3x3	14.69	0.72	9.70	0.72
2 layer PET - 3x3	10.23	0.71	5.31	0.71
4 layer PET - 3x3	8.06	0.72	2.08	0.72
Transparent PET - 3x3	7.08	0.64	0.57	0.71
1 layer PET - 5x5	4.48	0.73	3.10	0.73
2 layer PET - 5x5	13.07	0.73	2.77	0.73
4 layer PET - 5x5	4.11	0.71	6.10	0.71
Transparent PET - 5x5	13.25	0.75	0.72	0.75
One-sided oscillating magnetic field				
Object	Velocity in x-direction ($\mu\text{m/s}$)	Frequency (Hz)	Velocity in y-direction ($\mu\text{m/s}$)	Frequency (Hz)
1 layer PET - 3x3	180.89	-	62.84	-
2 layer PET - 3x3	281.49	-	158.31	-
4 layer PET - 3x3	215.62	-	115.41	-
Transparent PET - 3x3	100.52	-	127.86	-
1 layer PET - 5x5	271.95	-	150.09	-
2 layer PET - 5x5	282.53	-	94.82	-
4 layer PET - 5x5	241.76	-	174.70	-
Transparent PET - 5x5	246.31	-	157.22	-

Table 4.1: Average velocities of each planar object for the rotational and oscillating magnetic fields. In addition, the frequencies of the planar object moving back and forth (caused by the swinging movements of the pillars) in x- and y-direction are shown as well for each actuation mechanism. This frequency is calculated from the experimental data obtained by using a tracking algorithm in MatLab.

Left-sided sweeping magnetic field				
Object	Velocity in x-direction ($\mu\text{m/s}$)	Frequency (Hz)	Velocity in y-direction ($\mu\text{m/s}$)	Frequency (Hz)
1 layer PET - 3x3	22.37	0.72	54.40	0.72
2 layer PET - 3x3	47.39	0.73	6.43	0.73
4 layer PET - 3x3	8.02	0.72	63.20	0.72
Transparent PET - 3x3	7.98	0.71	79.69	0.72
1 layer PET - 5x5	9.81	0.73	73.95	0.73
2 layer PET - 5x5	8.21	0.73	81.84	0.72
4 layer PET - 5x5	22.12	0.73	65.05	0.73
Transparent PET - 5x5	92.23	0.68	90.04	0.75
Right-sided sweeping magnetic field				
Object	Velocity in x-direction ($\mu\text{m/s}$)	Frequency (Hz)	Velocity in y-direction ($\mu\text{m/s}$)	Frequency (Hz)
1 layer PET - 3x3	95.40	0.74	14.98	0.69
2 layer PET - 3x3	87.08	0.75	34.34	0.75
4 layer PET - 3x3	149.49	0.70	41.40	0.70
Transparent PET - 3x3	73.34	0.72	28.48	0.72
1 layer PET - 5x5	179.69	0.72	73.47	0.72
2 layer PET - 5x5	258.84	0.72	44.55	0.72
4 layer PET - 5x5	240.25	0.72	62.17	0.72
Transparent PET - 5x5	192.65	0.75	59.15	0.75
Two-sided sweeping magnetic field				
Object	Velocity in x-direction ($\mu\text{m/s}$)	Frequency (Hz)	Velocity in y-direction ($\mu\text{m/s}$)	Frequency (Hz)
1 layer PET - 3x3	72.97	0.36	62.83	0.71
2 layer PET - 3x3	86.96	0.36	37.00	0.72
4 layer PET - 3x3	85.17	0.36	82.86	0.72
Transparent PET - 3x3	48.25	0.36	29.70	0.72
1 layer PET - 5x5	58.23	0.36	107.13	0.73
2 layer PET - 5x5	112.93	0.36	113.70	0.72
4 layer PET - 5x5	98.34	0.36	80.63	0.72
Transparent PET - 5x5	94.27	0.38	105.91	0.76

Table 4.2: Average velocities of each planar object for the sweeping magnetic fields. In addition, the frequencies of the planar object moving back and forth (caused by the movements of the pillars) in x- and y-direction are shown as well for each actuation mechanism. This frequency is calculated from the experimental data obtained by using a tracking algorithm in MatLab.

are still able to move the planar object by pushing.

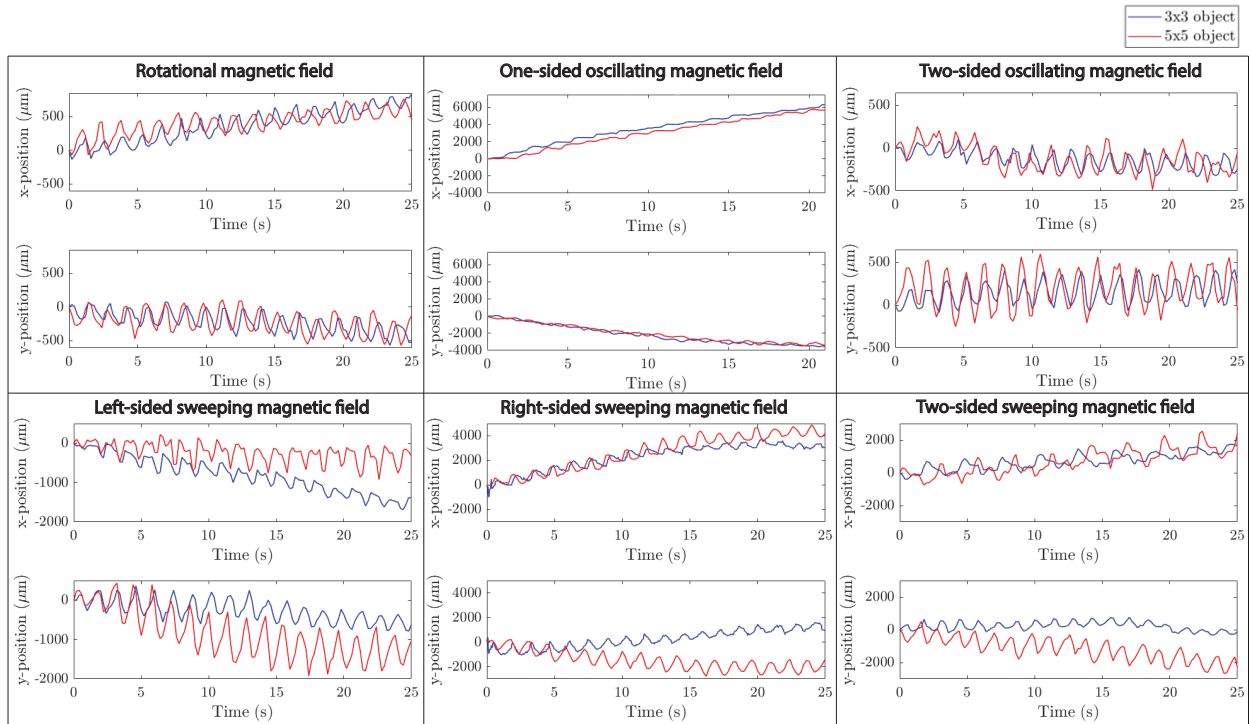


Figure 4.12: Planar objects with similar weight but different size: 3 mm planar object of 1.38 mg and 5 mm planar object of 1.89 mg. The displacements of both planar objects are similar for the rotational, one-sided oscillating and two-sided oscillating magnetic fields. For the sweeping magnetic field, it can be observed that the displacements are still similar but the 5 mm planar object has a bigger displacement compared to the 3 mm planar object.

Another effective actuation mechanism for the cargo transport is the sweeping magnetic field. This actuation mechanism tends to move the planar object into a direction perpendicular to the orientation of the magnetic field. For the two-sided sweeping magnetic field, it would be expected that the planar object stays in place since the left and right sweep are into opposite directions. In the results of Appendix E we observe that this is not the case. We observe that the planar object is moving to the lower right corner. For the left sweeping magnetic field the planar object is moving towards the lower left corner. This can be explained since each coil is powered by a current and therefore the magnetic field is not uniform. In experiments, it is observed that the pillars on the right lower corner are bending more than the pillars on the other corners which means that the magnetic field is stronger at that corner. Therefore, the direction of the movement of the planar object cannot be controlled precise. The planar objects also make small rotations on the tips of the carpet and around their own axis using the right- or left-sided sweeping magnetic field. The rotations on the tips of the carpet is caused by the sweeping part of the magnetic fields. The tips of the pillars are in contact with the planar objects and when the pillars change to the sweeping part of the period, the planar object is pushed to that side as well and follows the motion of the pillars. The rotation of the planar objects around their own axis is caused during the sweeping part of the period as well but by the pillars that touch the sides of the planar objects. During the

sweeping part of the period, the pillars are rotating around their own axis due to the gradient field. These pillars push against the planar object which results in the planar objects to rotate around their own axis.

In order to analyze the oscillatory motion experienced by the planar objects for each actuation mechanism, we calculated the frequency of the displacements in the x- and y-direction and is shown in Table 4.1 and Table 4.2 for each actuation mechanism. The frequency of the oscillatory motion of the planar objects is around 0.72 Hz while in software a frequency of 0.5Hz is used to calculate the currents. This suggests a possible slip between the object and the pillars and includes the error propagation of the tracking algorithm. After analyzing the signal of currents to each coil, we find that the frequency of this signal is approximately 0.61 Hz instead of 0.5 as programmed in the software. For the two-sided sweeping magnetic field, the frequency is approximately 0.36 Hz for the displacement in the y-direction and 0.72 for the displacement in the x-direction. This can be explained since the sweeping side changes alternately between left and right which means that a full cycle of this actuation mechanism is two periods, resulting in half the frequency of the planar object moving back and forth.

Two planar objects with different size but similar weight are compared in Figure 4.12 (the 3x3 mm dimension object has a weight of 1.38 mg and the 5x5 mm dimension object has a weight of 1.89 mg). Both objects show similar behaviour graphs of the displacements in the x- and y-directions. For the right sweeping magnetic field and two-sided sweeping magnetic field, the 5x5 mm dimension planar object is moving further into the y-direction than the 3x3 mm dimension planar object (approximately 2380 μm for the right sweeping magnetic field and approximately 2170 μm for the two-sided sweeping magnetic field).

4.3 Proof-of-concepts using the carpet

To show the capabilities of the carpet we use three different actuation mechanisms to perform rotation and 2D motion of the planar objects and relocation of the carpet within the workspace. In addition, we decided to add circular and triangular planar objects to demonstrate with different shapes.

4.3.1 Rotation of a planar object

Figure 4.13 shows the behaviour of the 5 mm and 3 mm squared planar object, a circular planar object (with diameter of 3 mm) and a triangular planar object (3.5 mm side-length) using a rotational magnetic field in horizontal plane. The objects are placed in the middle of the workspace and then the horizontal rotating magnetic field is activated. Each object rotates around its own axis and the object tends to spiral out from the middle of the workspace. The squared planar objects spiral out further compared to the circular and triangular planar object. On the other hand, the angle of the circular object rotating around its own axis (approximately -1037°) is larger than

the angles reached by the other objects (approximately -339° for the 3 mm squared object, approximately -197° for the 5 mm squared object and approximately -325° for the triangular object). The direction of the rotation and the direction of the spiraling out is in the opposite direction of the rotation of the pillars of the carpet. This behaviour can be explained by the interaction between the planar object and the pillars. Besides the rotation in the horizontal plane, the pillars are also rotating around their own axis. The pillars that are touching the sides of the planar objects push during the rotation around their own axis against the planar object which makes the planar object rotate in the opposite direction.

4.3.2 Moving the planar objects into two dimensions

Using the same planar objects (circular, triangular, 3 mm squared and 5 mm squared), the sweeping magnetic field is used to move the objects into two dimensions inside the workspace. For this demonstration the objects are placed in the right upper corner and are moved towards the middle of the workspace by using the left-sweeping magnetic field with an orientation of 0° . The objects are moving towards the middle of the workspace which is perpendicular to the orientation of the magnetic field. When the objects reach the middle of the workspace, the orientation of the magnetic field is changed to 90° and the objects move towards the lower right corner by using the right-sweeping magnetic field as shown in Figure 4.15 and Figure 4.14.

The circular planar object moves towards the middle of the workspace and the orientation of the magnetic field is changed at approximately 43 seconds. The sweeping magnetic field makes the objects rotate around its own axis as well during movement. After activating the magnetic field it takes approximately 2 seconds until the circular planar object starts moving on the carpet and approximately 12 seconds to start rotating around its own axis. Within the 43 seconds, an angle of approximately -305° is reached. Between 43 seconds and 80 seconds an angle of approximately 427° is reached. The circular object rotates with an average speed of 0.19 rad/s around its own axis and moves with an average speed of $217.36 \mu\text{m/s}$.

The orientation of the magnetic field is changed at approximately 64 seconds for the triangular planar object. After activating the magnetic field it takes the triangular object approximately 2 seconds to start moving and approximately 20 seconds to start rotating around its own axis. Within 64 seconds an angle of -185° is reached. Between 64 seconds and 108 seconds an angle of approximately 121° is reached. The triangular object rotates with an average speed of 0.07 rad/s around its own axis and moves with an average speed of $140.06 \mu\text{m/s}$.

The orientation of the magnetic field is changed at approximately 20 seconds for the 3 mm squared planar object. After activating the magnetic field it takes the squared object approximately 2 seconds to start moving and approximately 12 seconds to start rotating around its own axis. Within 68 seconds an angle of -142° is reached. Between 68 seconds and 110 seconds an angle of approximately 62° is reached. The squared object rotates with an average speed of 0.02 rad/s around its own axis and moves with an average speed of $132.21 \mu\text{m/s}$.

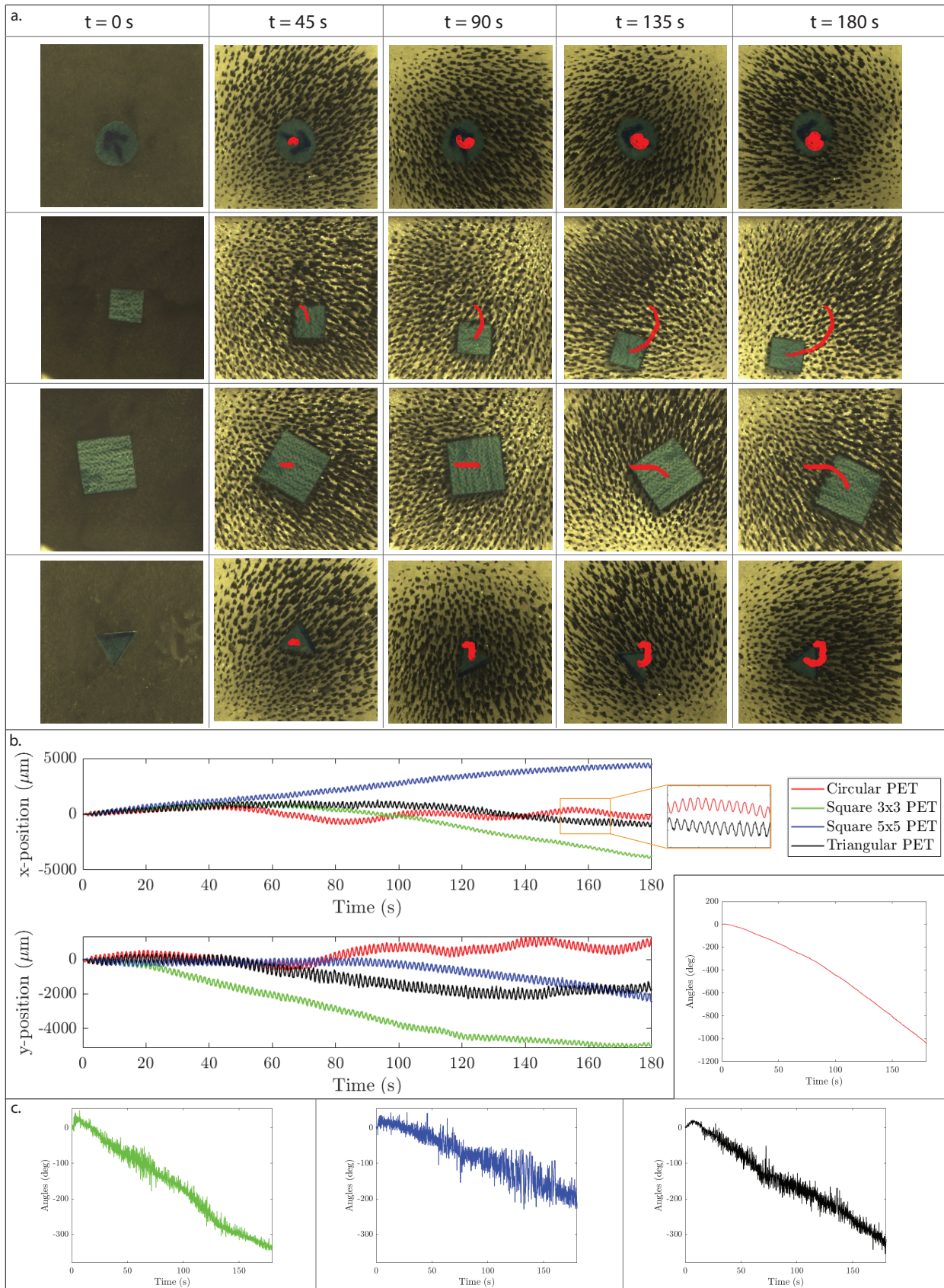


Figure 4.13: (a) Displacements and angles of the squared planar objects (3 mm dimension and 5 mm dimension), circular planar object (diameter of 3 mm) and triangular planar object (3.5 mm side length). (b) The graphs show that the planar objects are spiraling out from the middle of the workspace. The squared planar objects are spiraling out faster compared to the circular and triangular planar objects. (c) In addition, the objects are rotating around its own axis with approximately 0.03 rad/s for the 3 mm dimension square, approximately 0.02 rad/s for the 5 mm dimension square, approximately 0.12 rad/s for the circle and approximately 0.03 rad/sec for the triangle.

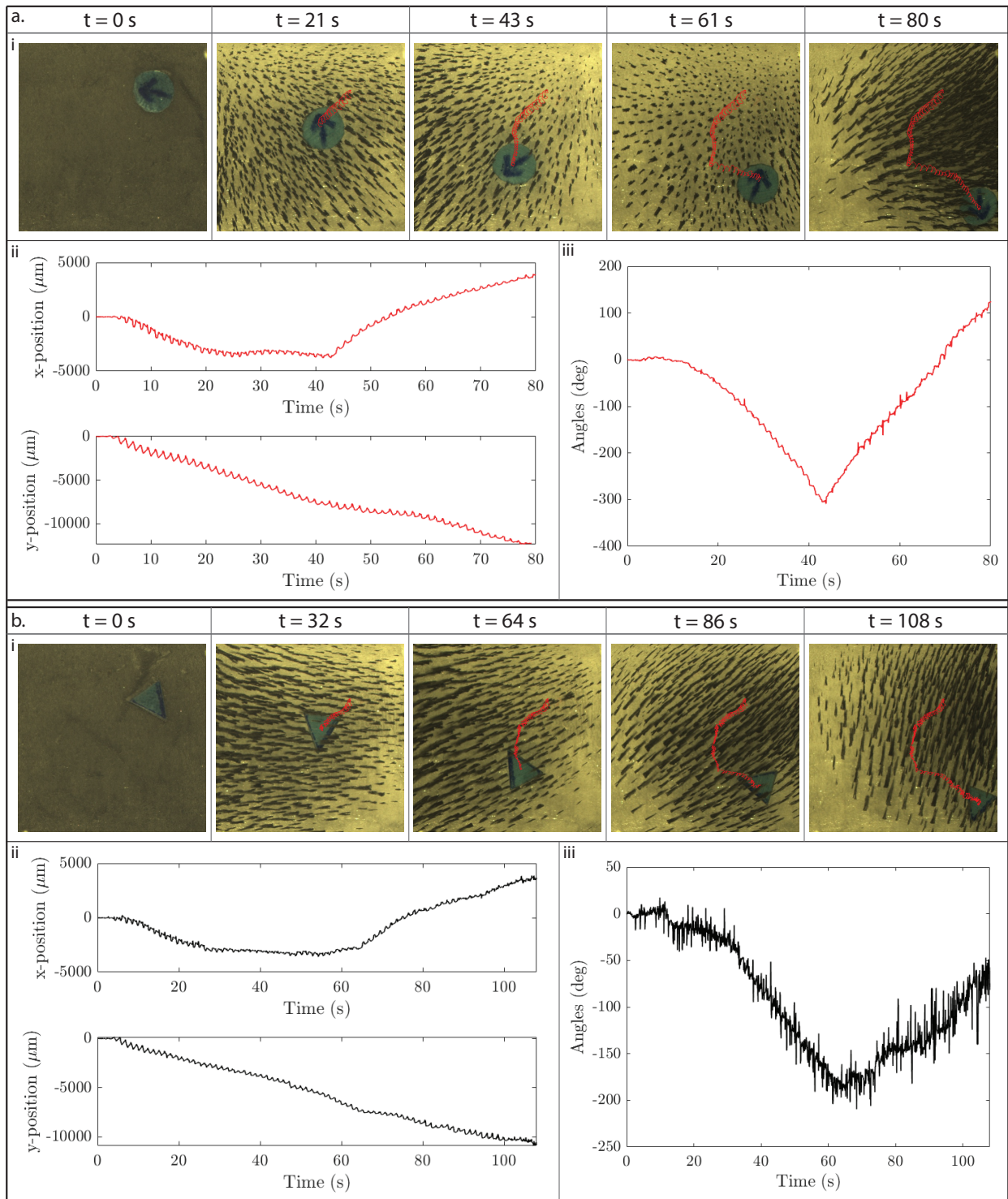


Figure 4.14: Displacement of the (a) circular and (b) triangular planar objects into two dimensions with graphs of the displacement in x - and y -direction and the angles of the rotation around its own axis.

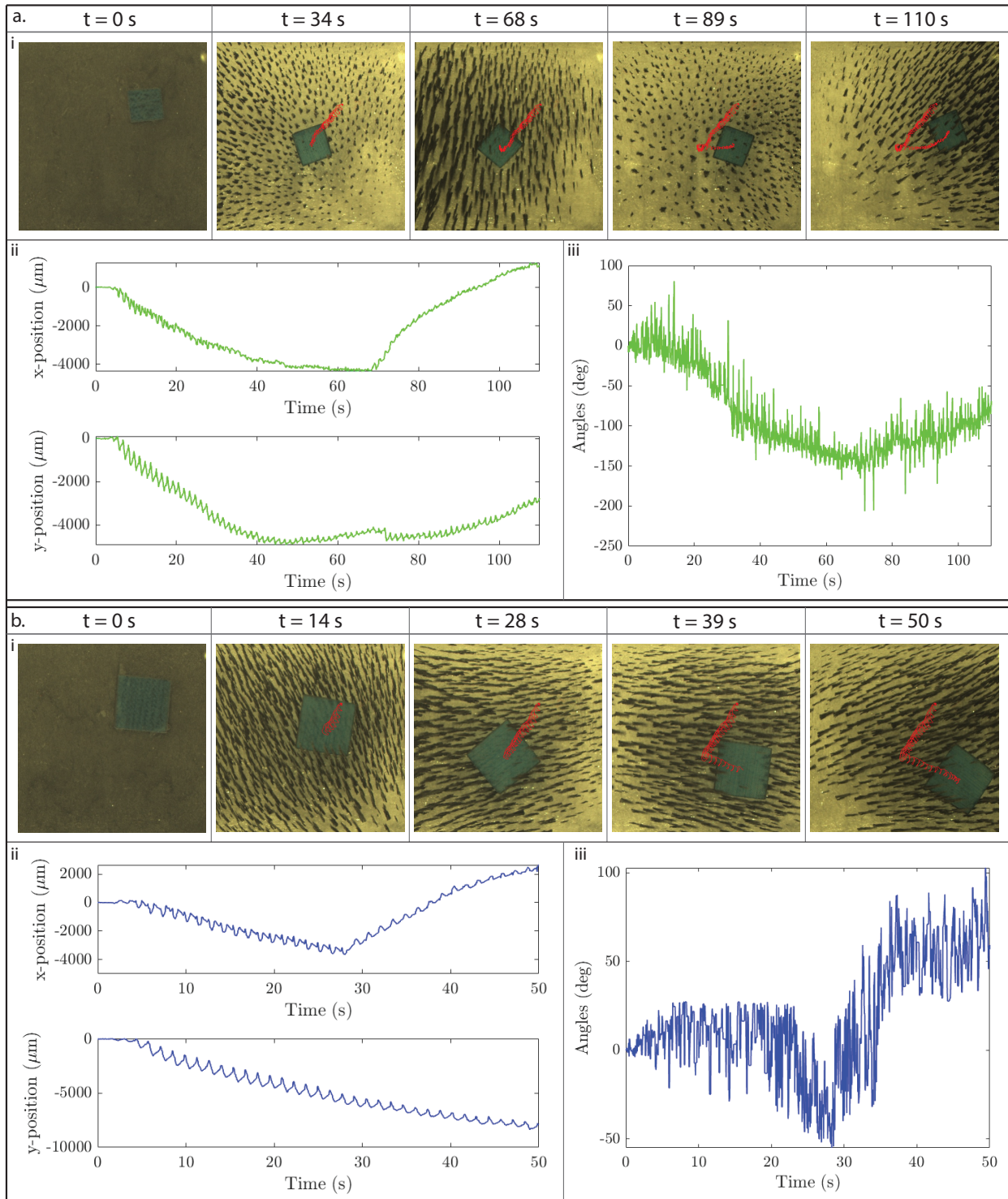


Figure 4.15: Displacement of the (a) 3 mm and (b) 5 mm dimension squared planar objects into two dimensions with graphs of the displacement in x- and y-direction and the angles of the rotation around its own axis.

The orientation of the magnetic field is changed at approximately 28 seconds for the 5mm squared planar object. After activating the magnetic field it takes the squared object approximately 2 seconds to start moving and approximately 12 seconds to start rotating around its own axis. Within 28 seconds an angle of -51° is reached. Between 28 seconds and 50 seconds an angle of approximately 122° is reached. The squared object rotates with an average speed of 0.05 rad/s around its own axis and moves with an average speed of $267.07 \mu\text{m/s}$.

For all planar objects, the planar objects rotate around their own axis in a clockwise direction when using the left-sweeping magnetic field. Then the objects rotate around their own axis in an anti-clockwise direction when using the right-sweeping magnetic field. As mentioned before, the pillars rotate around their own axis during the sweep. For the left-sweeping magnetic field, the pillars rotate anti-clockwise resulting the planar object to rotate clockwise around its own axis. For the right-sweeping magnetic field, the pillars rotate clockwise resulting the planar object to rotate anti-clockwise around its own axis.

4.3.3 Reconfiguration and relocation of the carpet

One of the main capabilities of using magnetic microparticles for generating the carpet without silicone is that the carpet is able to move through the workspace. To demonstrate this, the squared planar objects are placed in the middle of the workspace and all reduced iron microparticles are gathered in one of the corners of the workspace (Figure 4.16). Using the one-sided oscillating magnetic field the pillars move towards the object and push it forward. The pillars are able to displace the 3 mm squared object approximately $502 \mu\text{m}$ in x-direction and approximately $-539 \mu\text{m}$ in y-direction over a time of 20 seconds. This is also the time that it takes to cover the 3 mm squared object completely with the pillars. For the 5 mm squared object the displacement is approximately $-3706 \mu\text{m}$ in x-direction and approximately $3621 \mu\text{m}$ in y-direction over a time of 40 seconds which is again also the time it takes to cover the 5 mm squared object completely. The displacement of the 5 mm squared object is greater than the displacement of the 3 mm squared object which is due to the dimension of the object. The one-sided oscillating magnetic field displaces objects by pushing the object forward. Especially since no microparticles are placed underneath the planar object. Since the size of the object is bigger, more pillars are able to push the object forward, resulting in a greater displacement over time.

When the objects are covered fully by the pillars, the sweeping field is activated to try to move the object. The sweeping magnetic field displaces the 3 mm squared object approximately $3008 \mu\text{m}$ in x-direction and approximately $-212 \mu\text{m}$ in y-direction over a time of 84 seconds. For the 5 mm squared object, the sweeping magnetic field displaces the object approximately $-794 \mu\text{m}$ in x-direction and approximately $480 \mu\text{m}$ in y-direction over a time of 112 seconds. In this second part the 3 mm squared object has a greater displacement than the 5 mm squared object due to the motions of the carpet pillars. Since no pillars are underneath the planar object, the planar object only exhibits motion when the pillar is pushing the planar object. In experiments, we observe

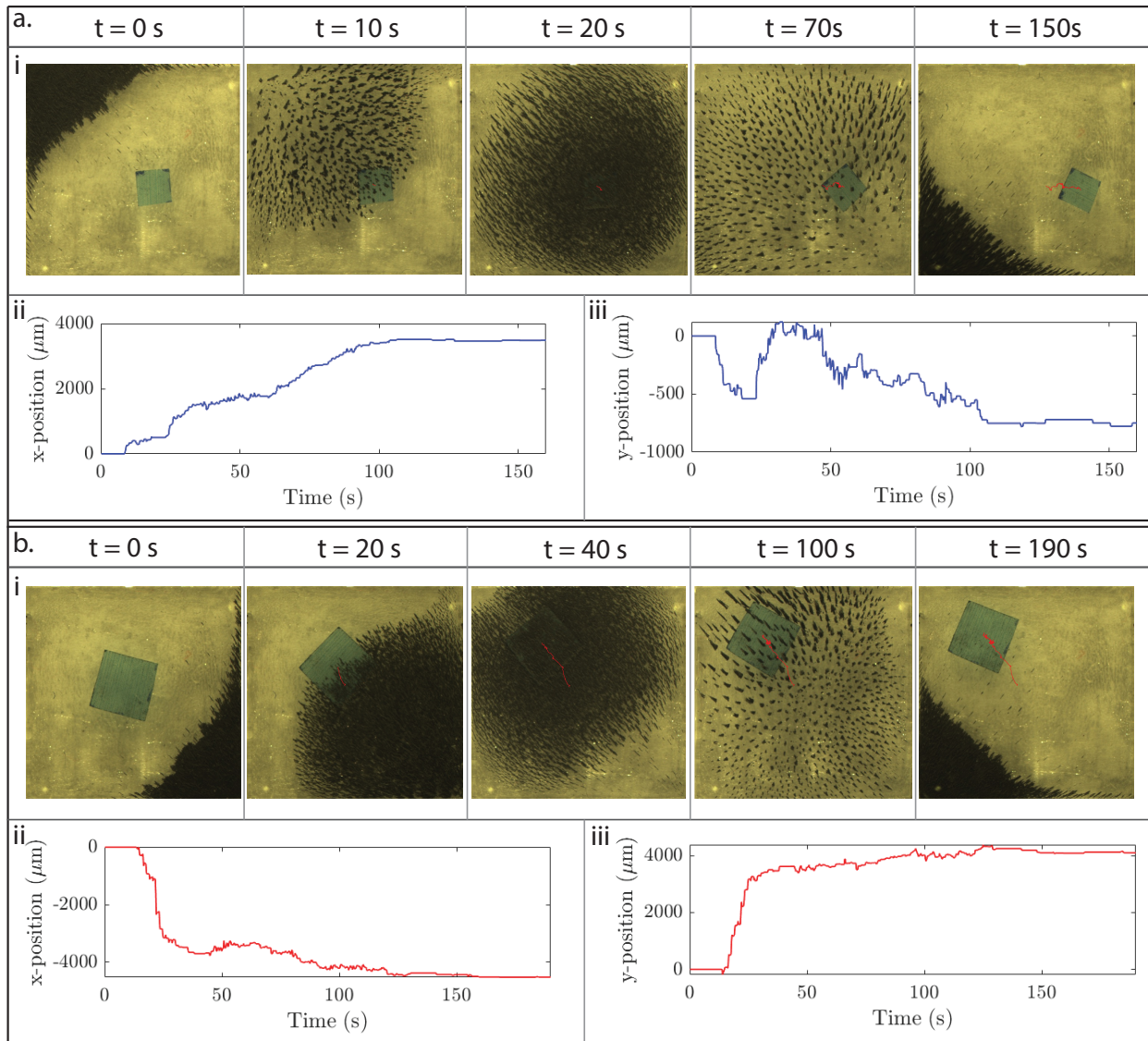


Figure 4.16: (a) The 3 mm dimension and 5 mm dimension squared are used in this experiment. For the 3 mm squared object, it takes 20 seconds to cover the planar object using the one-sided oscillating magnetic field. Then with the sweeping magnetic field the pillars try to displace the planar object. The sweeping magnetic field is resulting in a greater displacement of the 3 mm square compared to the displacement caused by the one-sided oscillating magnetic field. (b) For the 5 mm squared object, it takes 40 seconds to cover the planar object using the one-sided oscillating magnetic field. Using the sweeping magnetic field, the pillars try to displace the planar object. The one-sided oscillating magnetic field is resulting in a greater displacement of the 5 mm square compared to the displacement caused by the sweeping magnetic field.

that not all pillars at the sides of the planar objects are in contact with the planar objects which causes the planar object hardly move. In the last part of the experiment, the one-sided oscillating magnetic field is activated again to gather the pillars at a different corner and leave the object at its final location.

Conclusions and future work

In this master's thesis we propose a fabrication-free magnetic carpet for cargo transport of planar objects with different sizes, shapes and weights. This method of generating the magnetic carpet allows for easy configuration and relocation of the carpet within the workspace. In addition, the carpet can displace planar objects, with a weight upto 9.55 mg, within the workspace by transporting them on the tips of the pillars. We tested different actuation mechanisms to investigate which one is suitable for cargo transport, concluding that the sweeping magnetic field is the most efficient actuation mechanism for object transportation. We demonstrated that the planar object (with different shapes) can move into two dimensions. Furthermore, the one-sided oscillating magnetic field is an efficient actuation mechanism as well. However, this actuation mechanism is only efficient as long the carpet is not fully moved over the planar object. When using the one-sided oscillating magnetic field in combination with the sweeping magnetic field, the carpet can to move towards a planar object, perform transportation of the planar object using pushing forces and then relocate the carpet to a different location.

One of the main challenges of cargo transport using the fabrication-free magnetic carpet, is to move the planar objects into desired directions. Future work includes to design a feedback controller using the position of the planar objects as input. Furthermore, we should perform a force test to find the weight limitations of the generated carpet. Finally, we should perform transportation using other objects like spherical beads of different sizes and weights and try to perform the transportation of multiple objects simultaneously.

Bibliography

- [1] Cilia and flagella. URL: <https://www.thoughtco.com/cilia-and-flagella-373359>.
- [2] An introduction to solenoids. URL: <https://circuitdigest.com/article/what-is-solenoid-its-working-principle-and-types>.
- [3] Vector calculus: Understanding circulation and curl. URL: <https://betterexplained.com/articles/vector-calculus-understanding-circulation-and-curl/>.
- [4] Vector calculus: Understanding divergence. URL: <https://betterexplained.com/articles/divergence/>.
- [5] Web site of the documentation of ros. URL: <http://wiki.ros.org/>.
- [6] Y. Alapan, U. Bozuyuk, P. Erkoc, A.C. Karacakol, and M. Sitti. Multifunctional surface micro-rollers for targeted cargo delivery in physiological blood flow. *Science Robotics*, 5(42), 2020. doi:10.1126/scirobotics.aba5726.
- [7] S. Ben, J. Tai, H. Ma, Y. Peng, Y. Zhang, D. Tian, K. Liu, and L. Jiang. Cilia-inspired flexible arrays for intelligent transport of viscoelastic microspheres. *Advanced Functional Materials*, 28(16), 2018. doi:10.1002/adfm.201706666.
- [8] K. Bente, A. Codutti, F. Bachmann, and D. Faivre. Biohybrid and bioinspired magnetic microswimmers. *Small*, 14(29), 2018. doi:10.1002/smll.201704374.
- [9] C. Calderon-Arce, J.C. Brenes-Torres, and R. Solis-Ortega. Swarm robotics: Simulators, platforms and applications review. *Computation*, 10(6):80, May 2022. doi:<https://doi.org/10.3390/computation10060080>.
- [10] A.R. Cheraghi, S. Shahzad, and K. Graffi. Past, present, and future of swarm robotics. In K. Arai, editor, *Intelligent Systems and Applications*, pages 190–233. Springer International Publishing, 2022.
- [11] J. Choi, J. Hwang, J.-Y. Kim, and H. Choi. Recent progress in magnetically actuated microrobots for targeted delivery of therapeutic agents. *Advanced Healthcare Materials*, 10(6), 2021. doi:10.1002/adhm.202001596.
- [12] Z. Cui, S. Zhang, Y. Wang, L. Tormey, O.S. Kanies, R.C. Spero, J.K. Fisher, and J.M.J. den Toonder. Self-cleaning surfaces realized by biologically sized magnetic artificial cilia. *Advanced Materials Interfaces*, 9(5), 2021. doi:10.1002/admi.202102016.

- [13] A.F. Demirörs, S. Aykut, S. Ganzeboom, Y. Meier, R. Hardeman, J. de Graaf, A.J.T.M. Mathijssen, E. Poloni, J.A. Carpenter, C. Ünlü, and D. Zenhäusern. Amphibious transport of fluids and solids by soft magnetic carpets. *Advanced Science*, 8(21), November 2021. doi:10.1002/advs.202102510.
- [14] D. C. Giancoli. *Physics for scientists & engineers with modern physics*. Harlow, Essex: Pearson Education Limited, 4th edition, pearson new international edition, 2014.
- [15] I. Giardina. Collective behavior in animal groups: theoretical models and empirical studies. *HFSP J.*, 2(4), August 2008. doi:10.2976/1.2961038.
- [16] D. J. Griffiths. *Introduction to Electrodynamics*. Harlow, Essex: Pearson Education Limited, 4th edition, pearson new international edition, 2014.
- [17] A. R. Hambley. *Electrical Engineering - Principles and Applications*. Harlow, Essex: Pearson Education Limited, 6th edition, pearson new international edition, 2014.
- [18] S.-H. Lee, J. Kim, M. Seong, S. Kim, H. Jang, H.W. Park, and H.E. Jeong. Magneto-responsive photothermal composite cilia for active anti-icing and de-icing. *Composites Science and Technology*, 217, 2022. doi:10.1016/j.compscitech.2021.109086.
- [19] L. Yang, J. Miao, G. Li, H. Ren, T. Zhang, D. Guo, Y. Tang, W. Shang, and Y. Shen. Soft tunable gelatin robot with insect-like claw for grasping, transportation, and delivery. *ACS Applied Polymer Materials*, 4(8):5431–5440, 2022. doi:10.1021/acsapm.2c00522.
- [20] M.H.A. Majid, M.R. Arshad, and R.M. Mokhtar. Swarm robotics behaviors and tasks: A technical review. In M. Mariappan, M.R. Arshad, R. Akmeliawati, and C.S. Chong, editors, *Control Engineering in Robotics and Industrial Automation: Malaysian Society for Automatic Control Engineers (MACE) Technical Series 2018*, pages 99–167. Springer International Publishing, 2022. doi:10.1007/978-3-030-74540-0_5.
- [21] J. Miao, S. Sun, T. Zhang, G. Li, H. Ren, and Y. Shen. Natural cilia and pine needles combinedly inspired asymmetric pillar actuators for all-space liquid transport and self-regulated robotic locomotion. *ACS Applied Materials & Interfaces*, 14(44):50296–50307, October 2022. doi:10.1021/acsami.2c12434.
- [22] J. Miao, T. Zhang, G. Li, W. Shang, and Y. Shen. Magnetic artificial cilia carpets for transport, mixing, and directional diffusion. *Advanced Engineering Materials*, 24(7), November 2021. doi:10.1002/adem.202101399.
- [23] K. Ni and Z. Wang. Recent progress on the development of magnetically-responsive micropillars: Actuation, fabrication, and applications. *Advanced Functional Materials*, 33(14), 2023. doi:10.1002/adfm.202213350.
- [24] The Editors of Encyclopaedia Britannica. Magnetic dipole. URL: <https://www.britannica.com/science/magnetic-dipole>.

- [25] F. Ongaro, S. Pane, S. Scheggi, and S. Misra. Design of an electromagnetic setup for independent three-dimensional control of pairs of identical and nonidentical microrobots. *IEEE transactions on robotics*, 35(1):174–183, February 2019. doi:10.1109/TR0.2018.2875393.
- [26] J. Park, C. Jin, S. Lee, J.-Y. Kim, and H. Choi. Magnetically actuated degradable microrobots for actively controlled drug release and hyperthermia therapy. *Advanced Healthcare Materials*, 8(16), 2019. doi:10.1002/adhm.201900213.
- [27] D. Sun S. Zhao, J. Zhang, H. Lu, Y. Wang, R. Xiong, and K.T.V. Grattan. Actuation and biomedical development of micro-/nanorobots - a review. *Materials Today Nano*, 18:100223, May 2022. doi:10.1016/j.mtnano.2022.100223.
- [28] V. Sahadevan, B. Panigrahi, and C.-Y. Chen. Microfluidic applications of artificial cilia: Recent progress, demonstration, and future perspectives. *Micromachines*, 13:735, May 2022. doi:10.3390/mi13050735.
- [29] Science4Fun. Magnetism. URL: <https://science4fun.info/magnetism/>.
- [30] N.J. Shetty, P. Swati, and K. David. Nanorobots:future in dentistry. *Epub*, 25(2), 2013. doi:10.1016/j.sdentj.2012.12.002.
- [31] J.V.I. Timonen, C. Johans, K. Kontturi, A. Walther, O. Ikkala, and R.H.A. Ras. A facile template-free approach to magnetodriven, multifunctional artificial cilia. *ACS Applied Materials & Interfaces*, 2(8), 2010. doi:10.1021/am100244x.
- [32] S. Tottori, L. Zhang, F. Qiu, K.K. Krawczyk, A. Franco-Obregón, and B.J. Nelson. Magnetic helical micromachines: Fabrication, controlled swimming, and cargo transport. *Advanced Materials*, 24(6):811–816, January 2012. doi:10.1002/adma.201103818.
- [33] T. ul Islam, Y. Wang, I. Aggarwal, Z. Cui, H.E. Amirabadi, H. Garg, R. Kooi, B.B. Benkataramanachar, T. Wang, S. Zhang, P.R. Onck, and J.M.J. den Toonder. Microscopic artificial cilia - a review. *Lab Chip*, 22:1650–1679, April 2022. doi:10.1039/d11c01168e.
- [34] J. Wang and A. Chortos. Control strategies for soft robot systems. *Advanced Intelligent Systems*, 4(5), February 2022. doi:<https://doi.org/10.1002/aisy.202100165>.
- [35] Z. Wang, Z. Xu, B. Zhu, Y. Zhang, J. Lin, Y. Wu, and D. Wu. Design, fabrication and application of magnetically actuated micro/nanorobots: a review. *Nanotechnology*, 33(15), January 2022. doi:10.1088/1361-6528/ac43e6.
- [36] H. Xie, M. Sun, X. Fan, Z. Lin, W. Chen, L. Wang, L. Dong, and Q. He. Reconfigurable magnetic microrobot swarm: Multimode transformation, locomotion, and manipulation. *Science Robotics*, 4(28):eaav8006, 2019. doi:10.1126/scirobotics.aav8006.
- [37] Z. Xu and Q. Xu. Collective behaviors of magnetic microparticle swarms: From dexterous tentacles to reconfigurable carpets. *ACS Nano*, 16(9):13728–13739, August 2022. doi:10.1021/acsnano.2c05244.

- [38] L. Yang, J. Yu, S. Yang, B. Wang, B.J. Nelson, and L. Zhang. A survey on swarm micro-robotics. *IEEE Transactions on Robotics*, 38(3):1531–1551, 2022. doi:10.1109/TR0.2021.3111788.
- [39] H. Zhou, C.C. Mayorga-Martinez, S. Pané, L. Zhang, and M. Pumera. Magnetically driven micro and nanorobots. *Chemical Reviews*, 121(8):4999–5041, 2021. doi:10.1021/acs.chemrev.0c01234.

Background

A.1 Magnetism

Magnetism is the force that magnets use to either attract or repel one another. The concept of magnetism goes back thousands of years [14]. It was discovered that some rocks in the Magnesian area of Asia Minor could attract each other and called these magnets. In the nineteenth century, it was discovered that magnetism and electric currents were related. It was found that magnetic fields were produced by electric currents.

Magnets have two poles, defined as both ends of the magnet. At these poles, the magnetic effect is the strongest. One of these poles will point to the geographic north if you hang a magnet bar onto a thin wire. The Chinese used this principle to create a compass for navigation purposes in the eleventh century [14]. The magnetic bar has a north pole that points to the geographic north pole and a south pole that points towards the south. Attractive or repulsive forces can be exerted on magnets depending on the relative position of their poles. For instance, when two north poles or two south poles are brought near each other a repulsive force appears and when a south pole and north pole are brought near each other an attractive force appears. Such magnet is also called a permanent magnet since it generates a persistent magnetic field that does not change. Two new permanent magnets are formed with a north and south pole when cutting the permanent magnet in half. Each magnet has a magnetic field that can be visualized by drawing the magnetic field lines (also called lines of magnetic flux [17], illustrated in Figure A.1). The strength of the magnetic field is related to the number of magnetic field lines, and the magnetic field's direction is perpendicular to a field line at any point [14].

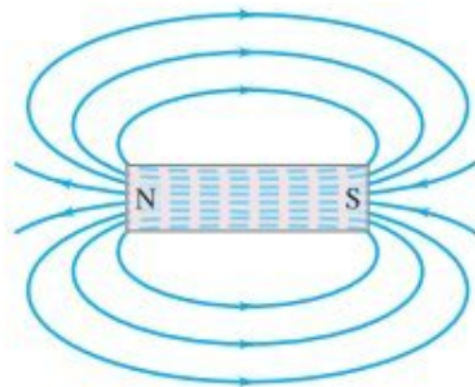


Figure A.1: Visualisation of the magnetic field lines of a magnet. (Adapted from Giancoli et al. [14])

Besides permanent magnets, magnetic fields also exist around wires that carry current, as shown in Figure A.2. Hans Christian found in 1820 that when a wire has current, and a compass is brought near the wire, then the generated magnetic field deflects the needle of the compass [14]. Hereby, Hans Christian showed that a wire that carries current generates a magnetic field. Unlike permanent magnets, the south and north pole of a wire carrying a current is not defined as fixed to the sides of the wire but depends on the direction of the current through the wire. For example, if two wires carry current where the currents have opposite directions, the wires will repel each other. When the current in both wires have the same directions, the wires will attract. The electrical charge in motion is the fundamental source of the magnetic field in a wire that carries current (which also applies to the permanent magnet where the spin of electrons in atoms creates the magnetic field) [17]. A force appears when a wire that carries current is placed inside a magnetic field, which is shown in Figure A.2. The direction of this force is always perpendicular to the direction of the positive current ($I \in \mathbb{R}$) and the direction of the magnetic field ($\mathbf{B} \in \mathbb{R}^3$), where the current can be described as the charge per unit time that is passing a certain point [16]. The strength of the magnetic field is described in Tesla (T) where $1T = 1N/(A \cdot m)$. The magnetic force on a charge can then be described by Equation A.1 where $\mathbf{F} \in \mathbb{R}^3$ is the magnetic force, $q \in \mathbb{R}$ is the moving charge, $\mathbf{v} \in \mathbb{R}^3$ is the velocity vector at which the charge is moving through the magnetic field.

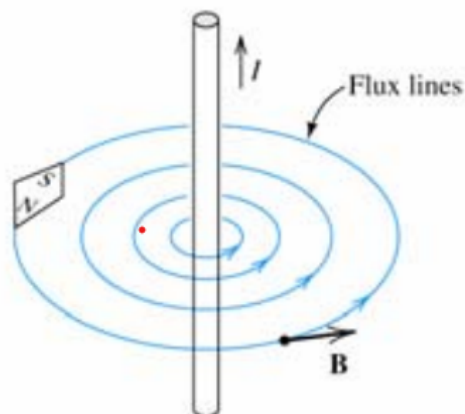


Figure A.2: A current-carrying wire generates a circular magnetic field that is strongest close to the wire and gets weaker when you move away from the wire. (Adapted from Hambley [17])

$$\mathbf{F} = q \mathbf{v} \times \mathbf{B} \quad (\text{A.1})$$

Since the force is always perpendicular to the direction of the velocity and magnetic field, the magnetic force is only capable of changing the direction of the movement but is not able to modify the velocity of the charge. Knowing this, the force on a current-carrying wire with a certain length can then be described by Equation A.2 where $I \in \mathbb{R}$ is the current that is carried by the wire and $l \in \mathbb{R}$ is the length of the wire. Then the magnetic force of a finite length of the wire, between points $a \in \mathbb{R}$ and $b \in \mathbb{R}$, can be described with Equation A.3.

$$d\mathbf{F} = i d\mathbf{l} \times \mathbf{B} \quad (\text{A.2})$$

$$\mathbf{F} = i \int_a^b d\mathbf{l} \times \mathbf{B} \quad (\text{A.3})$$

Magnetic fields work according to the superposition principle which implies that when you have multiple coils that generate their own magnetic fields that overlap then the resulting magnetic field is the sum of these separate magnetic fields. To determine the direction of the magnetic field that is generated by a current-carrying wire, the right-hand rule can be used [17]. Two interpretations of

this rule will be discussed next. The first interpretation is when we want to determine the direction of the magnetic field of a current-carrying wire. In this case if your thumb points into the direction of the current, the four fingers point into the direction of the magnetic field around the wire. The second interpretation is for a coil where we point our fingers into the direction of the current, then the thumb is pointing into the direction of the magnetic field. These two interpretations of the right-hand rule are illustrated in Figure A.3.

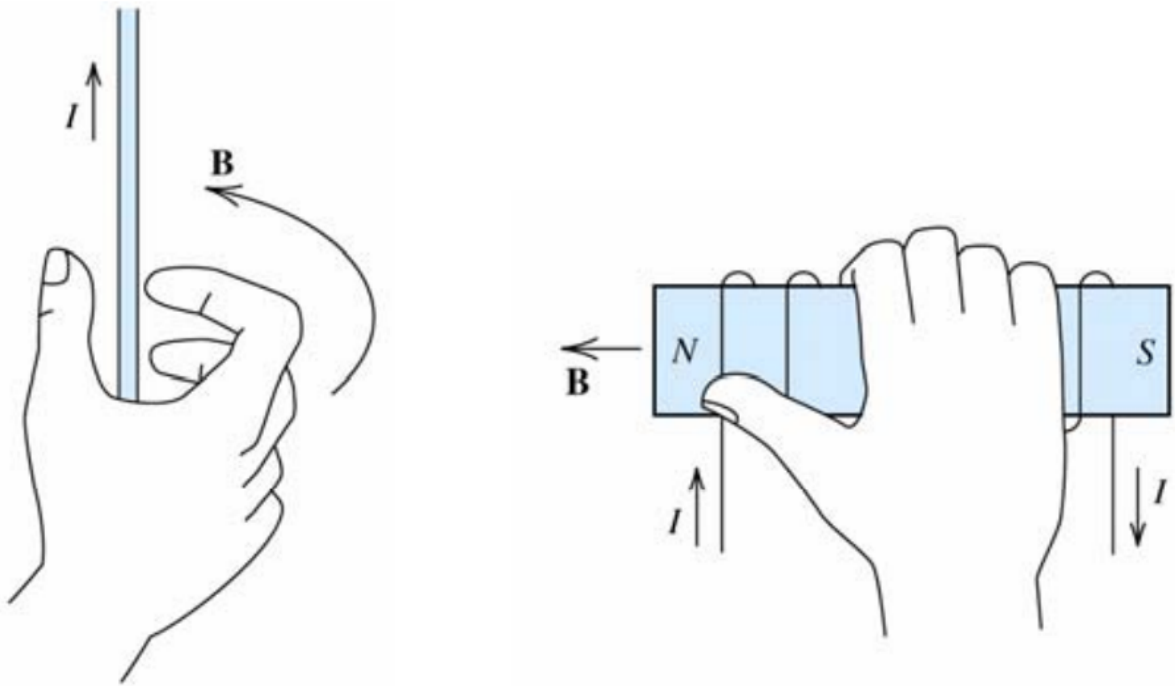


Figure A.3: The Right-Hand rule. In left figure on the right-hand rule is illustrated for a wire that is carrying current where the thumb is pointed into the direction of the flowing current and the four fingers are pointing into the direction of the magnetic field. In the right figure the right-hand rule is illustrated for a coil where the fingers point into the direction of the flowing current and the thumb is pointing into the direction of the magnetic field. (Adapted from Hambley [17])

A static magnetic field is created when a static current is carried through the wire. The higher this current, the stronger the generated magnetic field and the lower the current, the weaker the generated magnetic field. Using the Biot-Savart law it is possible to calculate the magnetic field at a certain point p in space of a static magnetic field produced by a current. Equation A.4 describes the Biot-Savart law where $\mu_0 = 4\pi \times 10^{-7} \text{N/A}^2$ which describes the permeability of free space and $r \in \mathbb{R}^3$ which is the vector from the source to point p .

$$\mathbf{B}(p) = \frac{\mu_0}{4\pi} \mathbf{I} \int \left(\frac{d\mathbf{l} \times \hat{\mathbf{r}}}{r^2} \right) \quad (\text{A.4})$$

A.1.1 Maxwell's Equations

A current-carrying wire as shown in Figure A.2 that generates a circular magnetic field ($\mathbf{B} = [\mathbf{B}_x \ \mathbf{B}_y \ \mathbf{B}_z]^T$), which is strongest close to the wire and gets weaker when you move away from the wire (the magnitudes of the vector field decreases when moved further away from the wire) [16].

In this 2D example, any point p taken in this space has a divergence of zero which is shown in Equation A.6. Divergence relates to the flux density which is the total flux through a unit area [4]. The divergence can be positive or negative depending on whether more flux is entering than leaving at point p (called a sink) or more flux is leaving than entering point p (called a source) respectively. The total flux can be calculated by adding the field changes in direction x , y and z . Then the divergence can be mathematically shown as Equation A.5 where ∇ is the gradient operator.

$$\text{Divergence} = \frac{\partial \mathbf{B}_x}{\partial x} + \frac{\partial \mathbf{B}_y}{\partial y} + \frac{\partial \mathbf{B}_z}{\partial z} \quad (\text{A.5})$$

$$= \nabla \cdot \mathbf{B} = 0 \quad (\text{A.6})$$

Besides the divergence of a magnetic field, there is also the curl of the magnetic field. The rate of rotation at points inside the magnetic field can be described by the curl which is a vector with a magnitude and direction [3]. The magnitude indicates the rate of rotating force at that point. The direction of the curl gives the orientation where the maximal rotation can be gained. This direction can be found by the right-hand rule where the fingers point into the direction of the rotating force and the thumb is then pointing into the direction of the curl. Mathematically, the curl can be described in Equation A.7.

$$\text{Curl}(\mathbf{B}) = \nabla \times \mathbf{B} \quad (\text{A.7})$$

$$= \mu_0 \mathbf{J} + \mu_0 \epsilon_0 \frac{\partial \mathbf{E}}{\partial t} \quad (\text{A.8})$$

Then we can use Ampère's law for static fields to express Equation A.7 in electric field and current density which is described in Equation A.8 where $\mathbf{E} \in \mathbb{R}^3$ is the electric field and $\mathbf{J} \in \mathbb{R}^3$ is the current density. A part of the last term can be described by \mathbf{J}_d which is the displacement current as shown in Equation A.9.

$$\mathbf{J}_d = \epsilon_0 \frac{\partial \mathbf{E}}{\partial t} \quad (\text{A.9})$$

Taking Equation A.9 and Equation A.8 into mind, it is possible to conclude that when the electric field is non-zero, then the magnetic field is also non-zero. Therefore, A magnetic field is produced by an altering electric field.

The Maxwell's equations are four equations that define the behavior of magnetic and electric fields [16]. Two of these equations are used to describe the magnetic field and the relation of the electric field to the magnetic field. The Maxwell's equations are defined using the divergence and curl properties of the magnetic fields as described in this subsection. The Maxwell's equations are shown again in Equation A.10 and Equation A.11.

$$\nabla \cdot \mathbf{B} = 0 \quad (\text{A.10})$$

$$\nabla \times \mathbf{B} = \mu_0 \mathbf{J} + \mu_0 \epsilon_0 \frac{\partial \mathbf{E}}{\partial t} \quad (\text{A.11})$$

A.1.2 Electromagnetic field and magnetic materials

Multiple loops of current-carrying wire is called a solenoid as shown in Figure A.4. The closer the turns of wire are, the closer the magnetic field is to an uniform field where the field is strongest at the ends of the solenoid [14]. An uniform field is a magnetic field where the flux lines are parallel to each other with the same distances between the lines while a non-uniform field is a field where the lines differ in direction and distances between the lines. The closer the field lines, the stronger the field that is produced by the solenoid. The center of the solenoid is near an uniform field but becomes more non-uniform when moved further away from the outside of the solenoid. A solenoid behaves like a permanent magnet but is different in that the location of the north pole and south pole depend on the direction of the current. Therefore the north and south pole can be reversed by reversing the direction of the current.

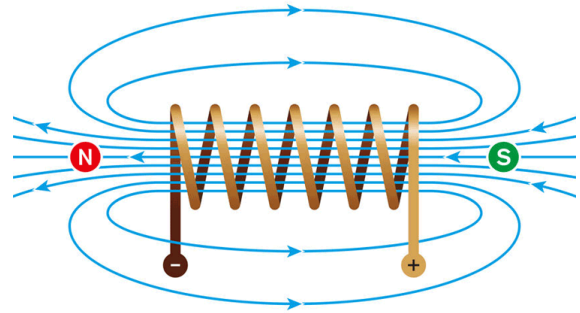


Figure A.4: Visualisation of the magnetic field of a solenoid. (This figure is retrieved from Circuit Digest [2].)

An electromagnet exists of a solenoid with a core of iron [14]. In this case the current-carrying wire is twisted around the piece of iron which is able to generate a strong magnetic field. Needless to say, the strength of the magnetic field generated by the electromagnet depends on the current. When multiple electromagnets are placed together and the current on each electromagnet is changing over time it is possible to generate different types of magnetic fields including oscillating magnetic fields and rotating magnetic fields.

Magnetic fields are generated by moving charges or current-carrying wires where for permanent magnets the spin of electrons around atoms creates the magnetic field [24]. The magnetic field is created because the electrons are carrying charge. This direction in which the electron moves around the atom decides whether it is a north pole or south pole. If the number of electrons are even, the magnetic fields will cancel each other out. However, there exists also atoms with an uneven amount of electrons which means that it has a net magnetic field. In other words, the atom is then a magnetic dipole and has a magnetic dipole moment. When materials with magnetic dipoles are exposed to a magnetic field, the magnetic dipoles will align and the material becomes magnetized.

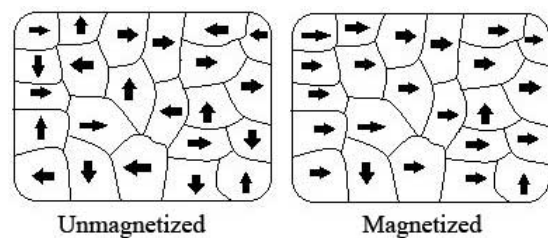


Figure A.5: Visualisation of the domains inside a piece of ferromagnetic material where the domains are randomly ordered when unmagnetized and aligned when magnetized. (Adapted from Science4Fun [29].)

Materials that can become strong magnets like iron are called ferromagnetic materials [14].

Such a piece of iron is divided in so called domains. Each domain has a north and south pole and behaves like a small magnet. The domains are organized in a random order (where they cancel each other out) when the iron is not magnetized. The iron becomes magnetized by placing the piece of iron inside a strong magnetic field. The direction of the domains will become more aligned and the piece of iron becomes a magnet. This process is shown in Figure A.5. Therefore, the magnetic field produced by an electromagnet increases significantly due to the iron core since the domains of the iron are now aligned with the flux lines of the solenoid.

The hysteresis curve shows the behaviour of a ferromagnetic material when placed inside a magnetic field (illustrated in Figure A.6). The domains of the material become more and more aligned until a saturation point is reached (from point a to b in Figure A.6). When the ferromagnetic material is magnetized, the domains do not fully become random when the magnetic field is deactivated which means that some magnetism remains (like point d and g in Figure A.6). Now the ferromagnetic material will act according to the hysteresis loop (points b, d, c, f and g in Figure A.6). When a ferromagnetic material has a broad hysteresis graph, the material makes a good permanent magnet since the ferromagnetic material stays more magnetized when the magnetic field is deactivated. For ferromagnetic materials with a thin hysteresis curve, the material becomes less magnetized when the magnetic field is deactivated. Therefore, these ferromagnetic materials are used as core for electromagnets.

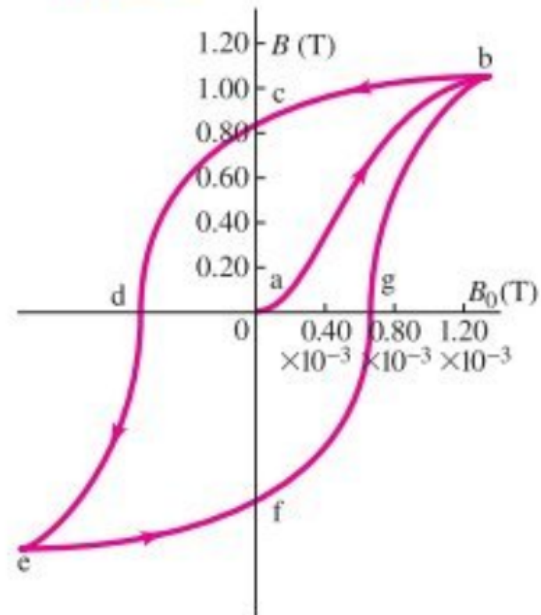


Figure A.6: Hysteresis curve of iron. (Adapted from [14].)

A.2 Swarm robotics

In 1988 the term "swarms" is first used by G. Beni and Fukuda in the robotics context [10]. Later they introduced the term swarm intelligence to describe a set of agents that can collaborate just like the cells of the human body. They claimed that the agents showed intelligent behaviour. In 1993 Gregory Dudek *et al.* says that swarms should be divided by its features. There are multiple definitions on what swarms are but we will conduct the definition as defined in the paper of Cheraghi *et al.* [10]. They define swarms as a large group of individuals that have to work together to accomplish tasks. However, there are still a lot of different types of swarms like biological swarms which are swarms found in nature (e.g. ants that perform a complicated task together like building a bridge to move over a gap). In this context swarms are defined as robotic swarms which behaviour is based on the behaviour of biological swarms.

A.2.1 High-Level and Low-Level tasks in swarm robotics

G. Beni introduces three swarm properties to increase the efficiency of the swarm robotics during the execution of a certain task. These properties are flexibility, scalability and robustness [10]. This means that the swarm must be able to perform various tasks where the individuals of the swarm can have multiple roles, the swarm must be able to accomplish tasks where the swarm varies in size and the swarm must be able to perform tasks while the environment might get disturbed (for example some individuals of the swarm are lost during performing the task). These three features are directly three advantages of swarm robotics. There are other advantages as well: the swarm of agents can combine their abilities for tasks, the swarm of agents are able to work in parallel which increases the speed of the completion of multiple tasks and the swarm of agents have a simple design which gives low cost. However, there are also a few drawbacks on swarm robotics. The biggest drawback is the realisation of the swarm robotics systems in applications in the real world.

The behaviour of swarm robotics can be defined into three groups: group behaviour, pair behaviour and individual behaviour [20]. Normally, we are mostly interested in the group behaviour of the swarm robotics which is the result of the interaction between the agents. The tasks that are performed by swarm of agents can be divided into two groups: low-level tasks and high-level tasks. The low-level tasks include:

- Aggregation. The gathering of agents at a location so the agents can interact.
- Dispersion. The process of distributing the agents over a certain area while they still interact with each other.
- Self-assembly and self-reconfigurable. The behaviour where the agents form a desired structure and can change into different types of structures.
- Pattern formation and flocking. Pattern formation is the process of forming a desired pattern and maintaining this pattern when the distance between agents, location or orientation changes. Flocking is focused on relocating the swarm of agents in a certain environment where maintaining the pattern is not a priority.
- Robot-environment interaction. The behaviour of the swarm of agents where they adapt and respond to changes in the environment.
- Task allocation. This is the process of dividing the tasks over the agents and control the group size of the agents.
- Robot learning. The approach where the agents are able to gain skills using learning algorithms.
- Collective tracking. The process where a the swarm of agents if following an object through the environment.

These low-level tasks are needed to accomplish the high-level tasks [20]. The most common high-level tasks are listed below. Note that for some of these tasks the swarm of agents have some sorts of sensors so data can be collected and analyzed.

- Collective searching and localization. The process of detecting and localizing a certain target or source where a target could be a physical object and the source could be a sound.
- Collective mapping. This is a process of modeling the environment where the environment is not known and localize the current position inside the created map.
- Collective Foraging. The process of searching an object and bring this object back to a certain location.
- Collective Transport. The process of moving an object from one location to another location.
- Collective Manipulation. The process were agents work together to handle and modify the geometry of an object.

In practice, there are simulators for swarm algorithms where the swarm of agents exists of mathematical models where the swarm does not exists of physical agents [9]. Software examples these simulators are *TeamBots*, *Gazebo* and *Swarm-bots*. It is also possible to use these kinds of simulations to test and evaluate the behaviour of the agents before testing it in a real-life application. The last decade, multiple promising real-life swarm agents are developed which are currently well-known and have been popular for researchers in the swarm robotics field. Examples of these agents are *E-puck*, *Khepera* and *Kilobot* which are on macroscale. These agents exists of a combination of sensors and communication protocols which therefore can easily be used for one of high-level tasks discussed in the previous paragraph. There are also swarms on micro- or nanoscale. There exist a few different shapes of the agents which might need a fabrication process to create these shapes. A few examples of existing types of agents are spherical, helical, flexible, wire-like, biohybrid, surface walkers and swarming agents. (More information on these types of agents can be found in the papers in the references [27] [39] [35] [8] [32].) Swarms of microrobots can be actuated with different methods e.g. based heat, fluid, electric fields and magnetic fields [34] [10]. In addition they are used in a wide range of biomedical applications (e.g. targeted drug delivery [11], cargo transport [37], in vivo detection [30], cell manipulations [39] and minimally invasive surgery (MIS) [39]) due to their small size, light weight and high precision [35].

BatMag system

The BatMag system is powered using two power sources. The power source (SM 70-20, Delta Elektronika, The Netherlands), located at the top of the setup, powers the coils and is set on 50V. The power source (BT-305, BASETech, The Netherlands), located on the right side of the setup, powers the LEDs, cooling system and the PCBs that control the amps that go through the coils and the settings of this power source are set on +/- 3A and +/- 25V. The cameras are directly connected to the desktop which runs the software. The software is based on a CMake system to build and run the code. The software, developed by Ongaro *et al.* [25], of BatMag consists of an GUI with multiple tabs. The software includes different programs which communicate to each other using the Robotic Operating System (ROS). Each program includes a different functionality of the BatMag system. These different programs are tracking, control, camera's, GUI, force to field mapping, CAN-bus communication and logging.

ROS is an operating system designed for a robotic system [5]. This software is an open source SDK for robotic environments. ROS has a lot of functionalities such as performing the communication between different sensors or parts inside the robotic system and tools for analyzing purposes and testing purposes. In this project, the ROS software is mainly used for communication purposes between the GUI and the different functionalities like the tracking and control algorithm.

Each program consists of a ROS node. These ROS nodes are started when the BatMag software is executed. ROS topics are used to communicate between the different ROS nodes. The communication protocol uses publishers and subscribers where a program can publish its data asynchronously on a created topic then another program can subscribe on this topic to receive that data. A graph of the ROS nodes and ROS topics of the software designed by Ongaro *et al.* [25] is given in Figure B.1.

Additions are made to the original BatMag system by Ongaro *et al.* [25]. The hardware and software designs are discussed in the next sections.

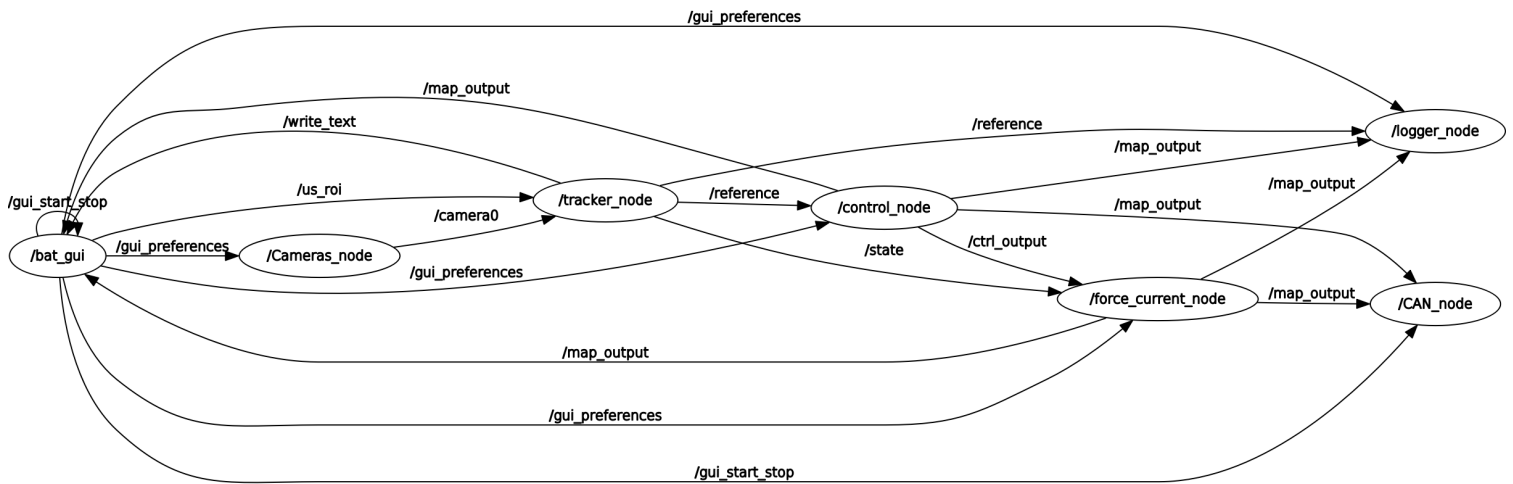


Figure B.1: Graph of ROS nodes and the ROS topics connecting the ROS nodes for data transfer of the BatMag software developed by Ongaro *et al.* [25]. The graph is generated using the `rqt_graph` command.

B.1 Hardware designs

A few changes and additions are made to the original setup by Ongaro *et al.* [25]. Firstly, a workspace is designed to hold the microparticles for experimental purposes. The workspace is fabricated by cutting acrylic panels using a laser cutter. The design of these pieces are made in SolidWorks (Figure B.2). The acrylic panel is 3mm thick and the workspace creates a space of 22x22x25mm where the top of the workspace is open. The pieces are glued together to Pattex special glue for models. The workspace is glued on the sides and outside of the workspace to make the workspace waterproof. The bottom of the workspace is one piece to prevent glue bubbles on the intersections between the planes for maximal quality of the video recordings. The bottom and back side of the workspace are covered with white paper to get a contrast between the microparticles and background.

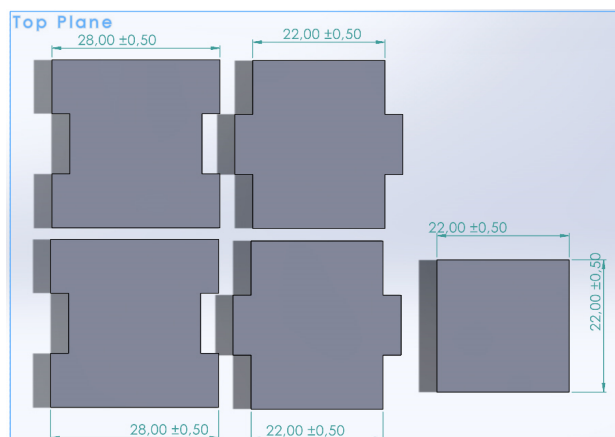


Figure B.2: SolidWorks design of the transparent workspace that creates a 22x22x22 mm workspace for experimental trials.

An addition to the setup is a platform inside the workspace that holds the workspace with mi-

croparticles (Figure B.3). This platform, designed using SolidWorks and fabricated using a 3D printer, has to be leveled that the middle of the workspace is exactly in the middle of the setup. On top of the platform a square (28x28mm) is 1 mm hollowed out to fit the workspace exactly. When the workspace is placed on top of the platform the coils will be located at each corner of the workspace. The platform can be attached to the table with screws.



Figure B.3: SolidWorks design for the platform on which the designed workspace is placed. This platform is placed inside the BatMag system.

The lights in the BatMag setup by Ongaro *et al.* [25], the lights would give reflections onto the workspace which gives a lot of disturbance in the recorded videos by the cameras. To prevent this we decide to remove the lights that are vested to the cameras and design a 3D print of light holders that hold the lights so the lights would be emit light towards the cameras instead (Figure B.4). To increase the light sources, we place two extra lamps to increase contrast in the camera images.

Lastly, one of the camera's is moved to the top of the setup to record the top behaviour of the workspace to be able to see the behaviour of the magnetic carpet into two dimensions.

B.2 Software design

The GUI designed by Ongaro *et al.* [25] consists of three tabs. The first tab is an initialization page where parameters, such as type of control, used particles and imaging modes, can be set (Figure B.5). The second tab is the control page. On this page, the control algorithm and tracking algorithms can be started (Figure B.6). The last tab is the debug tab in which it is possible to set currents directly onto the different coils for debugging purposes (Figure B.7).

To be able to perform cargo transport, a fourth tab is created. On this page, various parameters can be set to actuate the magnetic carpet inside the workspace. The parameters of each

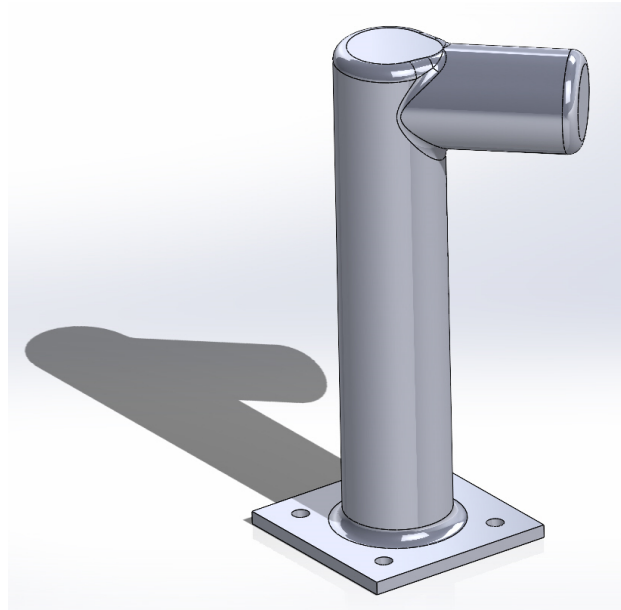


Figure B.4: SolidWorks design for the LED holders used in the BatMag setup to hold the LEDs.

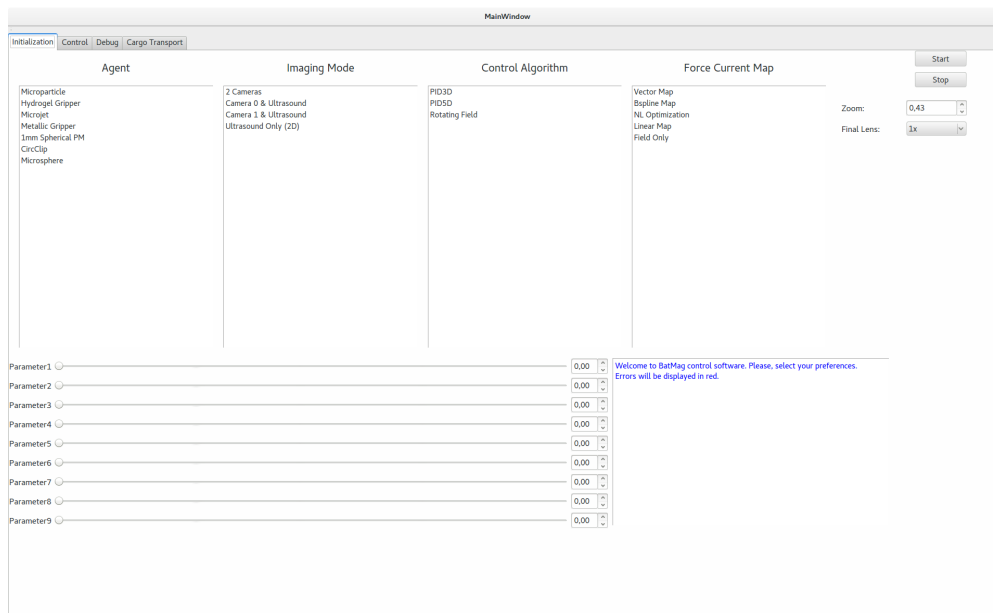


Figure B.5: Initialization page of the GUI for the control of microbeads by Ongaro et al. [25]. On this page, the user is able to set parameters like agent type, imaging mode, control algorithm and the force current map of the running program.

magnetic field such as the amplitude and frequency can be set on the GUI. In addition, the orientation of the magnetic field can be defined by angles and whether the magnetic field is clockwise or anti-clockwise. There are a few additional parameters like a delay for the one sided oscillating magnetic field and the direction of sweeping of the sweeping magnetic field. Furthermore, It is possible to record raw data dumps of the values of amps, that are put onto each coil at a certain time unit, and to record the camera's with a framerate of 25 frames per second. The GUI includes two push buttons for starting and stopping the cargo transport program.

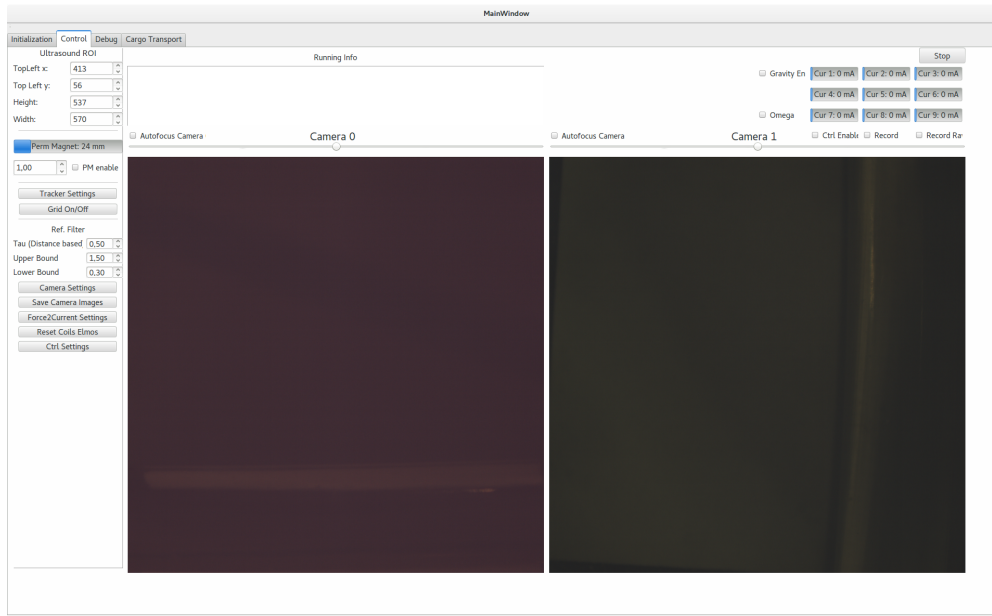


Figure B.6: Control page which is usable after setting the parameters on the initialization page. On this page you can start the control algorithm and adjust the settings for e.g. the cameras and the tracking algorithm.

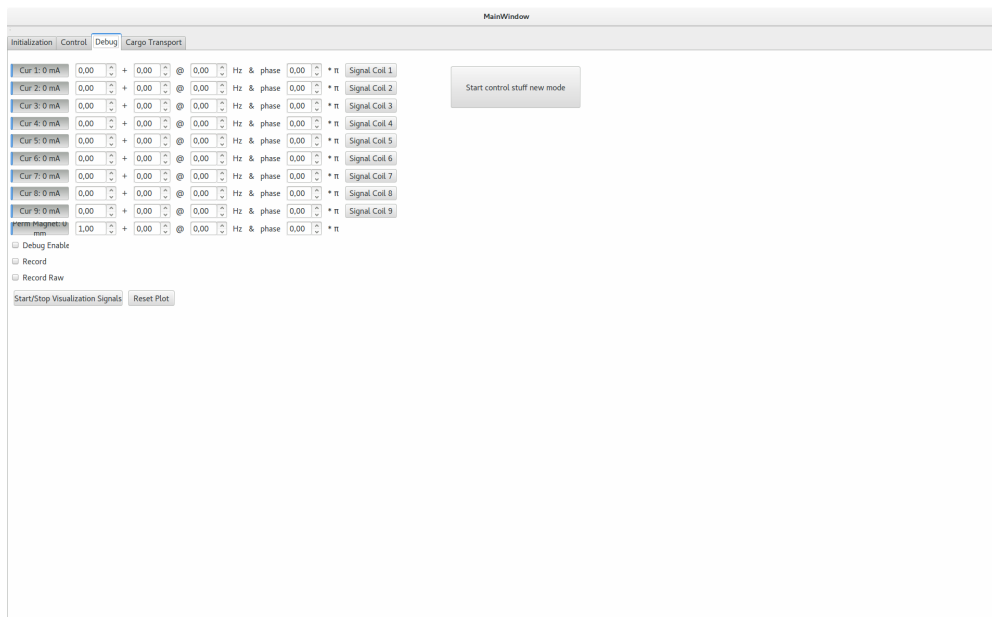


Figure B.7: Debug page where it is possible to put amps directly onto the coils for testing. It is possible to create sinusoidal signals using a certain amplitude, offset and frequency.

A ROS node called *cargo_transport* is added which creates the four different magnetic fields (see Figure B.9). This ROS node communicates through the *cargo_direction* topic to obtain information on the direction of the magnetic field and whether the signals should include a delay or direction of the sweeping and whether the magnetic field should be clockwise or anti-clockwise. Another topic called *cargo_settings* (not depicted in the ROS graph) is used to obtain the type of magnetic field, amplitude of the magnetic field, frequency, phase shift and value of coil number 9. The ROS node uses this information to calculate the values of each coil at the current time unit and publishes this information onto the topic (called *map_output*) which communicates with the

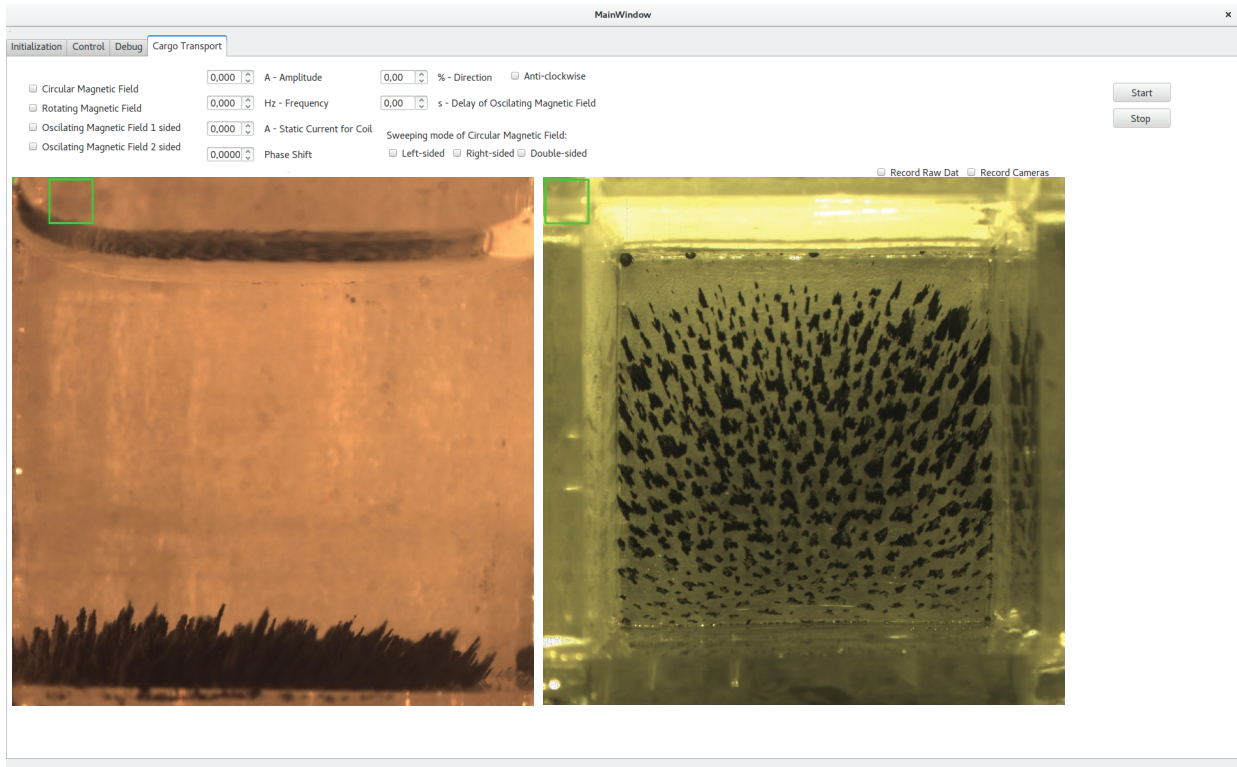


Figure B.8: Cargo transport tab developed as addition onto the existing GUI developed by Ongaro et al. [25] for cargo transport purposes using different magnetic fields.

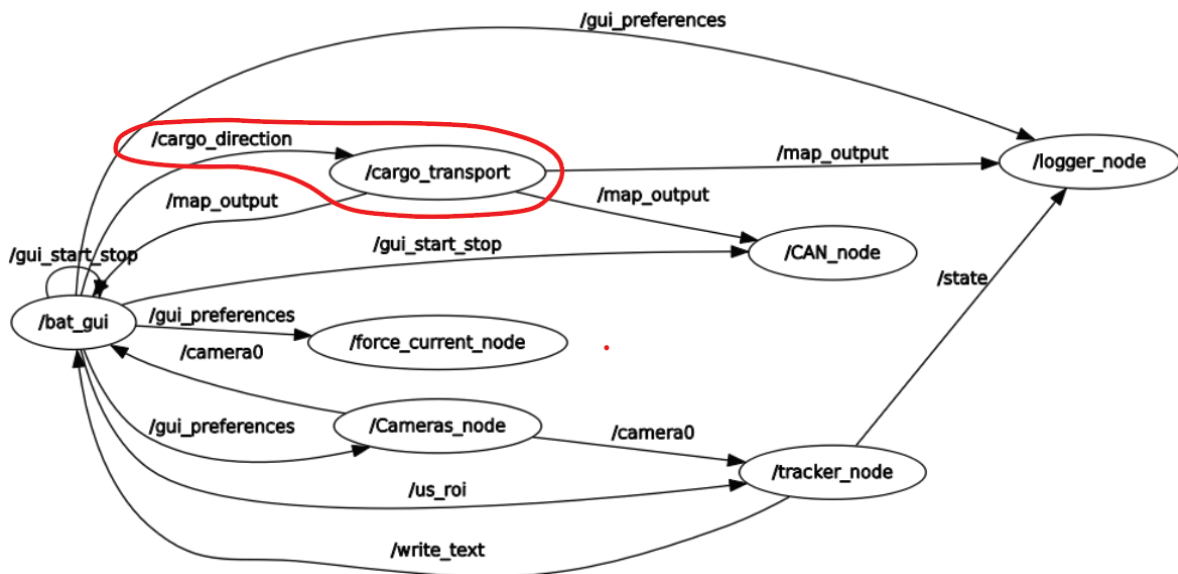


Figure B.9: Graph of the ROS nodes and ROS topics generated using the `rqt_graph` command. The red workspace highlights the created ROS node and ROS topic for the cargo transport.

CAN-bus node. The `cargo_settings` topic publishes messages with 20 Hz.

Description of performed experiments

This chapter describes a detailed description of each performed experiment.

C.1 Characterisation of carpet formation

This experiment is performed for 10 mg - 20 mg - 30 mg - 40 mg - 50 mg - 60 mg - 70 mg - 80 mg - 90 mg - 100 mg - 150 mg - 200 mg - 250 mg - 300 mg of iron microparticles.

1. Clean the workspace with water.
2. Put the workspace on the measuring device and make sure it says 0 mg.
3. Put the first amount of iron microparticles inside the workspace (10 mg).
4. Add 8ml water into the workspace.
5. Stir the substance to manually distribute the iron microparticles over the workspace.
6. Wait until the microparticles has sunk to the bottom and place the workspace inside the BatMag setup.
7. Power coil number 9 to 1 A using the debug mode in the GUI.
8. Save a frame of the camera to the computer.
9. Deactivate coil number 9.
10. Repeat step 7 through step 9 again three times.
11. Repeat step 7 through step 10 again for 2 A, 3 A, 4 A and 5 A.
12. Clean the workspace and remove all iron microparticles.
13. Repeat step 2 through step 12 for the other amounts of iron microparticles (20 mg - 30 mg - 40 mg - 50 mg - 60 mg - 70 mg - 80 mg - 90 mg - 100 mg - 150 mg - 200 mg - 250 mg - 300 mg).

C.2 Characterisation of the behavior of the carpet under different magnetic fields

C.2.1 Experiment 1: carpet under magnetic fields

This experiment is performed for 10 mg - 50 mg - 100 mg - 150 mg - 200 mg of iron microparticles. The simple rotational magnetic field and the two sided oscillating magnetic field is used (Figure C.1). In addition, the frequencies, for the sinusoidal signals of each coil to generate the magnetic fields, used in this experiment are 0.125 Hz - 0.25 Hz - 0.5 Hz - 1.0 Hz - 1.5 Hz - 2.0 Hz. Lastly, for coil number 9 0 A - 1 A - 2 A - 3 A - 4 A - 5 A is used. During this experiment the amplitude is set constant to 1.

1. Clean the workspace with water.
2. Put the workspace on the measuring device and make sure it says 0 mg.
3. Put the first amount of iron microparticles inside the workspace (10 mg).
4. Add 8ml water into the workspace.
5. Stir the substance to manually distribute the iron microparticles over the workspace.
6. Wait until the microparticles has sunk to the bottom and place the workspace inside the BatMag setup.
7. Use the GUI to set the parameters: set the amplitude on 1, set the frequency on 0.125 Hz and set coil number 9 on 0 A. Activate the rotational magnetic field.
8. Record the behaviour for 20 seconds.
9. Deactivate the rotational magnetic field using the GUI.
10. Stir the solution to manually distribute the iron microparticles and wait until the microparticles are sunk to the bottom of the workspace.
11. Repeat step 7 through step 10 using 1 A - 2 A - 3 A - 4 A - 5 A for coil number 9 as setting in the GUI.
12. Repeat step 7 through step 11 using frequencies 0.25 Hz - 0.5 Hz - 1.0 Hz - 1.5 Hz - 2.0 Hz as setting in the GUI.
13. Use the GUI to set the parameters: set the amplitude on 1, set the frequency on 0.125 Hz and set coil number 9 on 0 A. Activate the two sided oscillating magnetic field.
14. Record the behaviour for 20 seconds.
15. Deactivate the two sided oscillating magnetic field using the GUI.
16. Stir the solution to manually distribute the iron microparticles and wait until the microparticles are sunk to the bottom of the workspace.

17. Repeat step 13 through step 16 using 1 A - 2 A - 3 A - 4 A - 5 A for coil number 9 as setting in the GUI.
18. Repeat step 13 through step 17 using frequencies 0.25 Hz - 0.5 Hz - 1.0 Hz - 1.5 Hz - 2.0 Hz as setting in the GUI.
19. Repeat step 1 through step 18 again for 50 mg - 100 mg - 150 mg - 200 mg of iron microparticles.

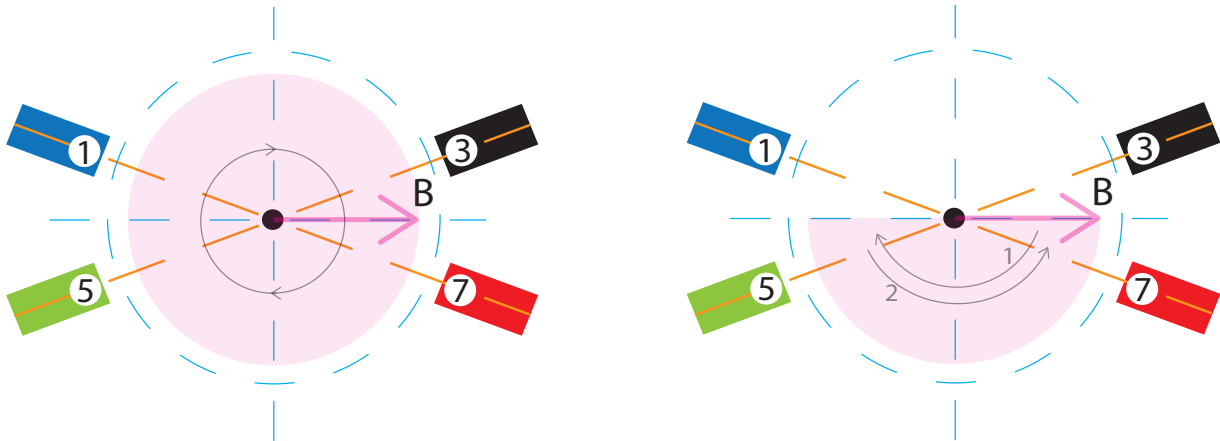


Figure C.1: Designed (left) rotational and (right) oscillating magnetic field for identifying the behaviour of the magnetic carpet.

C.2.2 Experiment 2: Adding iron microparticles under rotational magnetic field

For this experiment the GUI settings are set as follows: the amplitude is set on 1, the frequency is set on 0.25 Hz and coil number 9 is set on 3 A.

1. Clean the workspace with water.
2. Add 8ml water into the workspace.
3. Place the workspace inside the BatMag setup.
4. Use the GUI to set the parameters: set the amplitude on 1, set the frequency on 0.25 Hz and set coil number 9 on 3 A. Activate the rotational magnetic field.
5. Start recording the camera's.
6. Take 25 mg of microparticles and add this inside the workspace.
7. Wait for 1 minute.
8. Take 25 mg of microparticles and add this inside the workspace.

C.3 Carpet strength

This experiment is performed using 10 mg - 25 mg - 50 mg. In addition, in this experiment the next eight objects are used to test the pillar strengths: 3x3 and 5x5 objects of 1, 2 and 4 PET layers and transparent PET.

The software for this experiment is specially designed that only coil number 9 is activated for two seconds and then the two sided oscillating magnetic field (with a frequency of 0.5 Hz) is activated for 6 seconds (three periods). Then the oscillating field is deactivated and coil number 9 is increased with 1 A and the process is repeated until 5A is reached.

1. Clean the workspace with water.
2. Put the workspace on the measuring device and make sure it says 0 mg.
3. Put the first amount of iron microparticles inside the workspace (10 mg).
4. Add 8ml water into the workspace.
5. Stir the substance to manually distribute the iron microparticles over the workspace.
6. Wait until the microparticles has sunk to the bottom and place the workspace inside the BatMag setup.
7. Place the first object (3x3 - one layer of PET) at the middle of the workspace.
8. Start the recording using the GUI.
9. Start the designed software that automatically increases coil number 9 from 1 A to 5 A.
10. Wait until the software is executed.
11. Stop the recording using the GUI.
12. Remove the object from the workspace.
13. Repeat step 5 through step 12 for all other seven objects (3x3 and 5x5 objects of 1, 2 and 4 PET layers and transparent PET).
14. Repeat step 1 through step 13 using 25 mg - 50 mg of iron microparticles.

C.4 Cargo transport using different magnetic fields

C.4.1 Experiment 1: cargo transport using rotating, oscillating and sweeping magnetic fields

In this experiment 25 mg of iron microparticles is used. In addition a frequency of 0.5 Hz - 1.0 Hz is used. The amplitude used is 0.5 and 2 A is used for coil number 9. The direction of the magnetic

field that is used is 45 degrees (this is in vertical direction compared to the camera recordings of the camera on the top of the BatMag setup).

The magnetic fields used in this experiment are the rotational field (as shown in Figure C.1), one sided oscillating magnetic field, two sided oscillating magnetic field and three types of the sweeping magnetic field (sweeping on the left side, sweeping on the right side and sweeping on both sides). For the one sided oscillating magnetic field, coil number 9 is deactivated earlier compared to the other coils with 0.02 s for 0.5 Hz and 0.04 s for 1.0 Hz.

The planar objects used in this experiment are the eight objects: 3x3 and 5x5 objects of 1, 2, 4 PET layers and transparent PET.

1. Clean the workspace with water.
2. Put the workspace on the measuring device and make sure it says 0 mg.
3. Put 25 mg of iron microparticles inside the workspace.
4. Add 8ml water into the workspace.
5. Stir the substance to manually distribute the iron microparticles over the workspace.
6. Wait until the microparticles has sunk to the bottom and place the workspace inside the BatMag setup.
7. Place the first object (3x3 - one layer of PET) at the middle of the workspace.
8. Set the settings for the cargo transport inside the GUI: 0.5 for Amplitude, 0.5 Hz for frequency, 2 A for coil number 9, a direction of 45 degrees and a delay for coil number 9 (of 0.02 s for 0.5 Hz and 0.04 s for 1.0 Hz).
9. Start the recording using the GUI.
10. Activate the rotational magnetic field.
11. Record the behaviour for at least 1 minute. If the object is moving, record the behaviour until the object reaches one of the sides of the workspace.
12. Pause the recording.
13. Remove the object from the workspace.
14. Stir the substance to manually distribute the iron microparticles over the workspace.
15. Wait until the microparticles has sunk to the bottom and place the workspace inside the BatMag setup.
16. Place the object at the middle of the workspace.

17. Repeat step 9 through step 16 using the two sided oscillating magnetic field, one sided oscillating magnetic field, sweeping magnetic field with right sided sweeping, sweeping magnetic field with left sweeping and sweeping magnetic field with two sided sweeping.
18. Repeat step 8 through step 17 using 1.0 Hz for the frequency.
19. Repeat step 1 through step 18 for the other seven planar objects: 3x3 and 5x5 objects of 1, 2, 4 PET layers and transparent PET.

C.4.2 Experiment 2: Cargo transport using rotational magnetic field

In this experiment 25 mg of microparticles is used. In addition, an amplitude of 0.5, a frequency of 0.5 Hz and 2 A for coil number 9 is used. The magnetic field used in this experiment is the rotational magnetic field as illustrated in Figure C.2.

The planar objects used in this experiment are the eight objects: 3x3 and 5x5 objects of 1, 2, 4 PET layers and transparent PET.

1. Clean the workspace with water.
2. Put the workspace on the measuring device and make sure it says 0 mg.
3. Put 25 mg of iron microparticles inside the workspace.
4. Add 8ml water into the workspace.
5. Stir the substance to manually distribute the iron microparticles over the workspace.
6. Wait until the microparticles has sunk to the bottom and place the workspace inside the BatMag setup.
7. Place the first object (3x3 - one layer of PET) at the middle of the workspace.
8. Set the settings for the cargo transport inside the GUI: 0.5 for Amplitude, 0.5 Hz for frequency and 2 A for coil number 9.
9. Start the recording using the GUI.
10. Activate the horizontal rotational magnetic field.
11. Record the behaviour for at least 1 minute. If the object is moving, record the behaviour until the object reaches one of the sides of the workspace.
12. Stop the recording.
13. Remove the planar object from the workspace.
14. Repeat step 5 through step 13 using the other seven planar objects: 3x3 and 5x5 objects of 1, 2, 4 PET layers and transparent PET.

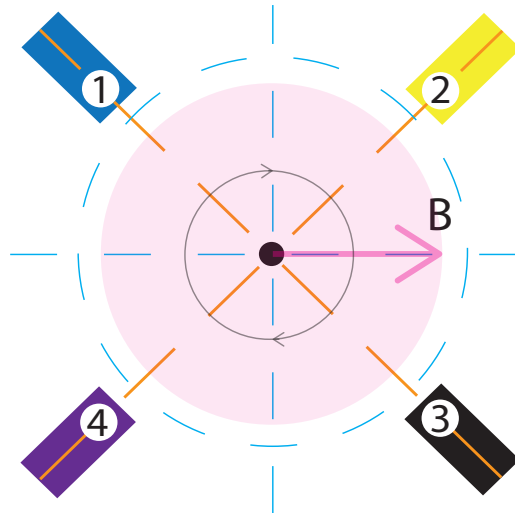


Figure C.2: Rotational magnetic field in the horizontal plane of the BatMag setup used for cargo transport.

C.5 Final experiments

In this section we describe the final experiments to show the capabilities of the designed magnetic carpet inside the BatMag setup.

C.5.1 Experiment 1: Cargo transport with circular and triangle planar objects under rotating magnetic field

In this experiment we test besides the squared the cargo transport with different shaped planar objects than the squared objects used before. In this experiment we will use circular (diameter 3 mm) and triangular (side length 3.5 mm) planar objects of 2 and 4 layers PET.

Next parameters settings are used during this experiment: Amplitude of 0.5, frequency of 0.5 Hz and 2 A for coil number 9. Lastly, we will use the horizontal rotational magnetic field as illustrated in Figure C.2.

1. Clean the workspace with water.
2. Put the workspace on the measuring device and make sure it says 0 mg.
3. Put 25 mg of iron microparticles inside the workspace.
4. Add 8ml water into the workspace.
5. Stir the substance to manually distribute the iron microparticles over the workspace.
6. Wait until the microparticles has sunk to the bottom and place the workspace inside the BatMag setup.
7. Place the first object (circular object with 3 mm diameter - two layers of PET) at the middle of the workspace.

8. Set the settings for the cargo transport inside the GUI: 0.5 for Amplitude, 0.5 Hz for frequency and 2 A for coil number 9.
9. Start the recording using the GUI.
10. Activate the horizontal rotational magnetic field.
11. Record the behaviour for at least 1 minute. If the object is moving, record the behaviour until the object reaches one of the sides of the workspace.
12. Stop the recording.
13. Remove the planar object from the workspace.
14. Repeat step 5 through step 13 using the other three planar objects: circular object with 3 mm and triangular object with side length of 3.5 mm of 2 and 4 PET layers.

C.5.2 Experiment 2: Cargo transport into two dimensions

In this experiment we use the squared planar objects 3x3 and 5x5 of 2 and 4 layers of PET and the circular (diameter 3 mm) and triangular (side length 3.5 mm) planar objects of 2 and 4 layers PET.

Next parameters settings are used during this experiment: Amplitude of 0.5, frequency of 0.5 Hz, 2 A for coil number 9 and an initial direction of 0 degrees. Lastly, we will use the sweeping magnetic field with the right sweeping option.

1. Clean the workspace with water.
2. Put the workspace on the measuring device and make sure it says 0 mg.
3. Put 25 mg of iron microparticles inside the workspace.
4. Add 8ml water into the workspace.
5. Stir the substance to manually distribute the iron microparticles over the workspace.
6. Wait until the microparticles has sunk to the bottom and place the workspace inside the BatMag setup.
7. Place the first object (3x3 squared object - 2 layers PET) close at the right upper corner of the workspace (coils 2 and 6 are located at this corner).
8. Set the settings for the cargo transport inside the GUI: 0.5 for Amplitude, 0.5 Hz for frequency, 2 A for coil number 9 and 0 for the direction of the magnetic field.
9. Start the recording using the GUI.
10. Activate the sweeping magnetic field using the right sweep.

11. Wait until the object reaches the middle of the workspace. Then change the direction of the magnetic field to 90 degrees.
12. Record the behaviour for at least 1 minute. If the object is moving, record the behaviour until the object reaches one of the sides of the workspace.
13. Stop the recording.
14. Remove the planar object from the workspace.
15. Repeat step 5 through step 14 using the other seven planar objects: squated planar objects 3x3 and 5x5, circular object with 3 mm and triangular object with side length of 3.5 mm of 2 and 4 PET layers.

C.5.3 Experiment 3: Replacing carpet and planar object

Experiment 3a: Retracting carpet after cargo transport

In this experiment we use the 5x5 squared planar object of 2 layers of PET. In addition we use an amplitude of 1, a frequency of 0.5 Hz, 2 A for coil number 9 and an initial direction of 0 degrees. Lastly, the sweeping magnetic field on the right side and the one sided oscillating magnetic field is used.

1. Clean the workspace with water.
2. Put the workspace on the measuring device and make sure it says 0 mg.
3. Put 25 mg of iron microparticles inside the workspace.
4. Add 8ml water into the workspace.
5. Stir the substance to manually distribute the iron microparticles over the workspace.
6. Wait until the microparticles has sunk to the bottom and place the workspace inside the BatMag setup.
7. Place the object (5x5 squared object - 2 layers PET) at the middle of the workspace.
8. Set the settings for the cargo transport inside the GUI: 0.5 for Amplitude, 0.5 Hz for frequency, 2 A for coil number 9 and 0 for the direction of the magnetic field.
9. Start the recording using the GUI.
10. Activate the sweeping magnetic field using the right sweep.
11. Wait until the object reaches the lower left corner of the workspace. Then deactivate the sweeping magnetic field, set coil number 9 delay to 0.02 s and activate the one sided oscillating magnetic field.
12. Change the direction of the magnetic field to 90 degrees.

13. Record the behaviour until the carpet has moved to the opposite corner of the workspace.
14. Stop the recording.
15. Remove the planar object from the workspace and clean the workspace.

Experiment 3a: Relocating carpet to planar object to perform cargo transport and retract carpet after cargo transport is completed

In this experiment we use the 5x5 and 3x3 squared planar object of 2 layers of PET. In addition we use an amplitude of 1, a frequency of 0.5 Hz, 2 A for coil number 9 and an initial direction of 0 degrees. Lastly, the sweeping magnetic field on the right side and the one sided oscillating magnetic field is used.

1. Clean the workspace with water.
2. Put the workspace on the measuring device and make sure it says 0 mg.
3. Put 25 mg of iron microparticles inside the workspace.
4. Add 8ml water into the workspace.
5. Place the workspace inside the batmag workspace.
6. Activate the one sided oscillating magnetic field with direction 0 degrees and check the option anti-clockwise in the GUI to gather all iron microparticles in the lower right corner of the workspace.
7. When all microparticles are gathered, deactivate the one sided oscillating magnetic field and uncheck the option anti-clockwise in the GUI.
8. Place the object (5x5 squared object - 2 layers PET) at the middle of the workspace.
9. Set the settings for the cargo transport inside the GUI: 0.5 for Amplitude, 0.5 Hz for frequency, 2 A for coil number 9 and 0 for the direction of the magnetic field.
10. Start the recording using the GUI.
11. Activate the one sided oscillating magnetic field.
12. Wait until the planar object is fully covered by the pillars.
13. Deactivate the one sided oscillating magnetic field.
14. Activate the sweeping magnetic field using the right sweep.
15. Wait 1 minute or until the object reaches the sides of the workspace.
16. Deactivate the sweeping magnetic field

17. Change the direction to 90 degrees inside the workspace and check the anti-clockwise option.
18. Activate the one sided oscillating magnetic field.
19. Wait until the carpet is gathered inside the lower left corner of the workspace.
20. Stop the recording.
21. Remove the planar object from the workspace.
22. Repeat step 5 through step 20 using the 3x3 squared planar object (2 layers PET).
23. Remove the planar object from the workspace and clean the workspace.

Simulations of magnetic fields

Simulations of the seven actuation mechanisms are discussed in this chapter. For each actuation mechanism, the magnetic field (black vectors) and gradient field (red vectors) are shown at 0 , 0.5π , π and 1.5π of one period of the signals. The simulations are shown for the x-y plane in which the top camera is located, and for the y-z frame in which the side camera is located. Note that Figure D.1, Figure D.2, Figure D.3 and Figure D.4 are shown in landscape mode and that each simulation has its own colored bar. The simulations of the side view have the same dimensions as the workspace during experiments and the simulations from the top view are at the bottom of the workspace since this is where the magnetic carpet is formed.

Figure D.1 shows the simulations of the rotational magnetic fields including rotating magnetic fields in the horizontal and vertical planes (with respect to the BatMag system). Figure D.2 shows the simulations of the oscillating magnetic fields including the two-sided oscillating magnetic field and the one-sided oscillating magnetic field. Lastly, the sweeping magnetic fields are shown in Figure D.3 and Figure D.4.

In these simulations, the magnetic field corresponds with the movement of the pillars. The gradient field changes over time as well. However, the gradient is always pointing towards the bottom of the workspace which makes sure that the pillar-structure is maintained over time. In experiments, it can be seen that the pillars are bending more at the corners of the workspace. This can be explained using these simulations since the gradient vectors and magnetic field vectors are also bending outwards at the sides of the workspace.

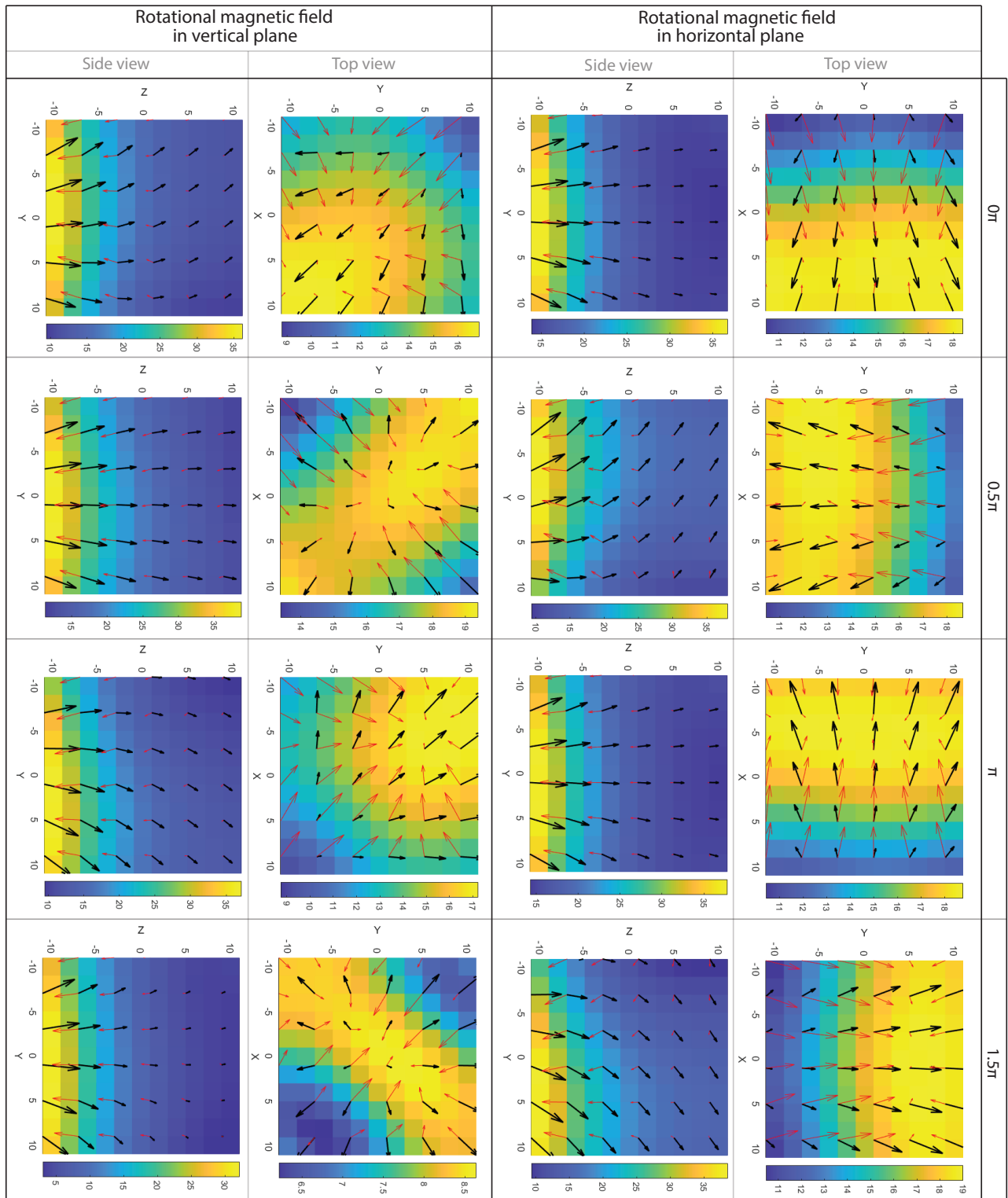


Figure D.1: Simulations of one period of the rotational magnetic fields in horizontal and vertical plane with respect to the BatMag setup. Note that the graph is in landscape mode and that the dimensions of the side and top views are given of the workspace inside the BatMag system.

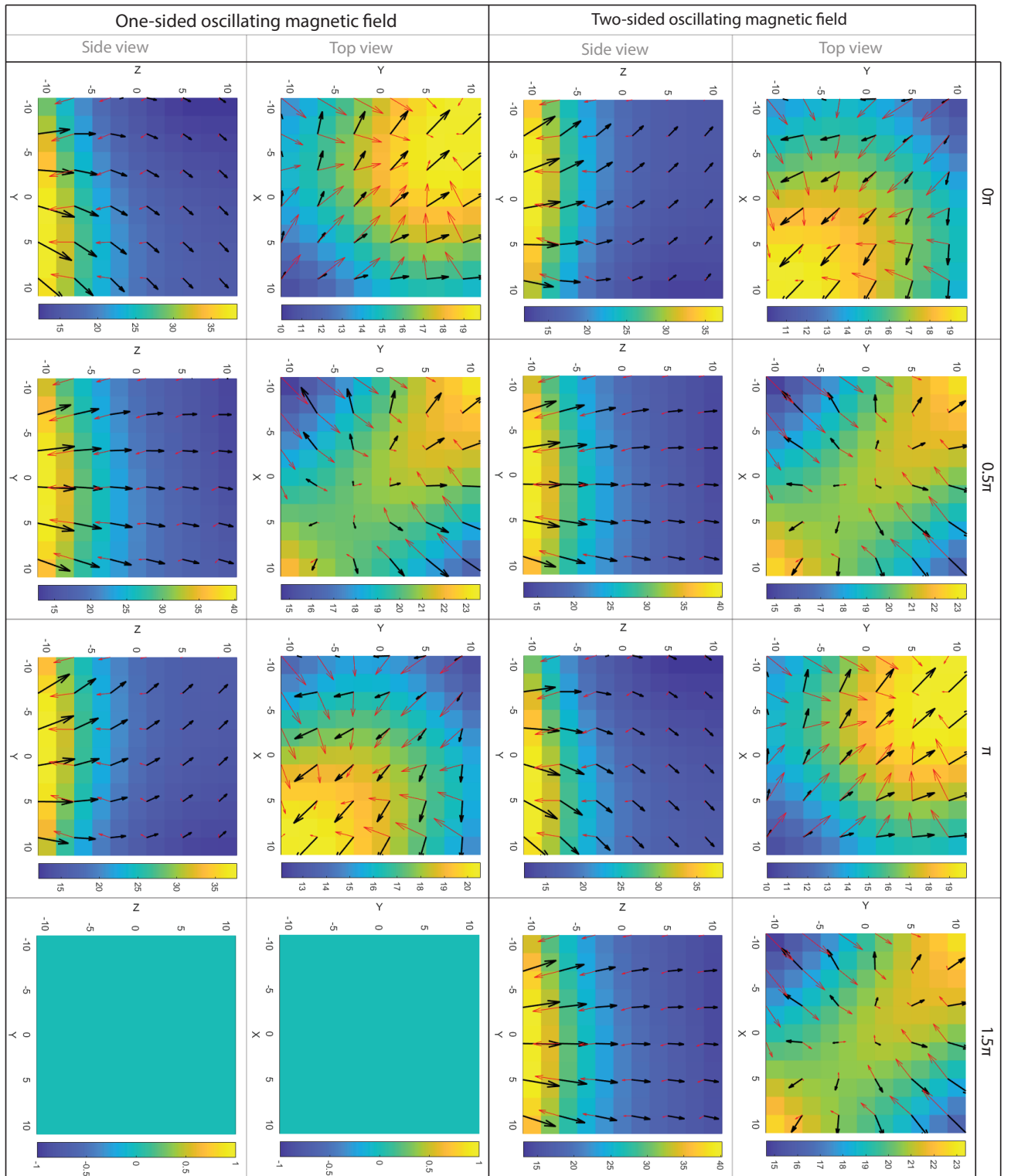


Figure D.2: Simulations of one period of the oscillating magnetic fields: two-sided oscillating magnetic field and the one-sided oscillating magnetic field. Note that the graph is in landscape mode and that the dimensions of the side and top views are given of the workspace inside the BatMag system.

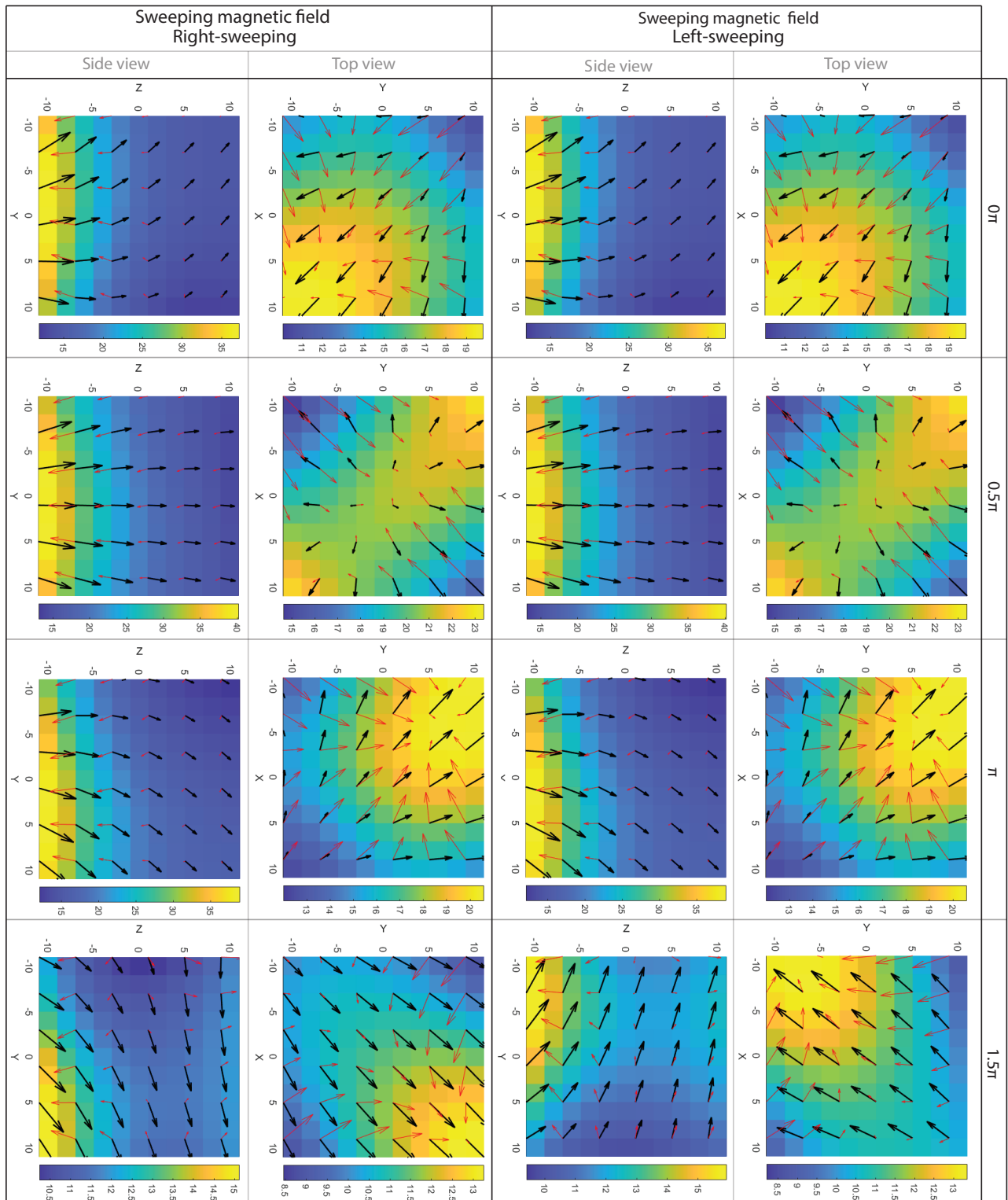


Figure D.3: Simulations of one period of the left- and right-sided sweeping magnetic fields. Note that the graph is in landscape mode and that the dimensions of the side and top views are given of the workspace inside the BatMag system.

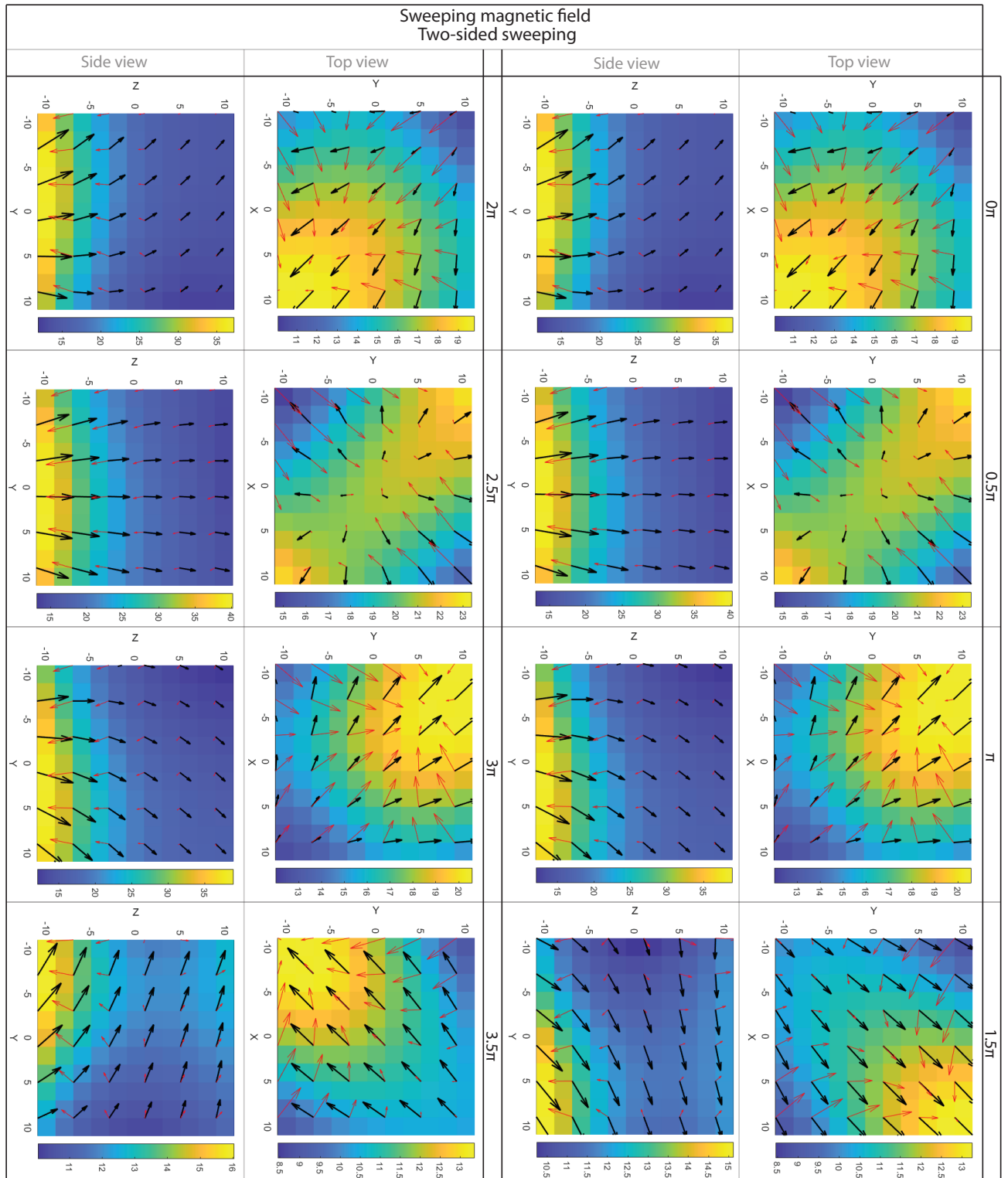


Figure D.4: Simulations of two periods of the two-sided sweeping magnetic field. (Two periods are shown since the sweeping side changes alternately.) Note that the graph is in landscape mode and that the dimensions of the side and top views are given of the workspace inside the BatMag system.

Full data of planar object displacement

The graphs shown in Figure E.1 and Figure E.2 show the full displacement paths in x- and y-directions for each planar object using the different actuation mechanisms. The data described in Table 4.1 and Table 4.2 is derived from these graphs. The data of each case is shift to the origin so the data can be compared between planar objects. Note that the planar objects did not start at the exact same position inside the workspace. This can give small errors between the different planar objects since the displacement of a planar object depends on the interaction with the pillars inside the workspace while the pillars behave differently at each point in the workspace. A cross sign inside the graphs shows the moment at which the planar object reaches a wall of the workspace and therefore, the used actuation mechanism is deactivated.

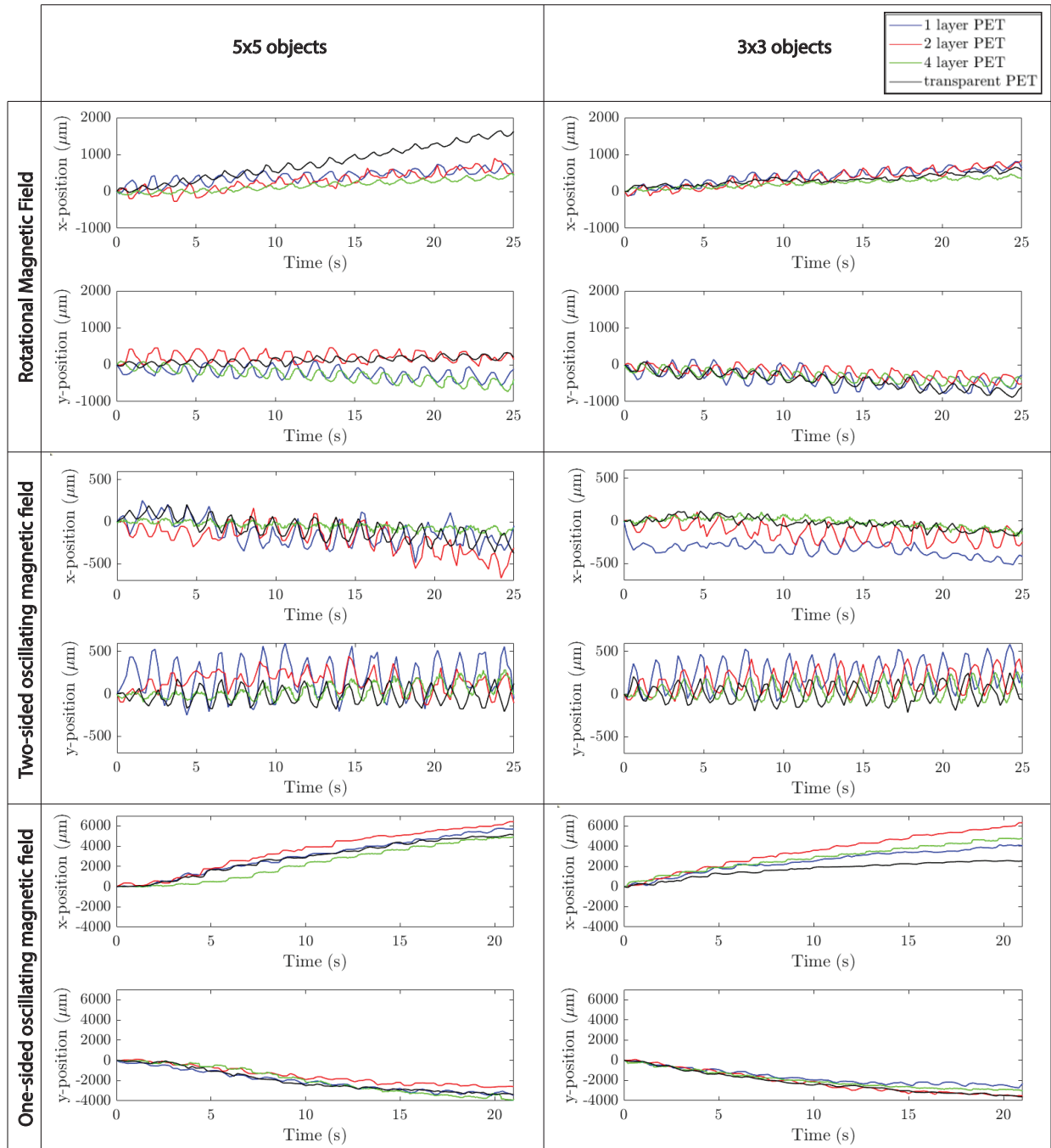


Figure E.1: Displacements of the 5 mm and 3 mm dimension squared planar objects for the vertical rotational magnetic field, two-sided oscillating magnetic field and the one-sided oscillating magnetic field. All objects have similar displacements. In some cases, there are visible differences in the displacements over 25 seconds. This can be explained by the fact that each planar object is not placed at exactly the same initial position inside the workspace since the pillars show different behaviour at different locations inside the workspace.

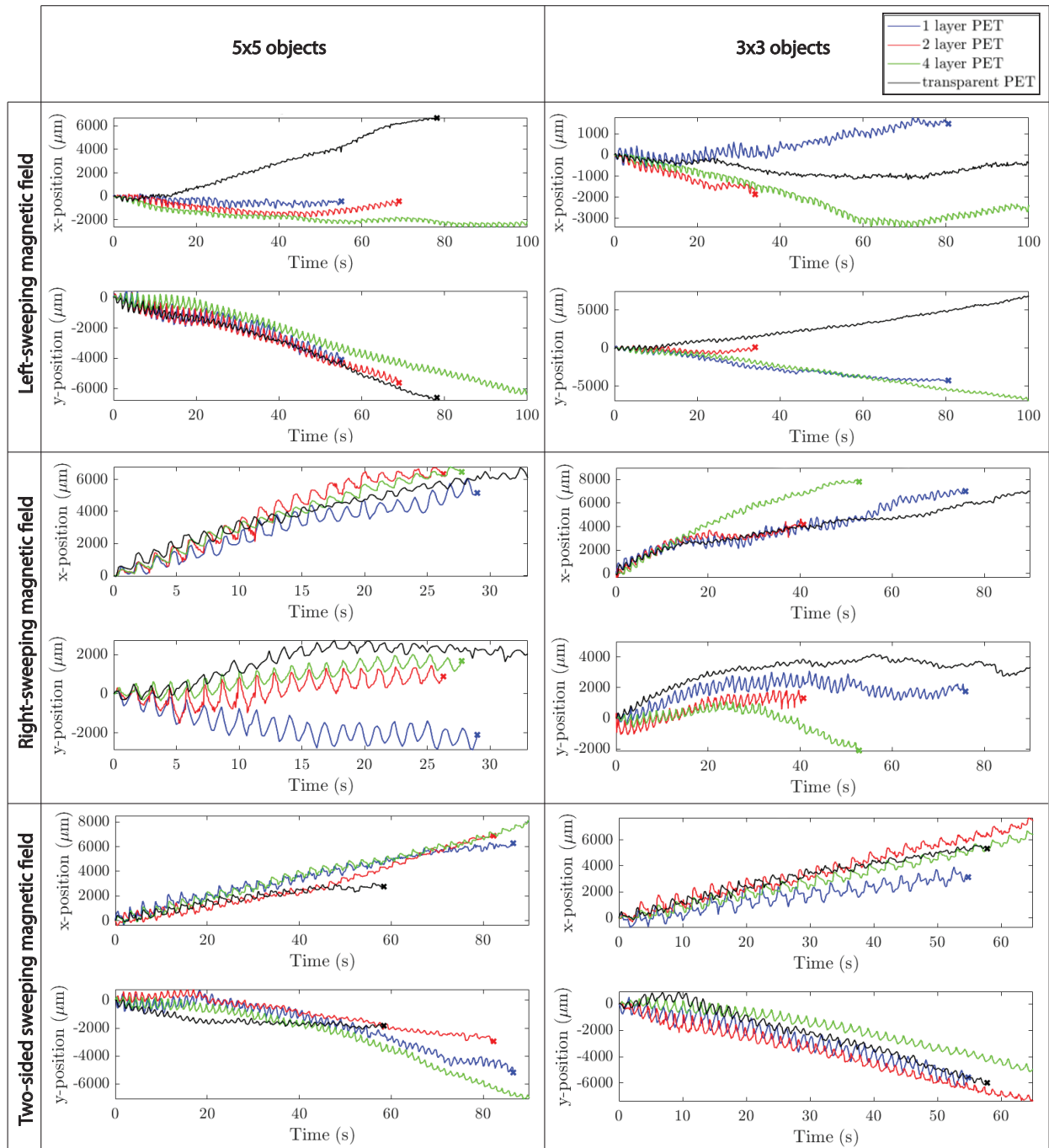


Figure E.2: Displacements of the 5 mm and 3 mm dimension squared planar objects for the sweeping magnetic field. All objects have similar displacements. In some cases, there are visible differences in the displacements over 25 seconds. This can be explained by the fact that each planar object is not placed at exactly the same initial position inside the workspace since the pillars show different behaviour at different places inside the workspace. In addition, for the planar objects of transparent PET, there are no pillars underneath the object anymore at a certain point in time. These planar objects are then displaced by pushing over the bottom of the workspace which also changes the moving direction as can be seen for the left-sweeping magnetic field.